REPORT DOCUMENTATION PAGE

Public reporting burden for this collection of information is estimated to average 1 hour per response, including the time for reviewing instructions, searching existing data sources, gathering and maintaining the data needed, and completing and reviewing the collection of information. Send comments regarding this burden estimate or any other aspect of this collection of information, including suggestions for reducing this burden, to Washington Headquarters Services, Directorate for Information Operations and Reports, 1215 Jefferson Davis Highway, Suite 1204, Arlington, VA 22202-4302, and to the Office of Management and Budget, Paperwork Reduction Project (0704-0188), Washington, DC 20503.

1. AGENCY USE ONLY (Leave blank)	2. REPORT DATE 30/9/95	3. REPORT TYPE AND DATES COVERED Final Tech. Rept. 15/8/93-14/8/95

4. TITLE AND SUBTITLE	5. FUNDING NUMBERS
(U) Breakup and Turbulence Generation in Dense Sprays	PE - 61102F PR - 2308 SA - BS G - F49620-92-J-0399

6. AUTHOR(S)

L.-P. Hsiang, J.-S. Wu, W.-H. Chou, J.-H. Chen and G.M. Faeth

7. PERFORMING ORGANIZATION NAME(S) AND ADDRESS(ES)	8. PERFORMING ORGANIZATION REPORT NUMBER
The University of Michigan Ann Arbor, MI 48109	

9. SPONSORING/MONITORING AGENCY NAME(S) AND ADDRESS(ES)	10. SPONSORING/MONITORING AGENCY REPORT NUMBER
AFOSR/NA 110 Duncan Avenue, Suite B115 Bolling AFB, D.C. 20332-0001	AFOSR-TR 96-0037

11. SUPPLEMENTARY NOTES

12a. DISTRIBUTION/AVAILABILITY STATEMENT	12b. DISTRIBUTION CODE
Approved for public release; distribution is unlimited	

13. ABSTRACT (Maximum 200 words)

Single- and double-pulse holography was used to measure the outcomes of secondary drop breakup after shock-wave disturbances in air at normal temperature and pressure; the resulting drop breakup regimes and drop size and velocity distributions were successfully interpreted and correlated based on phenomenalogical analysis. Laser velocimetry was used to measure the properties of sphere wakes at moderate Reynolds numbers (less than 1000) in turbulent environments (relative turbulence intensities in the range 2.1-09.5%); it was found that velocity distributions in these wakes could be correlated as laminar-like turbulent wakes with effective turbulent viscosities that were simple functions of sphere Reynolds numbers and relative turbulence intensities. A stochastic analysis of turbulence generation by particles (drops) was evaluated using earlier laser velocimetry measurements for dispersed multiphase flows; it was found that velocity fluctuations could be estimated reasonably well based on stochastic synthesis of randomly-arriving particle (drop) wakes using Campbell's theorem.

14. SUBJECT TERMS	15. NUMBER OF PAGES 108
Multiphase Flow, Homogeneous Turbulence, Drop Breakup, Sphere Wakes, Turbulence Generation	16. PRICE CODE

17. SECURITY CLASSIFICATION OF REPORT	18. SECURITY CLASSIFICATION OF THIS PAGE	19. SECURITY CLASSIFICATION OF ABSTRACT	20. LIMITATION OF ABSTRACT
Unclassified	Unclassified	Unclassified	UL

NSN 7540-01-280-5500

19960201 113

DTIC QUALITY INSPECTED 1

Standard Form 298 (890104 Draft)
Prescribed by ANSI Std. 239-18
298-01

BREAKUP AND TURBULENCE GENERATION IN DENSE SPRAYS

by

L.-P. Hsiang, J.-S. Wu, W.-H. Chou, J.-H. Chen and G.M. Faeth
Department of Aerospace Engineering
The University of Michigan
Ann Arbor, Michigan 48109-2118

Final Report

15 August 1993 - 14 August 1995

30 September 1995

ACKNOWLEDGMENTS

TABLE OF CONTENTS

LIST OF TABLES

LIST OF FIGURES

NOMENCLATURE

Symbol		Description
a	=	rate of acceleration
C_D	=	drag
d	=	drop or particle diameter
Eo	=	Eötvös number, $a(\rho_f - \rho_g)d^2/\sigma$
g	=	generic wake effect
G	=	generic property of turbulence generation
ℓ	=	characteristic wake width, Eq. 5
L_{ux}, L_{uy}	=	spatial integral scales
MMD	=	mass median diameter
$\dot{n}''$	=	particle number flux
Oh	=	Ohnesorge number, $\mu_f/(\rho_f d\sigma)^{1/2}$
PDF(ϕ)	=	probability density function of ϕ
Re	=	sphere Reynolds number, du/v_∞ or dU/v_∞
Re_t	=	turbulence Reynolds number, $d\,\overline{U}_\infty/v_t$
SMD	=	Sauter mean diameter
t	=	time
t*	=	characteristic breakup time, $d\,(\rho_f/\rho_g)^{1/2}/u_o$
u	=	streamwise velocity
U	=	relative streamwise velocity
U_t	=	velocity scale for the turbulent wake region, Eq. 4
v	=	cross-stream velocity
We	=	Weber number, $\rho\,d_o u_o^2/\sigma$
x, X	=	streamwise distance

y,Y	=	cross-stream distance
ε	=	rate of dissipation of turbulence kinetic energy
θ	=	initial momentum thickness of wake
μ	=	molecular viscosity
ν	=	kinematic viscosity
ν_t	=	effective turbulence kinematic viscosity
ρ	=	density
σ	=	surface tension
ϕ	=	generic property

Subscripts

b	=	property value at end of breakup
c	=	centerline value
f	=	liquid property
g	=	gas property
G	=	gas property
L	=	liquid property
o	=	initial condition, virtual origin
∞	=	ambient conditions

Superscripts

$(\bar{\ })$	=	time-averaged mean property
$(\bar{\ })'$	=	root-mean-squared fluctuating property

1. INTRODUCTION

Sprays and spray processes have been studied extensively due to their many applications (Faeth 1987, 1990, 1996; Faeth et al. 1995; Ruff and Faeth 1995). Nevertheless, sprays are complex multiphase turbulent flows and fundamental understanding of their properties is not well developed — particularly those processes relating to the near-injector dense portion of the flow. This is a serious deficiency because the dense-spray region involves the breakup of the liquid to form a dispersed phase, which is crucial to the mixing properties of sprays, and also develops the initial conditions required to analyze the structure of the better understood dilute portion of the sprays. Thus, the objective of the present investigation was to study three aspects of dense sprays that involve drop/gas interactions, namely: (1) secondary drop breakup, which is an intrinsic outcome of primary breakup of the liquid, and is the most significant rate process of dense sprays; (2) the structure of sphere wakes at moderate Reynolds numbers in turbulent environments, which is a fundamental property needed to understand the generation of turbulence by moving drops or particles in dispersed multiphase flows; and (3) turbulence generation by dispersed phases, which is the most significant source of turbulence production within dense sprays. The research has relevance to air-breathing propulsion systems, liquid rocket engines and internal combustion engines, among others.

The following description of the research is relatively brief. Additional details may be found in articles, papers and theses resulting from the investigation that are summarized in Table 1. This table also provides a summary of participants in the investigation, oral presentations of portions of the research results and a summary of honors/awards obtained during the grant period. Finally, for convenience, several articles resulting from the research are reproduced in appendices, including: Hsiang and Faeth (1993, 1995), Chou et al. (1995) and J.-S. Wu and Faeth (1993, 1994, 1995a).

The following report considers secondary breakup, sphere wakes and turbulence generation, in turn. Each section is written so that it stands alone; therefore, readers can skip to sections of interest.

Table 1. Summary of Investigation

Articles, Papers and Theses:

Chou, W.-H., Hsiang, L.-P. and Faeth, G.M. (1995) Dynamic properties of secondary breakup. Proceedings of ILASS-AMERICAS-95, Troy, MI, pp. 169-172.

Faeth, G.M. (1995) Spray combustion: a review. Proceedings of Second International Conference on Multiphase Flow, (A. Serizawa, T. Fukano and J. Bataille, eds.), Kyoto University, Kyoto, Vol. 1, pp. CO-1 to CO-16.

Faeth, G.M. (1996) Spray combustion phenomena. Twenty-Sixth Symposium (International) on Combustion, The Combustion Institute, Pittsburgh, invited.

Faeth, G.M. and Wu J.-S. (1992) Sphere wakes at moderate Reynolds numbers in a turbulent environment. Bull. Amer. Phys. Soc. 37, 1730 (abstract only).

Faeth, G.M., Hsiang L.-P. and Wu P.-K. (1995) Structure and breakup properties of sprays. Ann. Rev. Multiphase Flow, in press.

Hsiang, L.-P. (1994) Near-limit drop deformation and secondary breakup. Ph.D. Thesis, The University of Michigan, Ann Arbor, Michigan.

Hsiang, L.-P. and Faeth, G.M. (1993) Drop properties after secondary breakup. Int. J. Multiphase Flow 19, 721-735.

Hsiang, L.-P. and Faeth, G.M. (1993) Deformation and secondary breakup of drops. AIAA Paper No. 93-0814.

Hsiang, L.-P. and Faeth, G.M. (1994) Drop deformation and breakup due to shock wave and steady disturbances. AIAA Paper No. 94-0560.

Hsiang, L.-P. and Faeth, G.M, (1995) Drop deformation and breakup due to shock wave and steady disturbances. Int. J. Multiphase Flow 21, 545-560.

Hsiang, L.-P., Chou, W.-H. and Faeth, G.M. (1995) Temporal variation of drop properties and formation rates during secondary breakup. AIAA Paper 95-2426.

Ruff, G.A. and Faeth, G.M. (1995) Non-intrusive measurements of the structure of dense sprays. Prog. Astro. Aero., in press.

Tseng, L.-K., Ruff, G.A., Wu, P.-K. and Faeth, G.M. (1995) Continuous- and dispersed-phase structure of pressure atomized sprays. Prog. Astro. Aero., in press.

Wu, J.-S. (1994) Structure of sphere wakes at intermediate Reynolds numbers in still and turbulent environments. Ph.D. Thesis, The University of Michigan, Ann Arbor, Michigan.

Wu, J.-S. and Faeth, G.M. (1993) Sphere wakes in still surroundings at intermediate Reynolds numbers. AIAA J. 31, 1448-1455.

Wu, J.-S. and Faeth, G.M. (1993) Effects of ambient turbulence intensity on sphere wakes at intermediate Reynolds numbers. Bull. Amer. Phys. Soc. 38, 2272 (abstract only).

Wu, J.-S. and Faeth, G.M. (1994) Sphere wakes at moderate Reynolds numbers in a turbulent environment. AIAA J. 32, 535-541.

Wu, J.-S. and Faeth, G.M. (1995) Effects of ambient turbulence intensity on sphere wakes at intermediate Reynolds numbers. AIAA J. 33, 171-173.

Wu, J.-S. and Faeth, G.M. (1995) Turbulence generation in homogeneous particle-laden flows. Bull. Amer. Phys. Soc. (abstract only), in press.

Wu, J.-S. and Faeth, G.M. (1995) Predictions of turbulence generation by particles in homogeneous dilute dispersed flows. AIAA J., submitted.

Participants:

Chen, W.-H., Graduate Student Research Assistant and Doctoral Candidate, The University of Michigan.

Chou, W.-H., Graduate Student Research Assistant and Doctoral Candidate, The University of Michigan.

Faeth, G.M., Principal Investigator, Professor, The University of Michigan.

Hsiang, L.-P., Graduate Student Research Assistant and Doctoral Candidate (1992-94), Post-Doctoral Research Fellow (1994-95), The University of Michigan.

Wu, J.-S., Graduate Student Research Assistant and Doctoral Candidate (1992-94), Post-Doctoral Research Fellow (1994-95), The University of Michigan.

Oral Presentations:

Faeth, G.M., "Aerodynamic effects on primary and secondary spray breakup," First International Symposium on Liquid Rocket Combustion Instability," The Pennsylvania State University, University Park, PA, 1993, invited.

Faeth, G.M., "Aerodynamic effects on primary and secondary breakup of sprays," Mechanical Engineering Department, Hiroshima University, Hiroshima, Japan; Mechanical Engineering Department, Kyoto University, Kyoto, Japan; Toyota Central Research Laboratory, Nagoya, Japan; 1993, invited.

Faeth, G.M., "Sphere wakes at moderate Reynolds numbers in a turbulent environment," 45th Annual Meeting, APS Division of Fluid Dynamics, Tallahassee, FL, 1992.

Faeth, G.M., "Deformation and secondary breakup of drops," AIAA 31st Aerospace Sciences Meeting, Reno, NV, 1993.

Wu, J.-S., "Effects of ambient turbulence intensity on sphere wakes at intermediate Reynolds numbers," 46th Annual Meeting, APS Division of Fluid Dynamics, Albuquerque, NM, 1993.

Faeth, G.M., "Drop deformation and secondary breakup," Institute for Armament Technology, Pune, India, 1994, invited.

Faeth, G.M., "Turbulent primary breakup of pressure-atomized sprays," Institute for Armament Technology, Pune, India, 1994, invited.

Hsiang, L.-P., "Drop deformation and breakup induced by gradual disturbances," AIAA 32nd Aerospace Sciences Meeting, Reno, NV, 1994.

Faeth, G.M., "Drop deformation and secondary breakup near the thermodynamic critical point." Supercritical Fuels/Combustion Workshop, Wright Laboratory, Wright-Patterson AFB, OH, 1994.

Faeth, G.M., "Near-limit drop deformation and secondary breakup." AFOSR Contractors' Meeting on Propulsion, Lake Tahoe, NV, 1994.

Faeth, G.M., "Spray combustion: a review." Second International Conference on Multiphase Flow, Kyoto, Japan, 1995, invited.

Faeth, G.M., ""Research issues in hydrocarbon combustion." ARO Workshop, Myrtle Beach, SC, 1995, invited.

Faeth, G.M., "Dynamic properties of secondary drop breakup," AFOSR Workshop on Supercritical Phenomena, Ann Arbor, MI, 1995.

Faeth, G.M., "Dense-spray structure and liquid breakup." General Motors Research Laboratories, Warren, MI, 1995, invited.

Faeth, G.M., "Primary breakup at the surface of turbulent liquids," ONR Workshop on Free-Surface Turbulent Flows, California Institute of Technology, Pasadena, CA, 1995.

Faeth, G.M., "Temporal variation of drop properties and formation rates during secondary breakup." 31st Joint Propulsion Conference and Exhibit, San Diego, CA, 1995.

Hsiang, L.-P., "Dynamic properties of secondary drop breakup," ILASS-AMERICAS-95, Troy, MI, 1995.

Honors/Awards:

Faeth, G.M., Best Propellants and Combustion Paper Presented at the AIAA 32nd Aerospace Sciences Meeting, AIAA, 1995

Faeth, G.M., Best Paper Presented at the 29th National Heat Transfer Conference, ASME, 1995

Faeth, G.M., Propellants and Combustion Award, AIAA, 1993

Faeth, G.M., Stephen S. Attwood Award, The University of Michigan, 1993

Faeth, G.M., Distinguished Engineering Faculty Research Award, The University of Michigan, 1992

---

2. SECONDARY BREAKUP

2.1 Introduction

Secondary breakup of drops is an important fundamental process of multiphase flows with applications to liquid atomization, dispersed multiphase flow, spray drying, combustion instability, heterogeneous detonations, the properties of rain and interactions between missiles or vehicles and rain, among others. In particular, recent studies of the structure of dense sprays confirm the conventional view of liquid atomization that primary breakup at the liquid surface yields drops that are intrinsically unstable to secondary breakup; and that secondary breakup tends to control mixing rates in dense sprays in much the same way that drop vaporization tends to control mixing rates in dilute sprays, see Ruff et al. (1989, 1992, 1992), Faeth (1987, 1990, 1995, 1996), Faeth et al. (1995) and references cited therein. Motivated by these observations, the objectives of this phase of the investigation were to study drop deformation and breakup for well-defined shock-wave and steady disturbances.

Reviews of past work on secondary breakup are reported by Hinze (1955), Krzeczkowski (1980), Faeth (1987, 1990, 1995, 1996), Faeth et al. (1995) and Hsiang

and Faeth (1992). These reviews indicate that the regimes of drop deformation and breakup have been defined reasonably well when effects of liquid viscosity are small (low Oh conditions), and that breakup times have been measured for a wide range of conditions. However, the outcomes of breakup, i.e., drop size and velocity distributions after breakup, are not known very well. Thus, deformation and breakup regimes at large Oh, and the outcomes of breakup, were emphasized during the present investigation. The methodology involved experiments in shock tubes, to simulate effects of step changes of drop conditions, and steady drop towers, to simulate effects of gradual changes of drop conditions. In both cases, phenomenological theories were used to help interpret and correlate the measurements. The present description of the research is brief, see Hsiang (1994), Hsiang and Faeth (1992, 1993, 1995) and Chou et al. (1995) for more details.

2.2 Experimental Methods

Apparatus. A shock tube with the driven section open to the atmosphere, sketched in Fig. 1, was used to generate shock-wave disturbances. The driven section was rectangular (38 × 64 mm) with a 6.7 m length to provide 17-24 ms of uniform flow behind the shock wave for test purposes. Shock strengths were relatively weak; therefore, gas flow properties acting on the test drops approximated air at normal temperature and pressure.

Two different drop generator systems were used. Operation at low Oh involved a vibrating capillary tube drop generator with electrostatic selection to control the drop spacing; this provided a continuous drop stream to interact with the shock wave at the test location. Operation at large Oh involved acoustic levitation of a drop at the test location, allowing evaporation of a solvent in a solvent and viscous liquid mixture to yield a small, highly viscous, large Oh drop for interaction with the shock wave.

Tests of effects of steady disturbances were carried out in gas-liquid and liquid-liquid drop towers. The gas-liquid drop tower had a diameter of 300 mm with a length of 9.2 m which yielded nearly steady terminal velocity behavior at the bottom of the tube where measurements were made. The liquid-liquid drop tower had a 150 × 150 mm cross section with a vertical height of 1.2 m which also allowed observation of terminal velocity conditions for immiscible drops near the bottom of the tube. Drop formation involved a simple discharge of the test liquid from a buret in both cases.

Instrumentation. Drops were observed in two ways: pulsed shadowgraph photographs and motion pictures to observe overall breakup dynamics and single- and double-pulse holography to observe the outcome of breakup. See Hsiang and Faeth (1992, 1993, 1995) for the details and experimental uncertainties of these measurements.

2.3 Results and Discussion

The presentation of results will begin with definitions of deformation and breakup regime transitions to help organize the rest of the findings. These transitions are plotted in Fig. 2 as functions of We and Oh, following the earlier work of Hinze (1955) and Krzeczkowski (1980). Present findings are similar to Hsiang and Faeth (1992) but extend results from Oh ~ 10^0 to Oh ~ 10^3. The new results address behavior during high-pressure combustion processes where Oh becomes large because surface tension becomes small, while the liquid viscosity remains finite, due to approach of drops to their thermodynamic critical points.
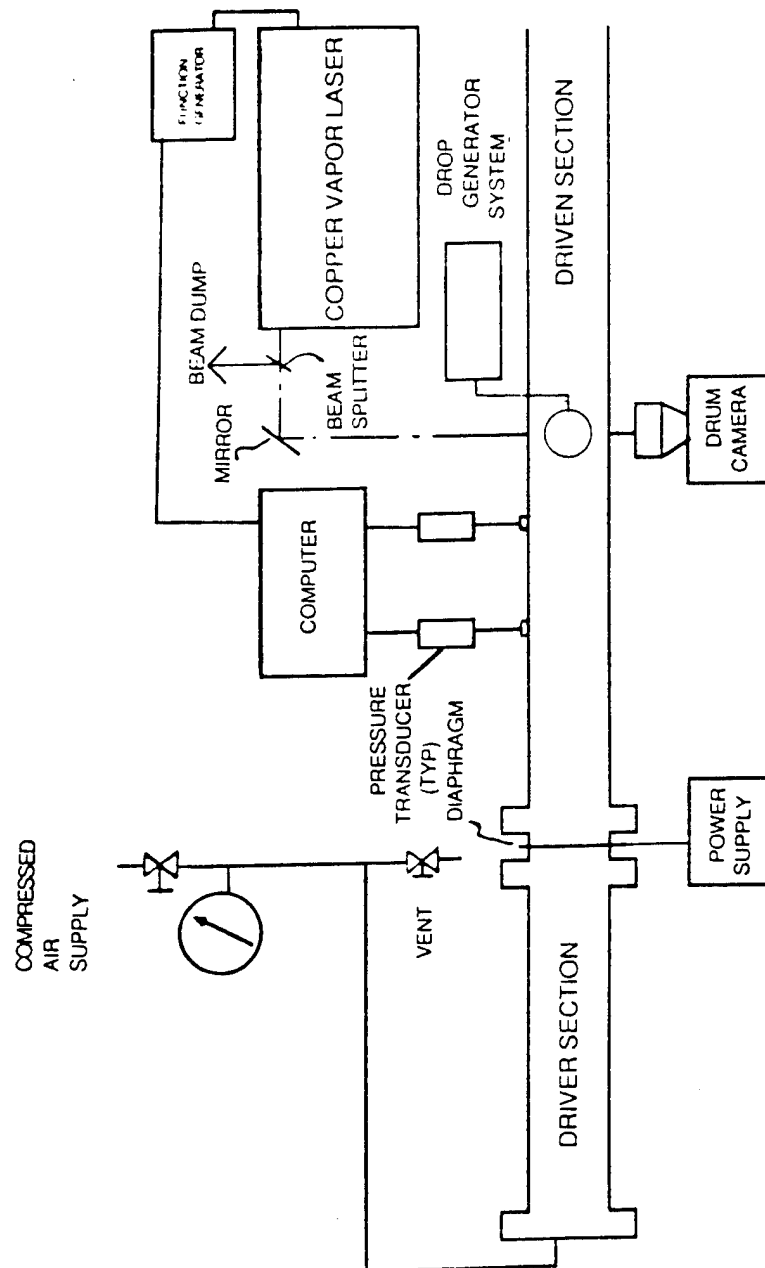
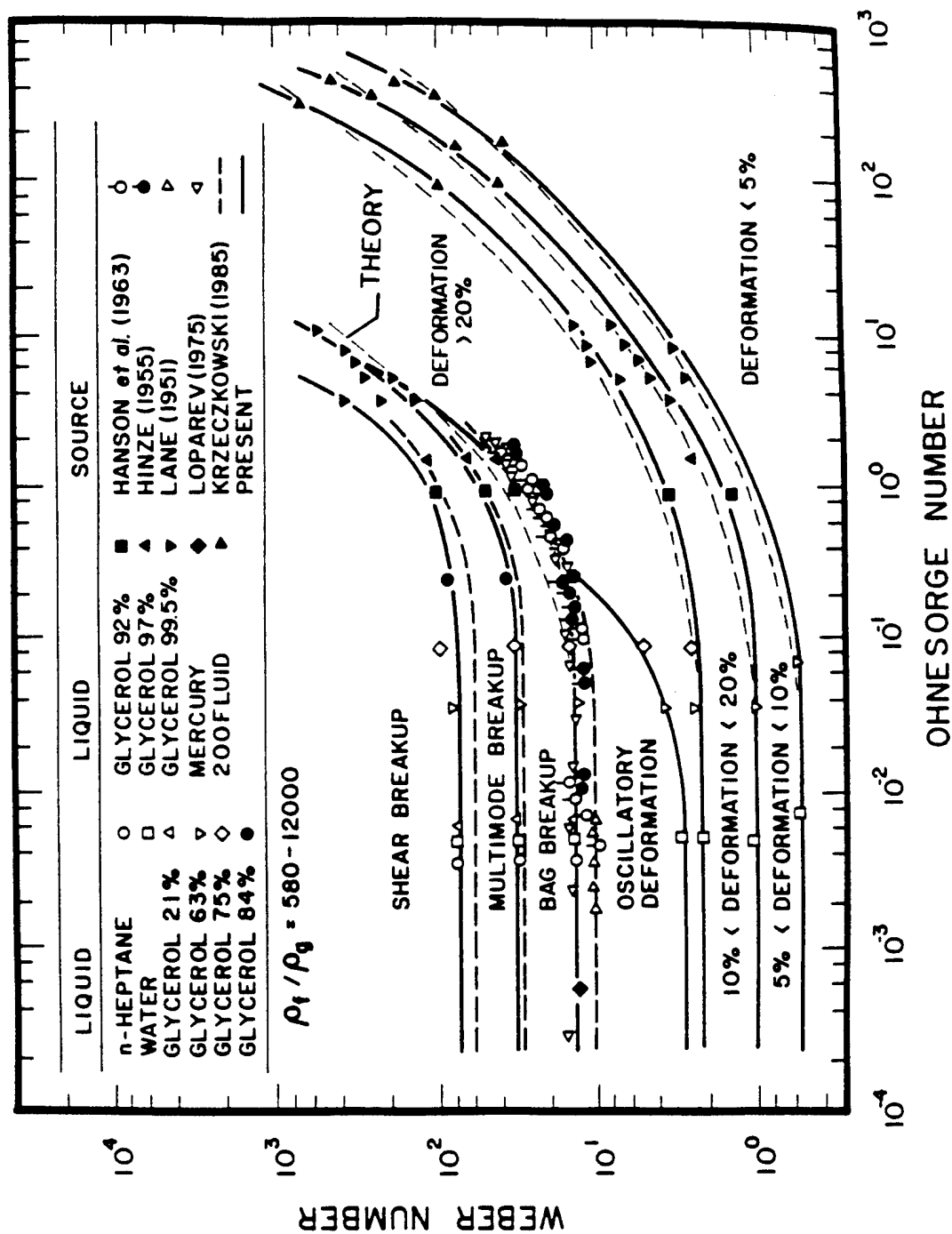Figure 1   Sketch of the shock tube apparatus.

Figure 2   Drop deformation and breakup regime map for shock wave disturbances.

At low Oh in Fig. 2, drops begin to deform at We ~ 1. Subsequently, three breakup regimes can be delineated: bag breakup beginning at We ~ 13, where the center of the drop deforms in the downstream direction; shear breakup beginning at We ~ 80, where ligaments and drops are stripped from the periphery of the original drop; and multimode breakup beginning at We ~ 35, which is a complex combination of bag and shear breakup. In view of the somewhat arbitrary definitions of these regimes, the agreement between the present breakup regime transitions and those of Hinze (1955) and Krzeczkowski (1980) is quite satisfying.

The most striking feature of the deformation and breakup regime map illustrated in Fig. 2 is that progressively higher We numbers are needed for the various transitions as Oh increases. This behavior can be explained by noting that increasing liquid viscosity reduces the rate of deformation of the drop. This behavior allows more time for drop relaxation to the local ambient velocity, tending to reduce the relative velocity and thus the driving potential for drop deformation at each stage of the deformation process. A phenomenological analysis based on these ideas is developed by Hsiang and Faeth (1995); results illustrated in Fig. 2 show that this analysis provides an effective correlation of the increased We required for a particular transition as Oh increases. Notably, these results suggest that transition We ~ Oh at large Oh, rather than reaching an ultimate limit at a particular Oh, as suggested by Hinze (1955). This difference in behavior has significant relevance for processes of high-pressure combustion, as noted earlier. Surprisingly, the result suggests increased resistance to drop breakup as the critical point is approached, rather than the rapid breakup which is assumed in current models of high-pressure combusting sprays Faeth (1990, 1996).

Similar to past work on the structure of dense sprays and processes of primary breakup (Ruff et al. 1992; P.-K. Wu et al. 1993); drop size distributions after secondary breakup generally satisfied the universal root normal distribution with MMD/SMD = 1.2 due to Simmons (1977), see Hsiang and Faeth (1992). Shear breakup was an exception when the parent (or drop-forming drop was considered; however, this deficiency could be eliminated by removing the parent drop from the distribution and treating it separately (Hsiang and Faeth 1993). Thus, the entire drop size distribution can be represented by the SMD alone, which is the practice that will be used in the following.

A correlation for the sizes after secondary breakup was developed based on phenomenological analysis of shear breakup that served equally well for the bag and multimode breakup processes (Hsiang and Faeth 1992). Present measurements of drop sizes after secondary breakup are illustrated according to this correlation in Fig. 3. These results are for Oh < 0.1 and We < 10^3, and yield the following fit:

$$\rho_G \, SMD \, u_o^2 / \sigma = 6.2 \, (\rho_L / \rho_G)^{1/4} [\mu_L/(\rho_L \, d_o \, u_o)]^{1/2} \, We \qquad (1)$$

with an overall correlation coefficient of the fit of 0.91. It should be noted, however, that ρ_L/ρ_G does not vary greatly over the present test range and additional measurements are needed to explore density ratio effects. In addition, it probably is fortuitous, and certainly surprising, that a single correlation can express the SMD after bag, multimode and shear breakup.

The coordinates of Fig. 3 were selected to highlight the values of We of the drops, assuming that velocity changes during breakup were negligible. The results suggest that drops resulting from secondary breakup continue to exceed the breakup criterion for a shock-wave disturbance in most instances; nevertheless, these drops actually are stable to additional breakup up due both to changes of their velocities and different criteria for
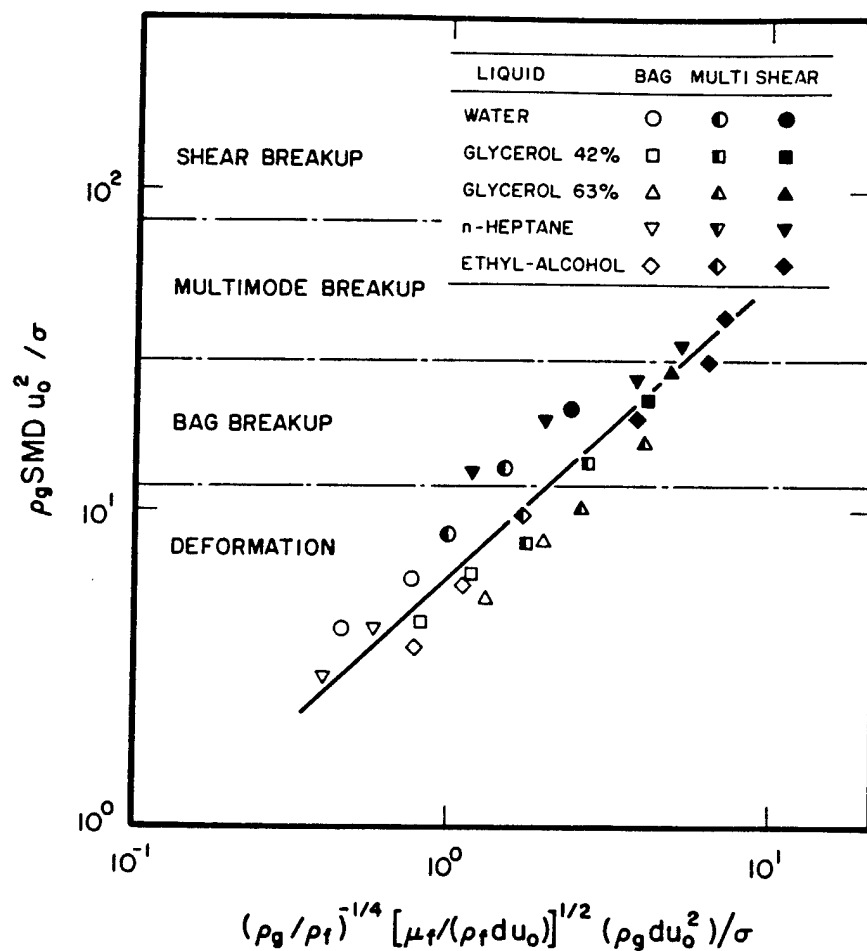
Figure 3   Correlation of SMD after secondary breakup due to shock wave disturbances.

breakup for the more gradual disturbances present hear the end of breakup — these issues will be considered directly. Upon rearrangement, the correlation of Eq. 1 can be rewritten in a form that better indicates the properties controlling drop sizes after secondary breakup, as follows:

$$SMD/d_o = 6.2 \, (\rho_L/\rho_G)^{1/4} \, [\mu_L/(\rho_L d_o u_o)]^{1/2} \tag{2}$$

Equation 2 emphasizes the surprising finding that while the onset of breakup depends on the surface tension of the liquid, the resulting drop sizes are independent of the surface tension and are mainly influenced by the viscosity of the liquid!

The properties of the parent (drop-forming) drop were studied in order to gain insight about the processes that cause secondary breakup to stop. Study of parent drop velocities showed that relative velocities were reduced 30-40% during the breakup period; this behavior was successfully correlated by a phenomenological analysis. The reduced size and relative velocity of the parent drop at the time breakup ended, however, still implied We in excess of the breakup criterion for shock-wave disturbances in most instances. Instead, the end of drop stripping was best characterized by a particular value of the Eötvös number, namely Eo = 16, which is very similar to the breakup criterion for gradual disturbances, as might be expected.

Given the breakup regime map, parent drop sizes and velocities after shear breakup, and drop sizes after breakup, the last secondary breakup jump condition to be resolved is the drop velocity distribution after breakup. Drop velocity properties were correlated based on a phenomenological analysis similar to the one used for parent drop velocities after breakup. The resulting correlation is illustrated in Fig. 4. These results involve a variety of drop liquids and all three breakup regimes — bag, multimode and shear breakup. Results for parent drops also are shown on the figure by dark symbols; these results scatter significantly from the rest and are best treated using the parent drop velocity correlation discussed earlier. The remaining drops yield an excellent velocity correlation that accounts for the 30-70% reduction of relative velocities of drops during breakup and the fact that the smallest drops experience the largest relative velocity reduction due to their smaller relaxation times.

Results about jump conditions for secondary breakup indicated that this process was not particularly localized in time and space. For example, drop breakup typically requires 5.5 t* while the parent drop moves roughly 40 d_o during shear breakup (Hsiang and Faeth 1992, 1993). Thus, subsequent work has focused on treating secondary breakup as a rate process rather than by jump conditions. An initial report of these results, giving drop size velocities and formation rates as a function of time during breakup, is presented by Chou et al. (1995).

The importance of the rate aspects of secondary breakup can be seen from the results plotted in Fig. 5, which is an illustration of the growth of the spray-containing region as a function of time during shear breakup. These boundaries are given by the motion of the parent drop and by the motion of the smallest drops that are formed at the onset of breakup (which occurs at 1.5 t*). When these paths are plotted in the manner of Fig. 5, ρ_f/ρ_g is the only parameter of the problem. Thus, boundaries of the drop-containing region are shown for $\rho_f/\rho_g = 500$ and 1000, which bound the present test range. The results show how the span of the drop-containing region increases with both liquid/gas density ratio and time, reaching x/d = 40-120 at the end of breakup for $\rho_f/\rho_g = 1000$. This
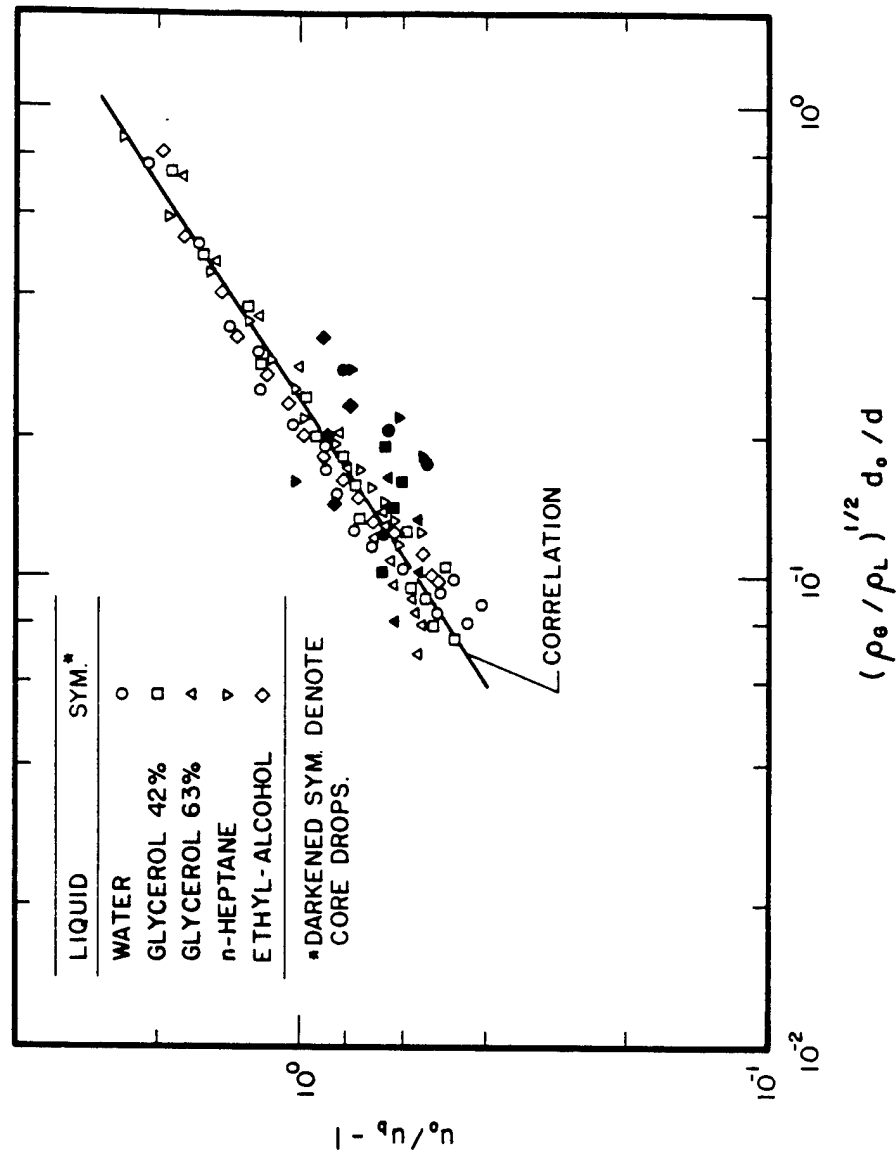
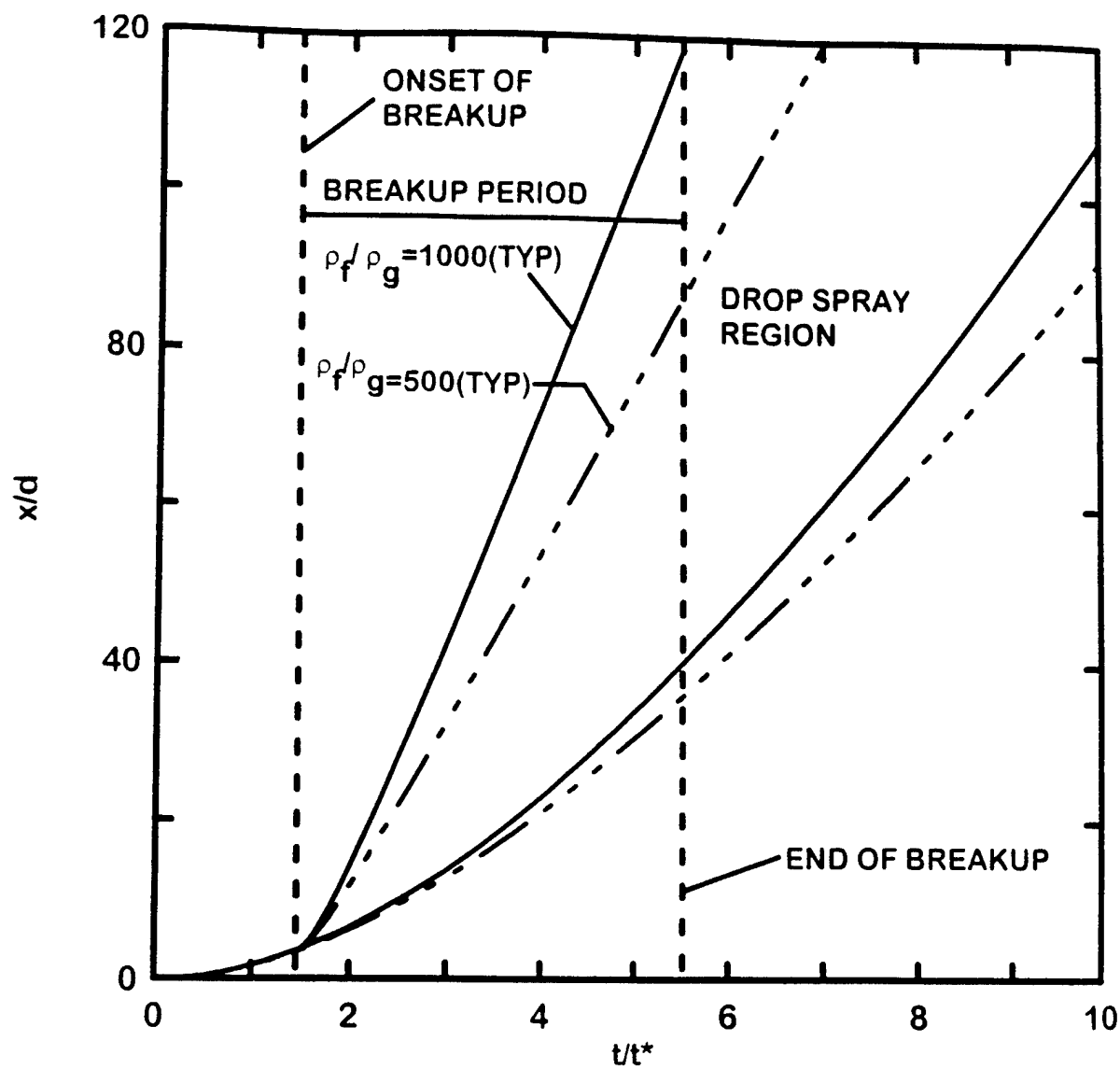Figure 4   Correlation of drop velocities after secondary breakup due to shock wave disturbances.

Figure 5   Growth of the spray-containing region during shear breakup due to shock wave disturbances.

finding clearly emphasizes the need to treat secondary breakup as a rate process rather than by jump conditions, in most instances.

2.4 Conclusions

Drop deformation and secondary breakup as a result of both shock wave and gradual disturbances were studied for a variety of liquids in air at normal temperature and pressure. The major conclusions of the study are as follows:

1. The We for the onset of deformation and breakup regimes increased with increasing Oh, and became proportional to Oh at large values of this parameter. This finding suggests that drops do not shatter as they approach their thermodynamic critical point during high-pressure combustion, as generally thought (Faeth 1990); instead, they simply deform or may even remain spherical if Oh is large enough.

2. Drop size distributions after secondary breakup satisfied the universal root normal distribution of Simmons (1977) with MMD/SMD = 1.2, excluding the parent drop during shear breakup; therefore, drop size distributions can be characterized by a single parameter which was taken to be the SMD during present work.

3. The SMD after secondary breakup, at Oh < 0.1 and ρ_f/ρ_g > 500 were correlated effectively in all three breakup regimes, using a phenomenological analysis of shear breakup. Remarkably, the SMD was independent of surface tension, and was mainly dependent on liquid viscosity, see Eq. 2, even though surface tension controls the criteria for the onset of various breakup regimes.

4. The properties of the parent drop after shear breakup must be treated differently from the other drops and were successfully correlated using phenomenological theory. In this case, the end of shear breakup was defined by the condition that Eo = 16 for the parent drop, which is very similar to the criterion for stable drops subjected to gradual disturbances.

5. The velocities of drops after secondary breakup at Oh < 0.1 and ρ_f/ρ_g > 500 were correlated effectively in all three breakup regimes, using a phenomenological analysis of shear breakup. These results indicated that relative velocities were reduced 30-70% during the time of breakup.

6. Secondary breakup was not found to be a particularly localized event in either time or space. For example, breakup times are 5.5 t* and drops are spread over a region x/d = 40-120 for ρ_f/ρ_g = 1000. Thus, secondary breakup should be treated as a rate process, rather than by jump conditions, in most instances.

In view of these findings, current work is emphasizing the dynamic properties of secondary breakup, e.g., the drop size and velocity distributions and the rate of drop formation as a function of time during secondary breakup. Current work also is addressing test conditions at larger Oh and smaller ρ_f/ρ_g, that are more representative of combusting sprays at the elevated pressures of contemporary propulsion systems.

3. SPHERE WAKES

3.1 Introduction

The wake flow of spheres has attracted attention due to numerous applications, e.g., dispersed particle-laden flows, sprays and rainstorms, among others. Work on turbulence generation by dispersed phases has shown, however, that there is a need for more information about sphere wakes at intermediate Reynolds numbers ($10 < Re < 1000$) typical of drops in sprays (Parthasarathy and Faeth 1990a,b). This prompted earlier measurements of the structure of sphere wakes at intermediate Reynolds numbers in nonturbulent environments (J.-S. Wu and Faeth 1993). The objective of this portion of the investigation was to extend this work to sphere wakes in turbulent environments that are more representative of conditions within practical dispersed multiphase flows.

Past research on the flow near spheres and in sphere wakes for intermediate sphere Reynolds numbers in nonturbulent environments is reviewed by J.-S. Wu and Faeth (1993) and references cited therein These studies have identified conditions where vortex shedding is present, the structure of turbulent wakes, conditions for transition to laminar wakes, and the structure of laminar wakes. An interesting feature of these results is that the transition between turbulent and laminar wakes occurs at a rather low wake Reynolds number (based on the characteristic wake width and centerline velocity defect) of roughly 10. On the other hand, comparable studies of wakes for intermediate Reynolds numbers in turbulent environments are limited and do not include consideration of the wakes of axisymmetric objects such as spheres.

Based on these observations, the present experimental investigation was undertaken to better understand the properties of sphere wakes at intermediate Reynolds numbers in turbulent environments. The study involved laser-velocimetry measurements of the structure of sphere wakes within stationary turbulence fields generated by a variety of wind tunnels. The present description of the research is brief, see J.-S. Wu (1994) and J.-S. Wu and Faeth (1993, 1994, 1995a) for additional details.

3.2 Experimental Methods

Apparatus. The sphere wakes were observed within regions having relatively constant turbulence properties using a variety of wind tunnels. These arrangements consisted of round tubes with either perforated disks along the axis or with fully-developed turbulent pipe flow present in the tube. The test spheres were polished plastic balls with diameters in the range 1-6 mm. The spheres were held by thin stainless steel wires that passed through the center of the spheres and were sealed with epoxy. The spheres were mounted in tension between two struts passing near the top and bottom of the wind tunnels, just beyond their exit, with provision for traversing the struts in order to accommodate a rigidly-mounted laser velocimeter. Flow rates were controlled by a variable-speed blower.

Instrumentation. Wake structure measurements were carried out using a dual-beam, forward-scatter, frequency-shifted laser velocimeter with the measuring volume centered on the wind tunnel axis. The sending optics included a beam expander that yielded measuring volume having a diameter and length of 50×300 µm. The flow was seeded with oil drops (1 µm nominal diameter) at the inlet of the blower. Velocities were found from the low-pass filtered analog output of a burst-counter signal processor.

A traversible dual-beam, forward-scatter, frequency-shifted laser velocimeter was used to measure the structure of the turbulent flow that surrounded the wake flow. Other aspects of these measurements were the same as the laser velocimeter measurements of sphere wake properties.

3.3 Results and Discussion

Sphere wakes at moderate Reynolds numbers in turbulent environments exhibited a number of surprising features. The first of these was that the wake flows generally scaled in a manner that satisfied laminar wake similarity even though the wakes were clearly turbulent. In this case, effects of turbulence were observed as effective (turbulent) viscosities that were larger (in many cases much larger) than molecular viscosities. Thus, these flows have been termed "laminar-like turbulent wakes."

Some typical radial profiles of mean streamwise velocities in laminar-like turbulent wakes are illustrated in Fig. 6. These results are plotted according to the classical similarity analysis of self-preserving round laminar wakes that have constant viscosities (J.-S. Wu and Faeth 1992; Schlichting 1977; and Tennekes and Lumley 1972), which implies:

$$\bar{u}/\bar{U}_t = [d/(x-x_o)]\exp(-r^2/(2\,\ell^2))$$ (3)

where the wake-scaling velocity and characteristic wake width are

$$\bar{U}_t/\bar{U}_\infty = C_d Re_t/32$$ (4)

$$\ell/d = [2(x-x_o)/(d\,Re_t)]^{1/2}$$ (5)

and the turbulence Reynolds number is given by

$$Re_t = d\bar{U}_\infty/\nu_t$$ (6)

where the effective turbulence viscosity has been selected to best fit the data. It is evident that the measurements correlate quite nicely according to the behavior of self-preserving round laminar wakes but with the effective turbulence viscosity replacing the laminar viscosity. As noted earlier, the effective turbulence viscosity is independent of position within the wake; however, subsequent results will show that this property varies with both the sphere Reynolds number and the ambient turbulence intensity.

Typical measurements of mean streamwise velocities along the axis of sphere wakes in turbulent environments are illustrated in Fig. 7. These results are for an ambient turbulence intensity of 4%, but results at other turbulence intensities were similar. Three wake regions are observed: (1) a near-wake region, (2) a laminar-like turbulent wake region which is the most prominent of the three, and (3) a final-decay region. The near-wake region (for $(x-x_o)/d < 2$) exhibits effects of vortex shedding for Re in the range 300-600. The final-decay region (for $(x-x_o)/d > 100$) for the conditions of Fig. 7) begins where the mean streamwise velocity defect is comparable to the ambient velocity fluctuations. This region exhibits a faster decay rate than any other axisymmetric wake flow observed thus far (J.-S. Wu and Faeth 1993, 1994). This fast-decay behavior is very significant because the high power law decay rate in the fast-decay region allows use of
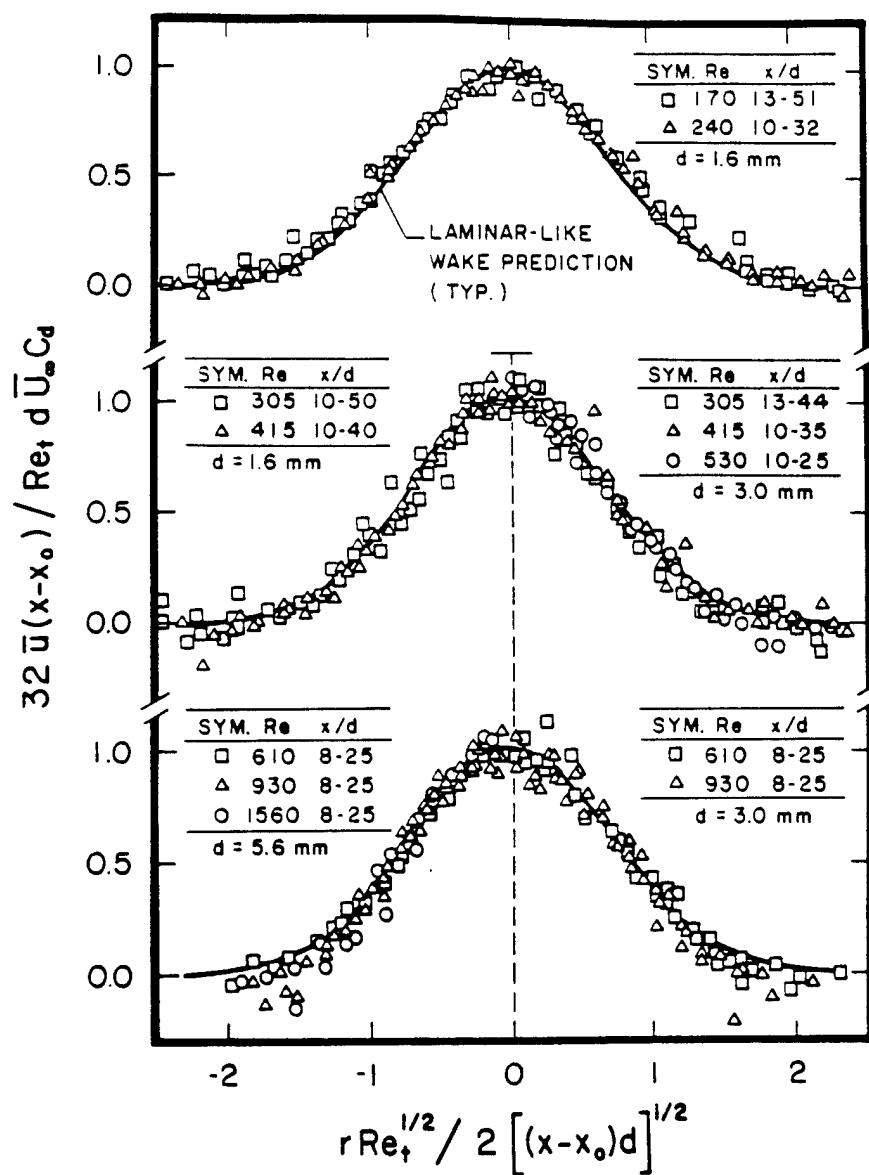
Figure 6   Typical radial profiles of mean streamwise velocities of sphere wakes at intermediate Reynolds numbers in a turbulent environment.

	d (mm)	
	1.2	1.6
SYM.	Re	SYM.	Re
□	135	■	170
△	210	▲	240

	d (mm)		
	1.2	1.6	3.0
SYM.	Re	SYM.	Re	SYM.	Re
□	315	■	305	◧	300
△	400	▲	410	△	415
				●	530

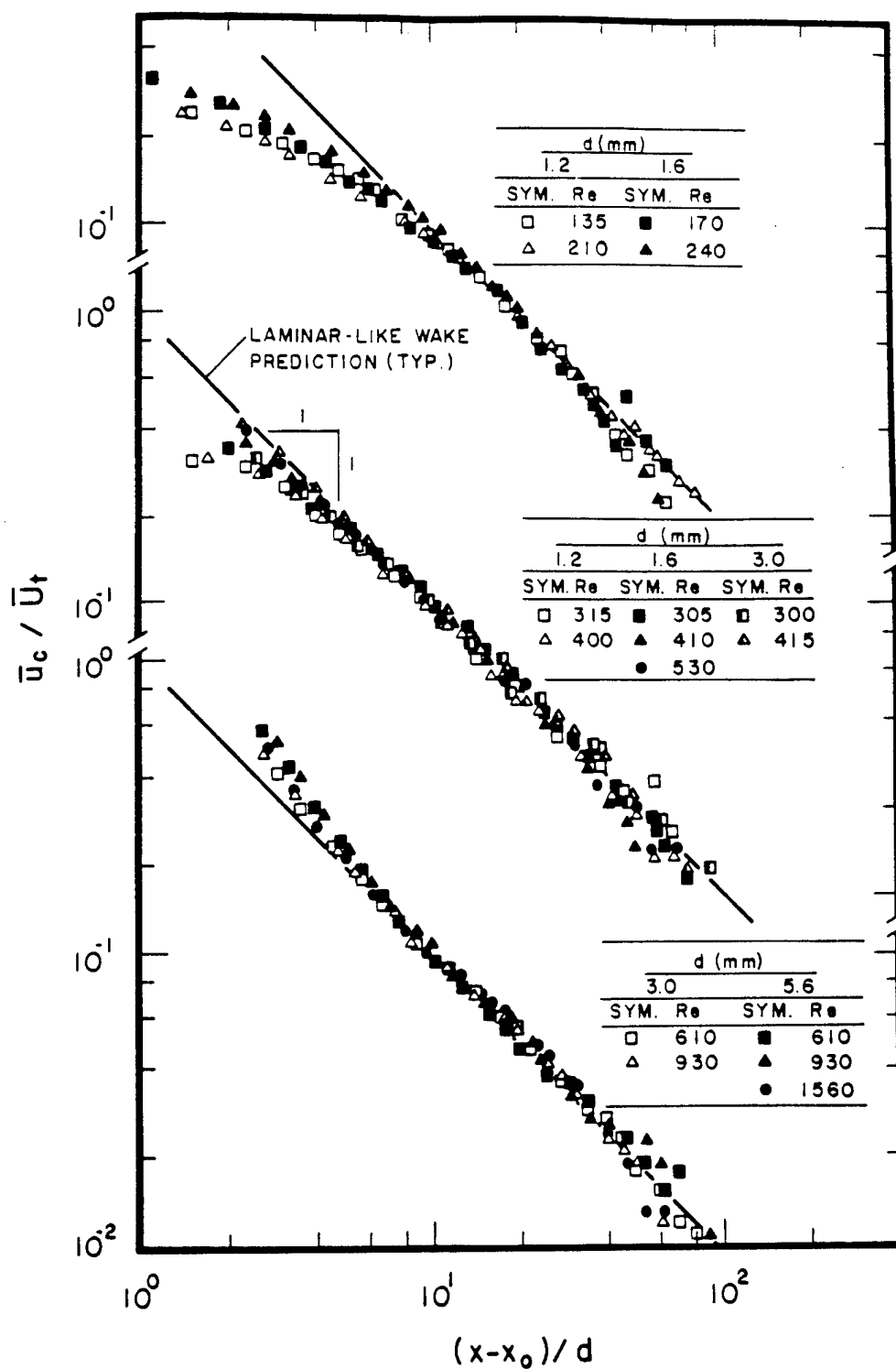|	d (mm)	
	3.0	5.6
SYM.	Re	SYM.	Re
□	610	■	610
△	930	▲	930
		●	1560

Figure 7   Mean streamwise velocities along the axis of sphere wakes at intermediate Reynolds numbers in a turbulent environment for $(\overline{u}'/\overline{u})_\infty = 4.0\%$.

Campbell's theorem to superimpose wake properties in order to find effects of turbulence generation by dispersed phases, see Parthasarathy and Faeth (1990a,b).

Effects of vortex shedding, wake turbulence, and ambient turbulence can be seen from the cross stream velocity fluctuations along the wake axis is plotted in Fig. 8. The results illustrated in Fig. 8 can be separated into three regimes: (1) prior to the onset of vortex shedding (Re < 300) velocity fluctuations in the wake are small, comparable to the ambient velocity fluctuations; (2) when effects of vortex shedding are observed in the near-wake temporal spectra (300 < Re < 600), the velocity fluctuations progressively increase with increasing Re; and (3) at high Re (Re > 600) where effects of vortex shedding are no longer observed in the near-wake temporal spectra, the velocity fluctuations are large and independent of Re, which is typical of behavior in turbulent wakes, see J.-S. Wu and Faeth (1993). In the high Re regime, values of velocity fluctuations are substantially enhanced from ambient turbulence levels near the start of the laminar-like turbulent wake region, however, they progressively decrease and reach ambient turbulence levels at the start of the final-decay region.

The value of the effective turbulent viscosity, v_t, clearly is the critical parameter needed to estimate laminar-like turbulent wake properties. It was found that these results can be correlated in terms of Re and $(\overline{u}'/\overline{U})_\infty$ as illustrated in Fig. 9. Similar to the other turbulence properties of laminar-like turbulent wakes, it is evident that v_t, exhibits low, transition and high Re regimes that are associated with vortex shedding behavior. The variation of v_t/v with Re is nearly linear for a given $(\overline{u}'/\overline{U})_\infty$ in the low Re range, with v_t/v progressively increasing as $(\overline{u}'/\overline{U})_\infty$ increases. This can be explained based on crude mixing length concepts. Thus, $v_t/v \sim \overline{v}' \ell$ while $\overline{v}' \sim \overline{v}'_\infty$ before vortex shedding begins whereas $\ell \sim d$ because the sphere size tends to control the flow width in the critical region near the start of the laminar-like turbulent wake. As a result, $v_t - v \sim \overline{v}'d \approx (\overline{v}'/U)_\infty U_\infty d$ or $v_t/v-1 \sim Re(\overline{u}'/U)_\infty$, since $\overline{v}'_\infty \sim \overline{u}'_\infty$, as observed in Fig. 9.

The variation of v_t/v also is nearly linear in Re in the high Re region but is less dependent on $(\overline{u}'/\overline{U})_\infty$. This behavior can also be explained by the mixing length argument, noting that $v_t >> v$ in the high Re regime. Then, $v_t/v \sim \overline{v}' \ell/v$ and in the laminar-like turbulent wake, $\overline{v}' \sim \overline{U}_\infty >> \overline{u}'_\infty$, see Fig. 8. Then estimating $\ell \sim d$, as before, $v_t/v \sim \overline{U}_\infty d/v = Re$, generally as observed in Fig. 9. Finally, the intermediate Re regime represents a branch region where turbulence properties make the transition between low and high Re behavior. Based on this discussion, the behavior of v_t/v seen in Fig. 9 is quite plausible, see J.-S. Wu and Faeth (1995a) for a more complete discussion about the properties of v_t/v.

3.4 Conclusions

Sphere wakes at intermediate Reynolds numbers (Re of 135 to 1560) in turbulent environments were studied. The major conclusions of the study are as follows:
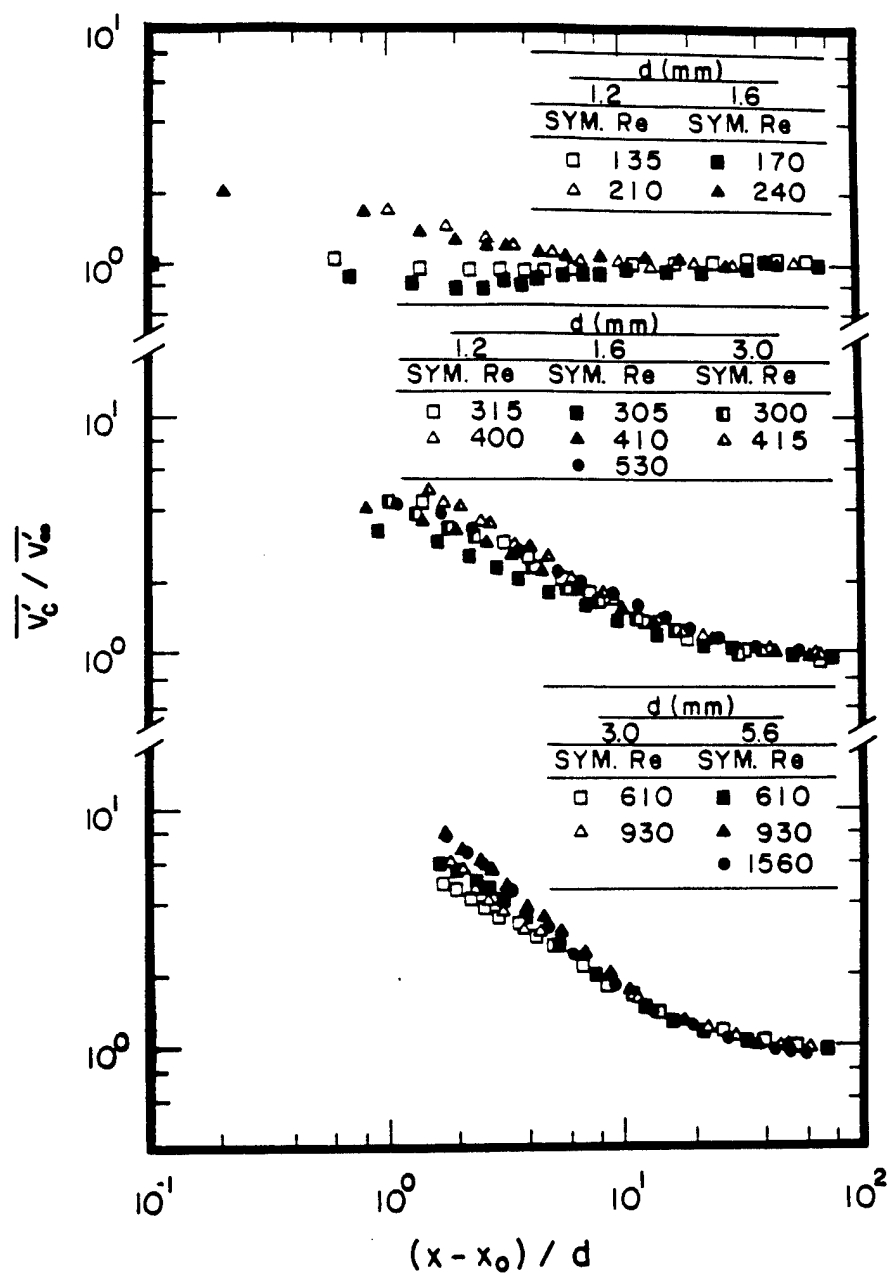
Figure 8   Cross-stream velocity fluctuations along the axis of sphere wakes at inter-
mediate Reynolds numbers in a turbulent environment for $(\overline{u}'/\overline{u})_\infty = 4.0\%$.
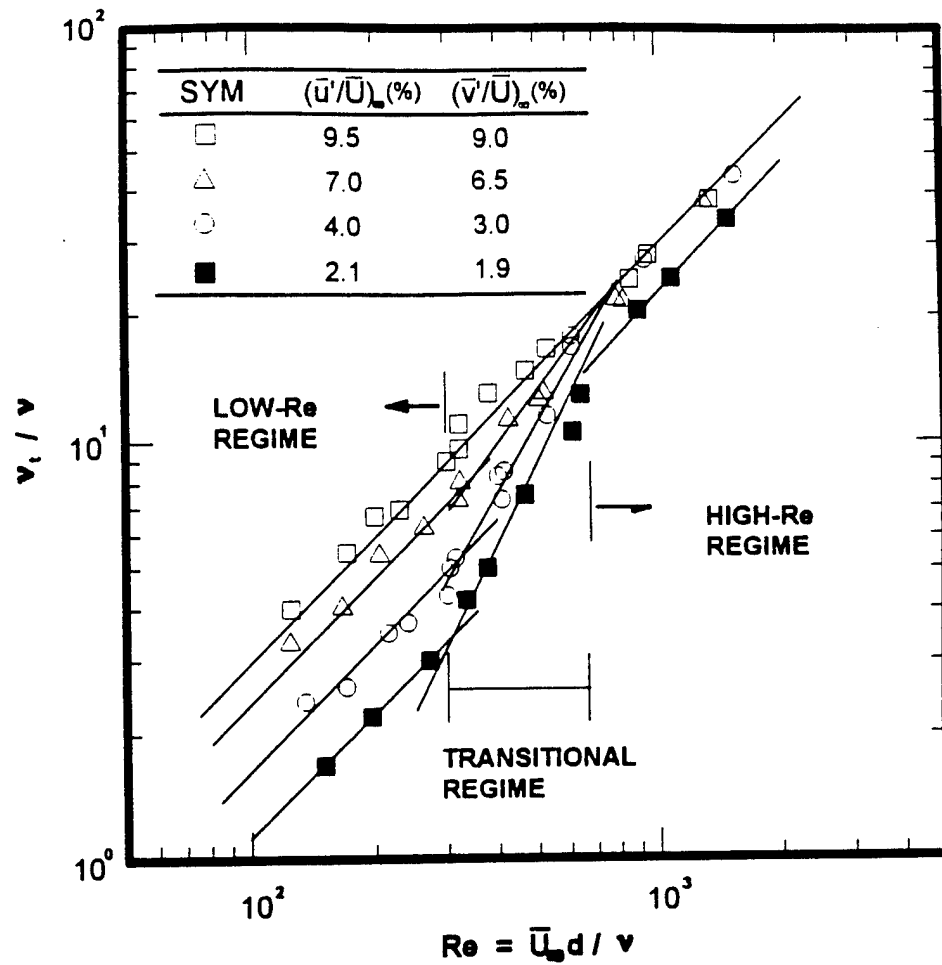
Figure 9   Variation of turbulent viscosity in laminar-like turbulent wakes with sphere
Reynolds number and ambient turbulence intensity.

1. The wakes were turbulent but mean streamwise velocities scaled like self-preserving round laminar wakes with enhanced viscosities due to effects of turbulence; this yielded behavior that was termed laminar-like turbulent wakes.

2. The laminar-like turbulent wake region was followed by a final decay region beginning when $\bar{u}_c \sim \bar{u}'_\infty$, which exhibits faster decay rates than any other axisymmetric wake observed thus far.

3. The effective turbulent viscosities were relatively independent of position but they varied with both Re and $(\bar{u}'/\bar{U})_\infty$ in a low Reynolds number regime (Re < 300), with Re alone in a high Reynolds number regime (Re > 600), with the transition between these regimes associated with significant effects of vortex shedding from the sphere.

There are three main issues that remain to be resolved concerning sphere wakes at intermediate Reynolds numbers in turbulent environments: (1) what are the properties of v_t/v for values of Re < 135 and values of $(\bar{u}'/\bar{U})_\infty > 9.5\%$ and < 2.1%, see Fig. 9; (2) what is the effect of the nature of the ambient turbulence (isotropic, anisotropic and due to particle-generated turbulence); and (3) what are the scalar properties of laminar-like turbulent wakes? Current work is addressing these issues.

4. TURBULENCE GENERATION

4.1 Introduction

Turbulence generation by drops controls the turbulence properties, and thus the mixing properties, within dense sprays (Faeth 1987, 1990, 1995, 1996; Ruff et al. 1989, 1991, 1992). This behavior follows because velocities are relatively uniform, inhibiting the conventional production of turbulence, while the relative velocities of drops are large, which causes significant flow disturbances from drop wakes, within dense sprays.

Drop-generated turbulence is superficially similar to grid-generated turbulence; however, the flows are fundamentally different because drops are distributed throughout the flow, and their arrival at any point is random, yielding a truly stationary turbulent field. In contrast, grids create turbulence at a plane of the flow yielding an unsteady flow that subsequently decays. Thus, drop-generated turbulence is unique compared to conventional turbulence and has been studied very little even though it controls turbulent mixing in the dense sprays found in high-performance air-breathing propulsion systems and liquid rocket engines. Motivated by these observations, turbulence generation was studied during this phase of the present investigation.

Past studies of turbulence generation have considered homogeneous dilute flows (Lance and Bataille 1982; Parthasarathy and Faeth 1990a,b; Mizukami et al. 1992). Lance and Bataille (1982) studied homogeneous air/water bubbly flows downstream of a turbulence-generating grid. Effects of turbulence generation were observed as a progressive increase of turbulence levels with increasing void fractions. These bubbly flows are interesting because they involve turbulence generation by both the dispersed phase and conventional continuous-phase turbulence generation. On the other hand, however, the results are difficult to interpret due to the presence of both mechanisms.

Initial work on turbulence generation in this laboratory is described by Parthasarathy and Faeth (1987, 1990a,b) and Mizukami et al. (1992). Experimental conditions consisted of uniform fluxes of nearly monodisperse spherical glass beads falling at roughly constant speeds in stagnant (in the mean) air and water. Measurements included phase velocities and the turbulence properties of the continuous phase. Turbulence properties were analyzed using a simplified stochastic method based on Campbell's theorem, described by Rice (1954), that involved the synthesis of randomly-arriving particle flow fields (mainly particle wakes). The measurements showed that particle-generated turbulence had rather different properties than conventional turbulence, and involved a large range of length scales even though particle Reynolds numbers (and thus particle wake Reynolds numbers) were modest — less than 1000. The theory helped explain this behavior as the result of the random arrival of wakes so that *mean* wake properties contribute to the apparent random turbulence field. However, while the approximate theory assisted data interpretation, qualitative predictions were not very satisfactory because particle wake properties in turbulent environments were unknown and had to be extrapolated from results for high Reynolds number turbulent wakes in nonturbulent environments. In addition, the scaling laws for wake properties in nonturbulent environments caused convergence problems for the stochastic theory, similar to those encountered when sedimentation is treated using conventional stochastic methods (Batchelor 1972).

The availability of new information about sphere wakes at intermediate Reynolds numbers in turbulent environments provides a new opportunity to study the potential of the stochastic theory. Thus, the objectives of the present study were to complete analysis along these lines, and to use the available measurements of Parthasarathy and Faeth (1990a,b) and Mizukami et al. (1992) to evaluate these predictions. The present discussion of this research will be brief, J.-S. Wu and Faeth (1995) should be consulted for additional details.

4.2 Experimental Methods

Apparatus. In order to help fix ideas about the formulation of the present turbulence generation analysis, the homogeneous particle/air flow experimental apparatus used by Mizukami et al. (1992) is illustrated in Fig. 10. The particles were nearly monodisperse spherical glass spheres having diameters of 0.5, 1.0 and 2.0 mm whose flow was controlled by a variable-speed particle feeder. The particles were dispersed by an array of screens to achieve a uniform particle flux before they fell through a windowed test chamber (410 × 535 × 910 mm) where the measurements were made. The particles collected at the bottom of the test chamber and were removed from time to time. The particles did not reach terminal velocities before entering the test chamber, however, particle velocity changes within the test chamber were small so that the flow was nearly homogeneous. The test arrangement for particle/water flows used by Parthasarathy and Faeth (1990a,b) was nearly the same except that the windowed chamber was filled with water. Results for particle/water flows in various test chambers indicated that effects of the chamber walls were negligible (Parthasarathy and Faeth 1990a,b).

Instrumentation. Measurement techniques for the particle/air and particle/water experiments were essentially the same (Parthasarathy and Faeth 1990a,b; Mizukami et al. 1992). Particle fluxes were measured using particle collection, particle velocities were measured using shadowgraph cinematography, and continuous-phase turbulence properties were measured using two-point phase-discriminating and frequency-shifted laser velocimetry (LV). In the latter case, Kolmogorov scales were comparable to the size of the measuring volume and seeding was sufficient so that turbulence properties could be found
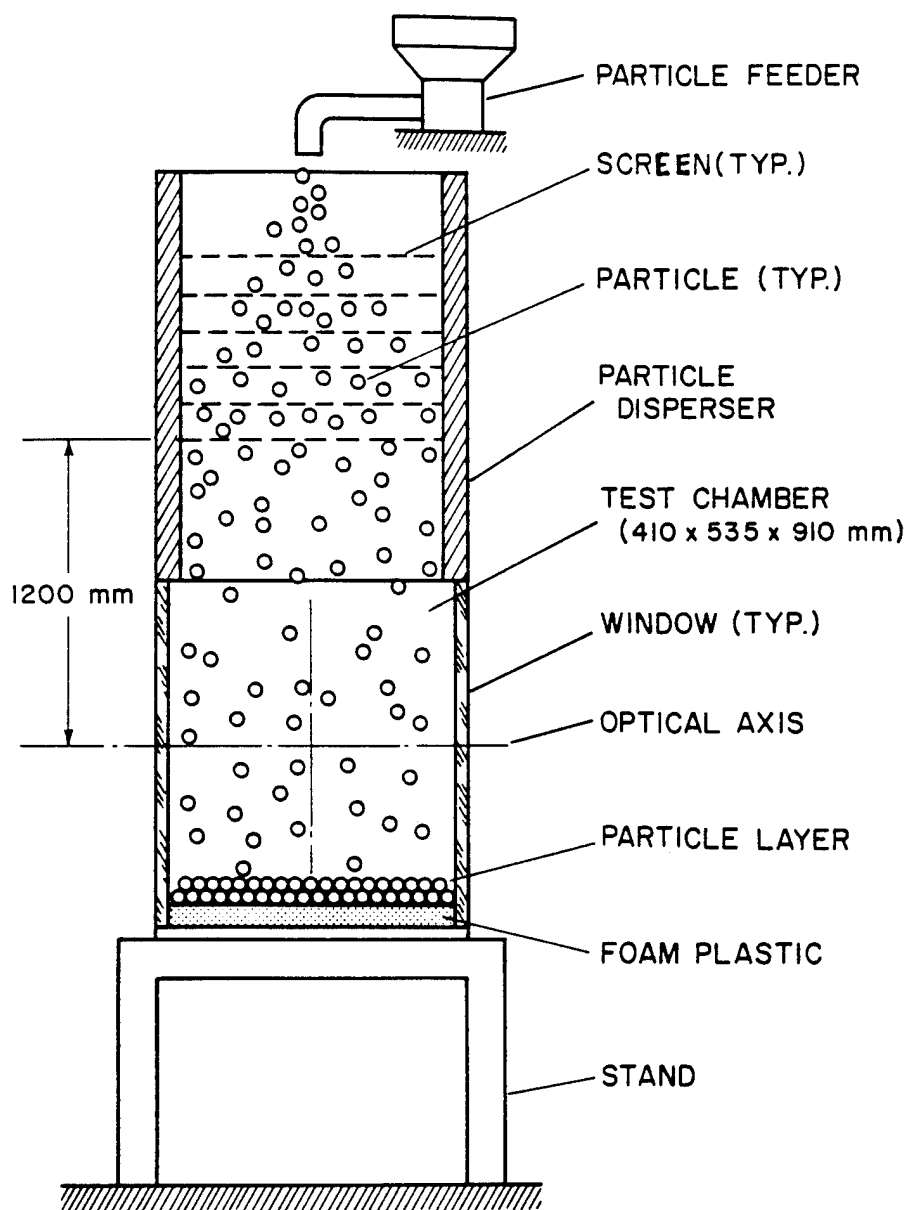
Figure 10 Sketch of the homogeneous particle/air flow apparatus.

as unbiased time averages. Assessment of flow properties with the LV showed that they were uniform within the central portion of the test chamber (± 120 mm in the cross-stream direction and ± 180 mm in the streamwise direction).

4.3 Theoretical Methods

The simplified analysis of Parthasarathy and Faeth (1990a) was used to help exploit the new findings for sphere wakes in turbulent environments, discussed in Section 3, in order to help interpret the measurements of the properties of particle-generated turbulence. The major assumptions of the analysis are as follows: the flows are statistically stationary with uniform particle fluxes and constant continuous-phase properties; particle arrival times are independent of other particle arrival times so that they satisfy Poisson statistics; the flows are infinite in extent, the flows are dilute so that the probability of a test point being within a particle is small; the contribution of flow properties immediately around particles is ignored for the same reason; and flow properties are taken to be the result of a linear superposition of particle flow fields (wakes) that have reached a particular position.

Summing flow properties under these assumptions involved an extension of methods used to analyze random noise (Rice 1954). Taking the point of observation to be the origin of a cylindrical coordinate system and taking the effect of a particle to have mean and turbulent contributions of $g(r,\phi,t)$ and $g'(r,\phi,t)$, the resulting mean-squared fluctuation about the average (which is zero for present flows) becomes (Parthasarathy and Faeth 1990a):

$$\overline{G'^2} = \dot{n}'' \int_{-\infty}^{\infty} dt \int_{0}^{2\pi} d\phi \int_{0}^{\infty} [g^2(r,\phi,t) + g'^2(r,\phi,t)]r\,dr. \tag{7}$$

Equation (7) is for a monodisperse particle or drop flow. Under the assumption of linear superposition, however, if $\overline{G}$ is a generic property for a particular diameter, then the mean value of ϕ becomes:

$$\overline{G} = \int_{0}^{\infty} G(d)PDF(d)dd \tag{8}$$

where PDF(d) is the probability density function of particle diameter. Formulas used for other properties — mean quantities, temporal correlations, temporal spectra, and two-point spatial correlations — can be formed in Parthasarathy and Faeth (1990a).

One of the problems of applying Eqs. (7) and (8) during earlier work was that the integrals did not converge when using the properties of wakes in nonturbulent environments; in particular, turbulent wakes exhibited a power law divergence of velocity fluctuations while allowing for a laminar wake in the final decay period still resulted in a logarithmic divergence of the integrals, see Parthasarathy and Faeth (1990a). Thus, these initial predictions required rather arbitrary termination of integrations at particular streamwise positions which was helpful for fitting measurements and predictions but clearly was very unsatisfactory from the fundamental standpoint. Fortunately, the observation of laminar-like turbulent wakes for wakes in turbulent environments eliminated this problem and yields a closed procedure. This comes about due to the high-order final rate of decay that is observed when the mean velocity defect becomes comparable to the ambient velocity fluctuation levels, see Fig. 7. In particular, velocities decay with increasing streamwise distance according to an algebraic power law having a power greater than unity which insures convergence of Eqs. (7) and (8). Thus, in order to close the stochastic approach, the end of the wake region for laminar-like turbulent wakes was

specified to occur when $\bar{u}_c/\bar{u}'_\infty = 0.3$, which corresponds to the mid-range region of the final fast-decaying wake portion of the flow. Thus, predictions involved an iterative procedure: a value of the turbulence intensity was guessed, integrations for this condition were completed using appropriate laminar-like turbulent wake properties, and this process was repeated until the initial and final values of the turbulence intensity were the same.

4.4 Results and Discussion

Particle-generated turbulence fields are unusual because it is rather simple to find the local rate of dissipation of turbulence kinetic energy, which must be equal to the local loss of particle mechanical energy, e.g.,

$$\varepsilon = \pi\dot{n}''d^2 C_D U^2/8 \tag{9}$$

Then, similar to Mizukami et al. (1992), the predictions for streamwise and cross-stream relative turbulence intensities can be put in the following form:

$$(\overline{u'^2})^{1/2}/U = C_u[\varepsilon d(\theta/d)^2/U^3]^{1/2} \tag{10}$$

and

$$(\overline{v'^2})^{1/2}/U = Cv[\varepsilon d(\theta/d)^2/U^3]^{1/2} \tag{11}$$

where the wake momentum diameter, θ, is defined as:

$$\theta = (C_D d^2/8)^{1/2} \tag{12}$$

The dimensionless parameter on the right-hand sides of Eqs. (10) and (11) plays an important role in turbulence generation and will be called the dissipation factor in the following. The coefficients, C_u and C_v, potentially are functions of the Reynolds numbers of the spheres and the turbulence intensity of the particle-generated flows. Fortunately, the available test conditions of Parthasarathy and Faeth (1990a,b) and Mizukami et al. (1992) involve nearly monodisperse particles; therefore, d, U, Re, and thus C_D and θ, are essentially the same for the entire flow.

Present predictions of $\bar{u}'$ and $\bar{v}'$, along with the measurements for particle/air and particle/water flows due to Parthasarathy and Faeth (1990a,b) and Mizukami et al. (1992), are plotted in Fig. 11 as suggested by Eqs. (10) and (11). Two sets of predictions are shown, either omitting or including the contribution due to turbulence in the wake. Unfortunately, it was not possible to provide predictions for relative turbulence intensities less than 2% because this was the lowest value available from wake property experiments to date, see Fig. 9. The measurements include sphere Reynolds numbers in the range 38-780, due to the variations of sphere sizes and the use of air and water environments; predictions have been completed for the same range of conditions.

When plotted according to the coordinates of Fig. 11, the measurements exhibit little effect of actual sphere Reynolds numbers; therefore, this parameter has not been identified on the figure. The predictions also were relatively independent of Reynolds numbers and single lines have been used to represent these results. Predictions ignoring velocity fluctuations in the laminar-like turbulent wakes are not very satisfactory: measured streamwise velocity fluctuations are underestimated by a factor of roughly two and, more importantly, cross-stream velocity fluctuations are underestimated of a factor of roughly
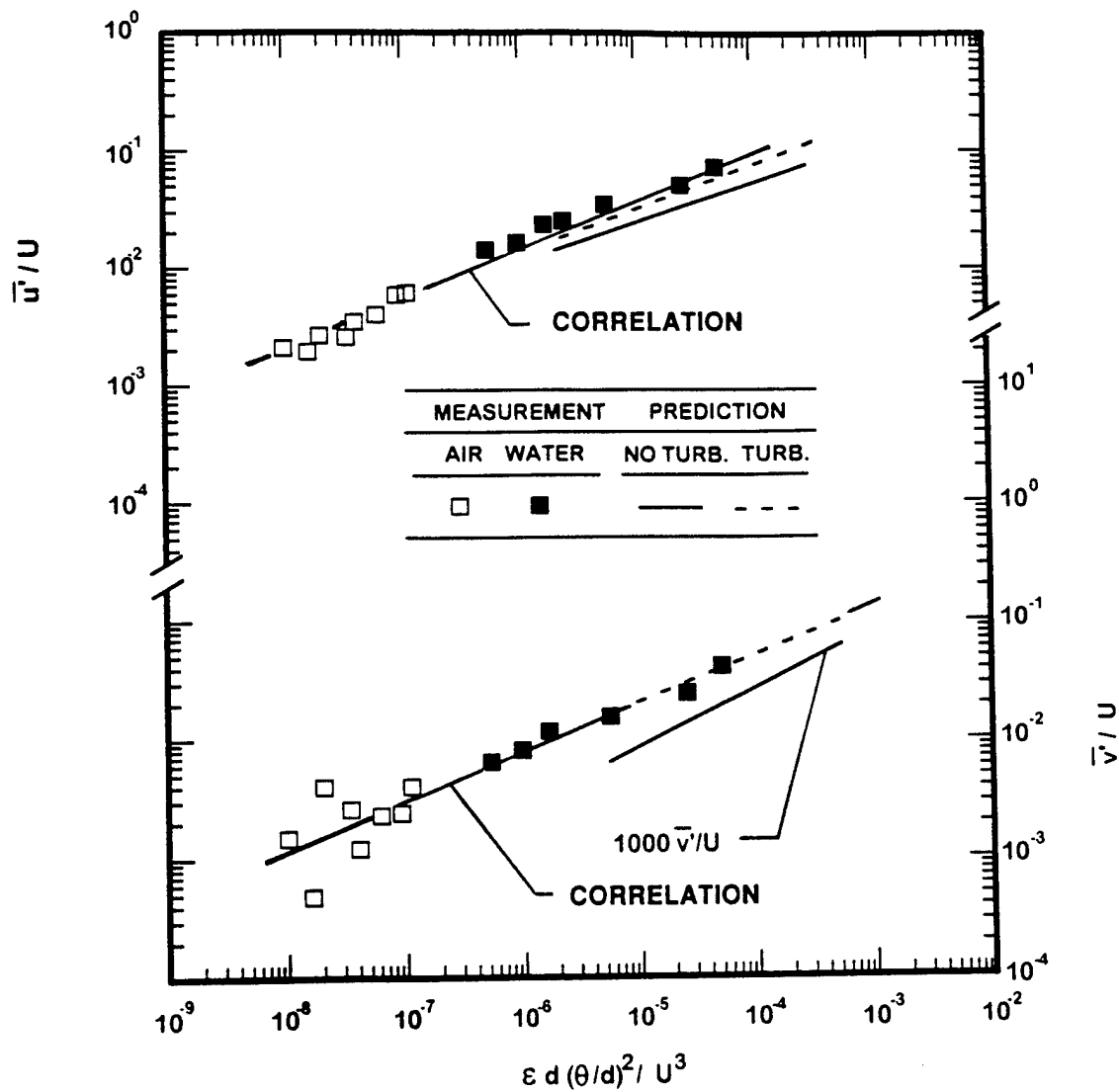
Figure 11 Measured and predicted streamwise and cross-stream rms velocity
fluctuations due to homogeneous particle-generated turbulence.

1000! The large difference between predictions with and without consideration of turbulence for cross-stream velocity fluctuations comes about due to the small values of mean cross-stream velocities in wakes. Including the contribution of wake turbulence, however, yields rather satisfactory predictions of both streamwise and cross-stream velocity fluctuations, which is quite impressive because the theory really has no adjustable parameters (other than a weak effect of the position where integration of wake properties is terminated). Thus, both mean and fluctuating velocities in the laminar-like wakes appear to contribute to turbulence generation, with mean properties contributing due to the randomness of the arrival of particle (drop) wakes at any given point in the flow field. This behavior accounts for the unusually large range of length scales present in particle-generated turbulence fields even though particle Reynolds numbers are small.

The comparison between measurements and predictions is less satisfying when correlations and integral scales are considered. The main difficulty with these properties is that available wake results do not provide information needed to define the turbulent effect in Eq. (7); therefore, only the contribution of mean wake properties can be considered. These results are illustrated for cross-stream and streamwise two-point spatial correlations in Figs. 12 and 13. In these figures, distances in the cross-stream and streamwise directions have been normalized by the corresponding cross-stream or streamwise spatial integral scales based on streamwise velocities, L_{uy} and L_{ux}, respectively. When plotted in this manner, measured correlations are relatively independent of sphere Reynolds number and the ambient turbulence intensity; this behavior also is supported by predictions. In addition, measured and predicted cross-stream correlations also are in reasonably good agreement in Fig. 12. On the other hand, the comparison between measured and predicted streamwise correlations is much less satisfactory in Fig. 13: predictions decay much too rapidly at small values of x/L_{ux} and exhibit a long tail at large values of streamwise distance that are not in good agreement with measurements. As might be expected, predictions of L_{ug} and L_{ux} themselves also are not very good, similar to problems encountered by Parthasarathy and Faeth (1990a,b) and Mizukami et al. (1992), see J.-S. Wu and Faeth (1995b). It seems unlikely that predictions of these properties will be significantly improved until appropriate turbulence properties are known for individual laminar-like turbulent wakes.

Thus, the new results concerning laminar-like turbulent wakes have substantially improved understanding of turbulence generation and capabilities for predicting the properties of turbulence in dispersed multiphase flows. Nevertheless, current problems about predictions of correlations, spectra and scales in these flows point to the need for additional study. In particular, new measurements of turbulence properties in laminar-like turbulent wakes are needed. Another problem is the need for more information about laminar-like turbulent wakes at low relative turbulence intensities so that predictions can be extended to the range of ambient turbulence intensities of greatest practical interest for combusting sprays. Current work seeks to address both these issues.

4.5 Conclusions

Turbulence generation in dispersed multiphase flows was studied theoretically with predictions evaluated using the measurements of Parthasarathy and Faeth (1990a,b) and Mizukami et al. (1992). The major conclusions of the study are as follows:

1.   Relative turbulence intensities were essentially independent of particle Reynolds numbers and could be correlated as functions of the dissipation factor, $\varepsilon d(\theta/d)^2/U^3$,
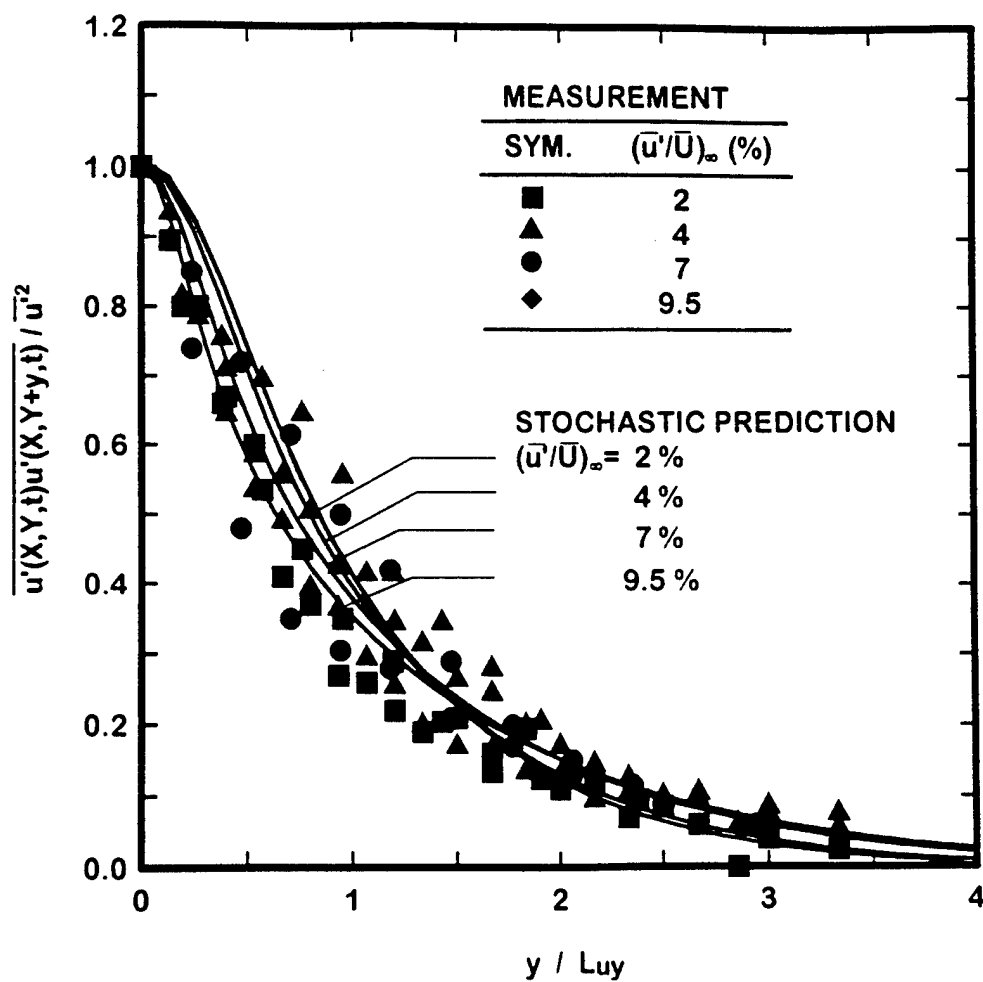
Figure 12 Measured and predicted spatial correlation of streamwise velocity
fluctuations in the cross-stream direction for homogeneous particle-
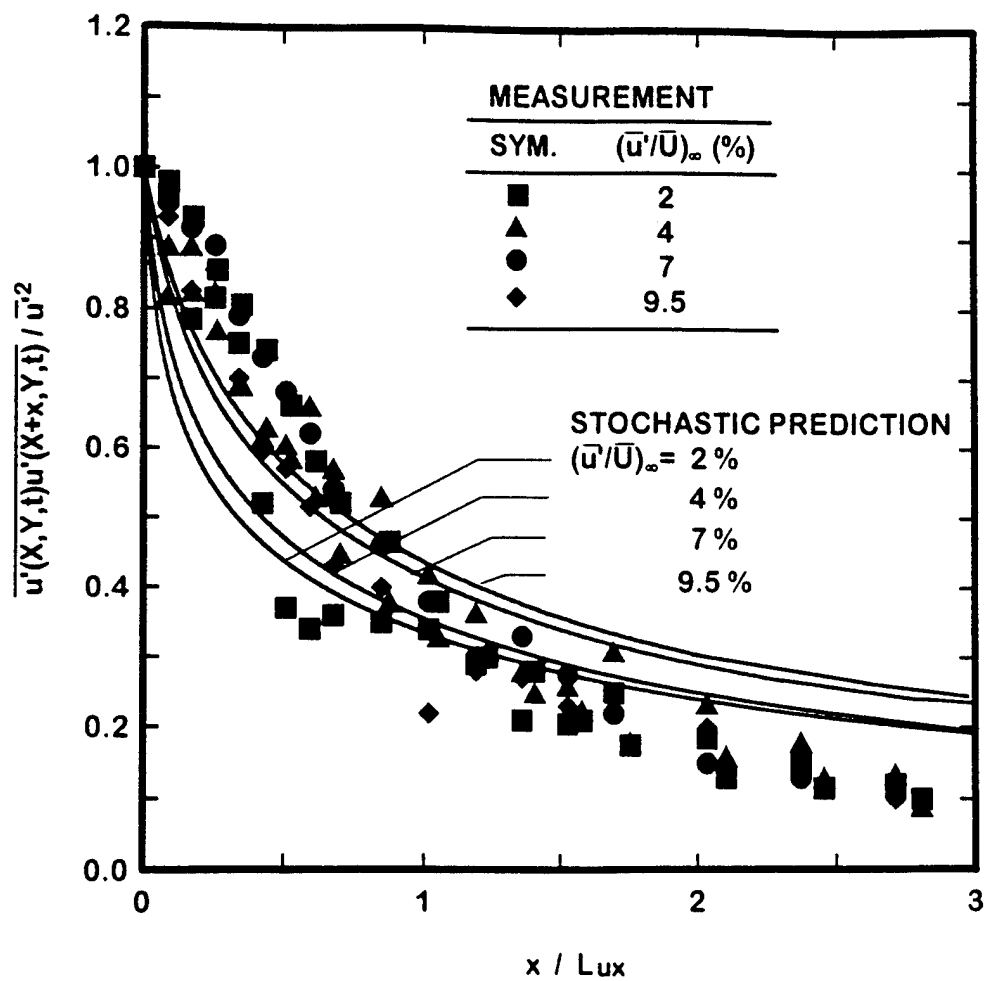generated turbulence.

Figure 13   Measured and predicted spatial correlation of streamwise velocity fluctuations in the streamwise direction for homogeneous particle-generated turbulence.

alone. Relative turbulence intensities from this mechanism can be quite large, approaching 10% for conditions comparable to dense sprays.

2. Recent observations of laminar-like turbulent wakes have resolved earlier problems of closure for stochastic methods of treating turbulence generation using Campbell's Theorem to superimpose results for individual wakes (which extends well-known methods used to study electrical noise to the three-dimensional environment of dispersed multiphase flows). The main effect resolving past stochastic convergence problems was the discovery of the fast-decaying final wake region where mean velocity defects and ambient turbulent fluctuations are comparable.

3. The revised stochastic theory using the properties of laminar-like turbulent wakes was helpful in explaining many features of turbulence generation, including the magnitude and trends of streamwise and cross-stream velocity fluctuations. However, problems till remain concerning correlations, scales and other turbulence properties.

Improved understanding of turbulence generation and the properties of turbulence in dispersed multiphase flows will require new information about the turbulence properties (correlations, spectra, scales, etc.) of laminar-like turbulent wakes, as well as measurements of laminar-like turbulent wake properties at ambient turbulence intensities less than 2%. Current work is addressing both these issues.

REFERENCES

Batchelor, G.K. and Townsend, A.A. (1948) Decay of turbulence in the final period. Proc. Roy. Soc. (London) A194, 527-543.

Chou, W.-H., Hsiang, L.-P. and Faeth, G.M. (1995) Temporal variation of drop properties and formation rates during secondary breakup. AIAA Paper No. 95-2426.

Faeth, G.M. (1987) Mixing, transport and combustion in sprays. Prog. Energy Combust. Sci. 13, 293-345.

Faeth, G.M. (1990) Structure and atomization properties of dense turbulent sprays. Twenty-Third Symposium (International) on Combustion, The Combustion Institute, Pittsburgh, 1345-1352.

Faeth, G.M. (1995) Spray combustion: a review. Proceedings of Second International Conference on Multiphase Flow, (A. Serizawa, T. Fukano and J. Bataille, eds.), Kyoto University, Kyoto, Vol. 1, pp. CO-1 to CO-16.

Faeth, G.M. (1996) Spray combustion phenomena. Twenty-Sixth Symposium (International) on Combustion, The Combustion Institute, Pittsburgh, invited.

Faeth, G.M. Hsiang, L.-P. and Wu, P.-K. (1995) Structure and breakup properties of sprays. Ann. Rev. Multiphase Flow, in press.

Hanson, A.R., Domich, E.G. and Adams, H.S. (1963) Shock-tube investigation of the breakup of drops by air blasts. Phys. Fluids 6, 1070-1080.

Hinze, J.O. (1955) Fundamentals of the hydrodynamic mechanism of splitting in dispersion processes. AIChE J. 1, 289-295.

Hsiang, L.-P. (1994) Near-limit drop deformation and secondary breakup. Ph.D. Thesis, The University of Michigan, Ann Arbor, Michigan.

Hsiang, L.-P. and Faeth. G.M. (1992) Near-limit drop deformation and secondary breakup. Int. J. Multiphase Flow 18, 635-652.

Hsiang, L.-P. and Faeth, G.M. (1993) Drop properties after secondary breakup. Int. J. Multiphase Flow 19, 721-735.

Hsiang, L.-P. and Faeth, G.M. (1995) Drop deformation and breakup due to shock wave and steady disturbances. Int. J. Multiphase Flow 21, 545-560.

Krzeczkowski, S.A. (1980) Measurement of liquid droplet disintegration mechanisms. Int. J. Multiphase Flow 6, 227-239.

Lance, M. and Bataille, J. (1982) Turbulence in the liquid phase of a bubbly air-water flow. Adv. Two-Phase Flow & Heat Trans. 1, Martinus Nijhof, Amsterdam, pp. 403-427.

Lane, W. R. (1951) Shatter of drops in streams of air. Ind. Engr. Chem. 43, 1312-1317.

Loparev, V.P. (1975) Experimental investigation of the atomization of drops of liquid under conditions of a gradual rise of the external forces. Izvestiya Akademii Nauk SSSR, Mekhanika Zhidkosti i Gaza 3, 174-178

Mizukami, M., Parthasarathy, R.N. and Faeth, G.M., (1992) Particle-generated turbulence in homogeneous dilute dispersed flows. Int. J. Multiphase Flow 18, 397-412.

Parthasarathy, R.N. (1989) Homogeneous dilute turbulent particle-laden water flows. Ph.D. Thesis, The University of Michigan, Ann Arbor, Michigan.

Parthasarathy, R.N. and Faeth, G.M. (1987) Structure of particle-laden turbulent water jets in still water. Int. J. Multiphase Flow 13, 699-716.

Parthasarathy, R.N. and Faeth, G.M. (1990) Turbulence modulation in homogeneous dilute particle-laden flows. J. Fluid Mech. 220, 485-514.

Parthasarathy, R.N. and Faeth, G.M. (1990) Turbulent dispersion of particles in self-generated homogeneous turbulence. J. Fluid Mech. 220, 515-537.

Ranger, A.A. and Nicholls, J.A. (1969) The aerodynamic shattering of liquid drops. AIAA J. 7, 285-290.

Rice, S.O. (1954) Mathematical analysis of random noise. *Noise and Stochastic Processes* (N. Wax, ed.), Dover Publications, New York, 133-294.

Ruff, G.A. and Faeth, G.M., (1995) Non-intrusive measurements of the structure of dense sprays, Prog. Astro. Aero., in press.

Ruff, G.A., Sagar, A.D. and Faeth, G.M. (1989) Structure of the near-injector region of pressure-atomized sprays. AIAA J. 27, 901-908.

Ruff, G.A., Bernal, L.P. and Faeth, G.M. (1991) Structure of the near-injector region of non-evaporating pressure-atomized sprays. J. Prop. Power 7, 221-230.

Ruff, G.A., Wu, P.-K., Bernal, L. P. and Faeth, G.M. (1992) Continuous- and dispersed-phase structure of dense non-evaporating pressure-atomized sprays. J. Prop. Power 8, 280-289.

Schlichting, H. (1975) Boundary Layer Theory, 7th ed., McGraw-Hill, New York, 234-235, 599.

Simmons, H.C. (1977) The correlation of drop-size distributions in fuel nozzle sprays. J. Engr. for Power 99, 309-319.

Tennekes, H. and Lumley, J.L. (1972) A First Course in Turbulence, MIT Press, Cambridge, Massachusetts, 275-284.

Wu, J.-S. (1994) The structure of sphere wakes at intermediate Reynolds numbers in still and turbulent environments. Ph.D. Thesis, The University of Michigan, Ann Arbor, Michigan.

Wu, J.-S. and Faeth, G.M. (1993) Sphere wakes in still surroundings at intermediate Reynolds numbers. AIAA J. 31, 1448-1455.

Wu, J.-S. and Faeth, G.M. (1994) Sphere wakes at moderate Reynolds numbers in a turbulent environment. AIAA J. 32, 535-541.

Wu, J.-S. and Faeth, G.M. (1995a) Effects of ambient turbulence intensity on sphere wakes at intermediate Reynolds numbers. AIAA J. 33, 171-173.

Wu, J.-S. and Faeth, G.M. (1995b) Predictions of turbulence generation by particles in honogeneous dilute dispersed flows. AIAA J., submitted.

Wu, P.-K. and Faeth, G.M. (1993) Aerodynamic effects in primary breakup of turbulent liquids. Atomization and Sprays 3, 265-289.

Appendix A: Hsiang, L.-P. and Faeth, G.M. (1993) Drop properties after secondary breakup. <u>Int. J. Multiphase Flow</u> 19, 721-735.

DROP PROPERTIES AFTER SECONDARY BREAKUP

L.-P. HSIANG and G. M. FAETH†

Department of Aerospace Engineering, The University of Michigan, Ann Arbor, MI 48109-2140, U.S.A.

Abstract—Drop properties during and after secondary breakup in the bag, multimode and shear breakup regimes were observed for shock-wave-initiated disturbances in air at normal temperature and pressure. Test liquids included water, *n*-heptane, ethyl alcohol and glycerol mixtures to yield Weber numbers of 15–600, Ohnesorge numbers of 0.0025–0.039, liquid/gas density ratios of 579–985 and Reynolds numbers of 1060–15080. Measurements included pulsed shadowgraphy and double-pulsed holography to find drop sizes and velocities after breakup. Drop size distributions after breakup satisfied Simmons' universal root normal distribution in all three breakup regimes, after removing the core (or drop-forming) drop from the drop population for shear breakup. The size and velocity of the core drop after shear breakup was correlated separately based on the observation that the end of drop stripping corresponded to a constant Eötvös number. The relative velocities of the drop liquid were significantly reduced during secondary breakup, due both to the large drag coefficients caused by drop deformation and the reduced relaxation times of smaller drops. These effects were correlated successfully based on a simplified phenomenological theory.

Key Words: drop breakup, drop dynamics, drop deformation, pulsed holography

1. INTRODUCTION

Numerous studies of secondary drop breakup have been reported due to applications for liquid atomization, industrial and agricultural sprays, dispersed multiphase flows and rainfall, among others. In particular, recent studies suggest that secondary breakup is a rate-controlling process in the near-injector region of pressure-atomized sprays through its affect on drop sizes (Ruff *et al.* 1992). Furthermore, primary breakup at the surface of both nonturbulent and turbulent liquids yields drops that intrinsically are unstable to secondary breakup (Wu & Faeth 1992; Wu *et al.* 1991, 1992). Prompted by these observations, the objective of the present investigation was to extend recent work on secondary breakup caused by well-defined step changes of relative velocities (shock-wave disturbances) in this laboratory (Hsiang & Faeth 1992).

The following discussion of past research on secondary breakup is brief, see Hsiang & Faeth (1992), Wierzba & Takayama (1987), Giffen & Muraszew (1953), Hinze (1955), Krzeczkowski (1980), and references cited therein, for more complete reviews. High-speed photography has been used to identify secondary breakup regimes for shock-wave disturbances (Hinze 1955; Hanson *et al.* 1963; Reinecke & McKay 1969; Reinecke & Waldman 1970; Ranger & Nicholls 1969; Gel'fand *et al.* 1974; Krzeczkowski 1980; Wierzba & Takayama 1988). Bag breakup is observed at the onset of secondary breakup. This process involves deflection of the center of the drop into a thin bag, followed by breakup of both the bag and the liquid ring at its base into drops. Shear breakup is observed at higher relative velocities. This process involves stripping of drops from the periphery of the original drop. Finally, the transition between the bag and shear breakup regimes involves a complex combination of behavior at these two limits. This regime will be termed multimode breakup, following Hsiang & Faeth (1992), but it also has been called parachute breakup, chaotic breakup, bag-jet breakup and transition breakup (Krzeczkowski 1980; Wierzba & Takayama 1988). Measurements of transitions between breakup regimes have been limited to liquid/gas density ratios, $\rho_L/\rho_G > 500$ and Reynolds numbers, $Re = \rho_G d_0 u_0/\mu_G > 500$, where d_0 and u_0 denote the original drop diameter and relative velocity and μ_G is the gas viscosity (Hinze 1955; Krzeczkowski 1980; Hsiang & Faeth 1992). Hinze (1955) shows that breakup regime transitions largely are functions of the ratio of drag/surface tension forces, represented by the Weber number,

---

†To whom all correspondence should be addressed.

We $= \rho_G d_0 u_0^2 / \sigma$, and the ratio of liquid viscous surface tension forces, represented by the Ohnesorge number Oh $= \mu_L / (\rho_L d_0 \sigma)^{1/2}$, where $\sigma =$ surface tension and $\mu_L =$ liquid viscosity. Hinze (1955) found that the progressively larger We were required for the onset of breakup as Oh increases because viscous forces inhibit drop deformation which is the first step in the breakup process. This behavior has been confirmed by later investigations (Krzeczkowski 1980; Hsiang & Faeth 1992).

The time required for breakup is another aspect of secondary breakup that has received significant attention for shock-wave disturbances at $\rho_L / \rho_G > 500$. For low Oh, it has been found that breakup times normalized by the characteristic breakup time of Ranger & Nicholls (1969), which will be defined later, are remarkably independent of the breakup regime and We (Liang *et al.* 1988). As might be expected from the effect of Oh on breakup regimes, however, recent work shows that normalized breakup times tend to increase with increasing Oh (Hsiang & Faeth 1992). Processes of drop deformation and the variation of the drop drag coefficient with time also appear to scale systematically in terms of the characteristic breakup time (Hsiang & Faeth 1992).

In comparison to other breakup properties, available information about the outcome of secondary breakup is rather limited. Nevertheless, measurements of drop size distributions for shock-wave disturbances at $\rho_L / \rho_G > 500$ have been reported by Gel'fand *et al.* (1974) and Hsiang & Faeth (1992). Gel'fand *et al.* (1974) observed a bimodal drop size distribution for bag breakup, and suggested that the small drops largely resulted from breakup of the bag and the large drops from breakup of the liquid ring at the base of the bag. However, the later measurements of Hsiang & Faeth (1992) did not confirm this finding. Instead, drop size distributions satisfied the universal root normal distribution with the ratio of the mass median diameter to the Sauter mean diameter, MMD/SMD $= 1.2$, proposed by Simmons (1977). This distribution also has been effective for drops within dense sprays and after primary breakup (Ruff *et al.* 1992; Wu & Faeth 1992; Wu *et al.* 1991, 1992). An exception to this behavior was shear breakup, where the universal root normal distribution was somewhat distorted at large drop sizes. The universal root normal distribution only involves two parameters; therefore, after fixing MMD/SMD, drop sizes are fully specified by the SMD alone. It was found that the SMD for all breakup regimes could be correlated successfully based on a phenomenological analysis of shear breakup (Hsiang & Faeth 1992). These results, however, raised questions about the mechanism causing secondary breakup to end. In particular, at large values of We, large drops in the size distribution after secondary breakup did not undergo subsequent breakup, even though they were unstable to secondary breakup based on existing breakup criteria—barring unusually large reductions of their relative velocities during the secondary breakup process. Unfortunately, information about drop velocities after secondary breakup was not available, so that the mechanism causing breakup to end was not resolved. In addition, information about drop size and velocity correlations after secondary breakup clearly is needed for rational estimates of secondary breakup properties in dispersed flows.

The objective of the present investigation was to extend the work of Hsiang & Faeth (1992) in order to resolve the problems of drop size distributions after shear breakup, the mechanism causing breakup to end, and drop size/velocity correlations after secondary breakup. Experimental methods involved shock-wave-induced disturbances in air with shadowgraph motion picture photography and pulsed holography used to observe the breakup process. The study was limited to conditions representative of bag, multimode and shear breakup near atmospheric pressure: $\rho_L / \rho_G > 500$, Oh < 0.039 and Re > 100. Water, *n*-heptane, ethyl alcohol and various glycerol mixtures were used as test liquids in order to resolve effects of liquid properties. Phenomenological descriptions of various aspects of secondary breakup were used to help interpret and correlate the measurements.

The paper begins with a discussion of experimental methods. Results are then considered, treating drop size distributions, the properties of the core (or drop-forming) drop when shear breakup ends, and drop velocities after secondary breakup in all three breakup regimes, in turn.

2. EXPERIMENTAL METHODS

2.1. Apparatus

The test apparatus was the same as that of Hsiang & Faeth (1992) and only will be described briefly. A shock tube with the driven section open to the atmosphere, similar to Ranger & Nicholls

(1969), was used for the experiments. The driven section had a rectangular cross section (38 mm wide × 64 mm high) and a length of 6.7 m with the test location 4.0 m from the downstream end. This provided test times of 17–21 ms in the uniform flow region behind the incident shock wave.

The test location had quartz windows (25 mm high × 305 mm long, mounted flush with the interior of the side walls) to allow observations of drop breakup. A drop generator using a vibrating capillary tube, similar to Dabora (1967), was used to generate a stream of drops. This drop stream passed through 6 mm dia holes in the top and bottom of the driven section, crossing the central plane of the driven section at the test location. An electrostatic drop selection system, similar to Sangiovanni & Kestin (1977), was used to deflect a fraction of the drops out of the stream. This yielded a drop spacing of roughly 7 mm so that drops always were present in the region observed while interactions between drops during secondary breakup were eliminated.

2.2. Instrumentation

Breakup properties were recorded using pulsed shadowgraph motion pictures and double-pulsed holography. Pulsed shadowgraph motion pictures were used to observe the overall dynamics of breakup, e.g. drop velocities prior to the onset of breakup and the properties of the core drop, using an arrangement similar to Hsiang & Faeth (1992). This involved a copper vapor laser as the light source with a 35 mm drum camera used to record shadowgraph images at unity magnification. A function generator was used to pulse the laser when the shock wave neared the drop stream location, with pulse frequencies of 6–8 kHz for 20 pulses. Each laser pulse duration was 30 ns which was sufficient to stop the motion of the drop on the rotating film drum. The drum camera recorded the images with an open shutter within a darkened room. The time between shadowgraph pictures was monitored by recording signal generator output using a digital oscilloscope. The film records were analyzed using a Gould FD 5000 image display. The procedure was to obtain three motion picture shadowgraphs for a particular test condition and group the data to obtain statistically-significant results as ensemble averages. Experimental uncertainties (95% confidence) of the measurements reported here are as follows: initial drop diameter and diameter of the core drop at the end of shear breakup, < 10%; and velocity and position of the core drop at the end of shear breakup, < 15%.

Double-pulsed holography was used to measure drop size and velocity correlations after secondary breakup. The holocamera and reconstruction systems were similar to those of Hsiang & Faeth (1992). An off-axis arrangement was used with optics providing a 2–3 : 1 magnification of the hologram image, and laser pulse time of 20 ns which was sufficient to stop the motion of the drops on film. This was coupled with reconstruction optics that allowed drop diameters as small as 25 μm to be measured with 5% accuracy and drops as small as 10–15 μm to be observed. Reconstruction of the double-pulse holograms yielded two images of the spray with separation times as short as 1 μs. The second pulse was somewhat weaker than the first pulse which allowed directional ambiguity to be resolved because the stronger pulse yielded a sharper reconstructed image. The properties of the reconstructed images were observed using the Gould FD 5000 Image Display with a field view of 1.7 × 2.0 mm. Various locations in the hologram reconstruction were observed by traversing the hologram in two directions and the videocamera of the image display in the third direction.

Drops were sized in the same manner as by Hsiang & Faeth (1992). The diameters of mildly irregular objects were found by measuring their maximum and minimum diameters, d_{max} and d_{min}, through the centroid of the image. Then assuming that the drop had an ellipsoidal shape, the drop diameter was taken to be the diameter, d, of a sphere having the same volume, $d^3 = d_{min}^2 d_{max}$, as the ellipsoid. More irregular images were sized by finding the cross-sectional area and perimeter of the image and proceeding as before for an ellipsoid having the same properties. The velocity of each drop was found by measuring the distance between the centroid of its two images and dividing by the known time between laser pulses. Results at each condition were summed over at least three realizations, considering 150–300 liquid elements, in order to provide drop size and velocity correlations. Experimental uncertainties caused by the definition of drop diameters are difficult to quantify, however, they are felt to be small in comparison to the accuracy of the size and distance measurements, sampling limitations and effects of grouping of data when velocities were found for a particular drop size. Estimated experimental uncertainties (95% confidence) based on the latter effects are < 10% for drop diameters and < 15% for drop velocities.

2.3. Test Conditions

The test conditions are summarized in table 1. Test drops of water, n-heptane, ethyl alcohol and various glycerol mixtures were used to provide a wide range of liquid properties. The liquid properties listed in table 1 were obtained from Lange (1952), except for the surface tension of the glycerol mixtures which was measured in the same manner as Wu et al. (1991). Initial drop diameters were 1000 μm with the following ranges of other variables: $\rho_L/\rho_G = 580$ to 985, Oh = 0.0025 to 0.039, We = 15 to 600 and Re = 1060 to 15080. The We range includes the bag, multimode and shear breakup regimes, which begin at We = 13, 35 and 80 respectively, based on the measurements of Hsiang & Faeth (1992). The Re range of the present experiments is higher than conditions where gas viscosity plays a significant role on drop drag properties, e.g. the drag coefficient, C_D, for spheres only varies in the range 0.4–0.5 (White 1974). Shock Mach numbers were relatively low, 1.08–1.31, so that physical properties within the uniform flow region were not significantly different from room air.

3. RESULTS

3.1. Drop Size Distributions

It was necessary to address drop size distributions after secondary breakup first because this affects the information needed to characterize secondary breakup properties and drop size and velocity correlations. The main issue to be examined was the distortion of the universal root normal size distribution at large drop sizes after shear breakup, observed by Hsiang & Faeth (1992).

The difficulty with the size distribution function for shear breakup appeared to be due to the presence of the core (or drop-forming) drop, which is the remaining portion of the original drop after the stripping of smaller drops has ended. In particular, the core drop is one of the largest drops in the distribution which corresponded to the region where the measured drop dize distribution departed from the universal root normal distribution. Thus, it seemed plausible that the size distribution would approximate the root normal distribution if the core drop was removed from the drop population.

The resulting drop size distributions after shear breakup, with the core drop removed from the drop population, are illustrated in figure 1. These measurements were obtained directly from the data of Hsiang & Faeth (1992). The results are plotted in terms of the root normal distribution function, with the function itself illustrated for values of MMD/SMD = 1.0, 1.20 and 1.50. The measurements are somewhat scattered at large drop sizes because the number of large drops is limited from the breakup of single drops. In view of this effect, the measured drop size distributions are represented reasonably well by the root normal distribution function with MMD/SMD = 1.2. This behavior is similar to drop size distributions after primary breakup and within dense sprays, as well as for secondary breakup in the bag and multimode breakup regimes (Hsiang & Faeth 1992). Thus, the complication of distortion of the drop size distribution for shear breakup can be handled by treating the core drop separately from the population of the drops stripped from the original drop.

As noted earlier, the universal root normal drop size distribution is specified completely if the SMD is known because the only other parameter in the distribution is fixed, e.g. MMD/SMD = 1.2.

Table 1. Summary of test conditions[a]

Drop liquid	ρ_L (kg/m³)	$\mu_L \times 10^4$ (kg/ms)	$\sigma \times 10^3$ (N·m)	Oh	We	Re
Water	997	8.94	70.8	0.0038	15–600	1990–15080
n-Heptane	683	3.94	20.0	0.0025	15–600	1060–7200
Ethyl alcohol	800	16.0	24.0	0.011	15–600	1150–7880
Glycerol (42%)[b]	1105	35.0	65.4	0.012	15–375	1910–10790
Glycerol (63%)[b]	1162	108.0	64.8	0.039	15–37	1880–10640

[a]Breakup in air initially at 98.8 kPa and 297 ± 2 K in the driven section of the shock tube with shock Mach numbers in the range 1.08–1.31. Properties of air taken at normal temperature and pressure: $\rho_G = 1.18$ kg/m³, $\mu_G = 18.5 \times 10^{-6}$ kg/ms.
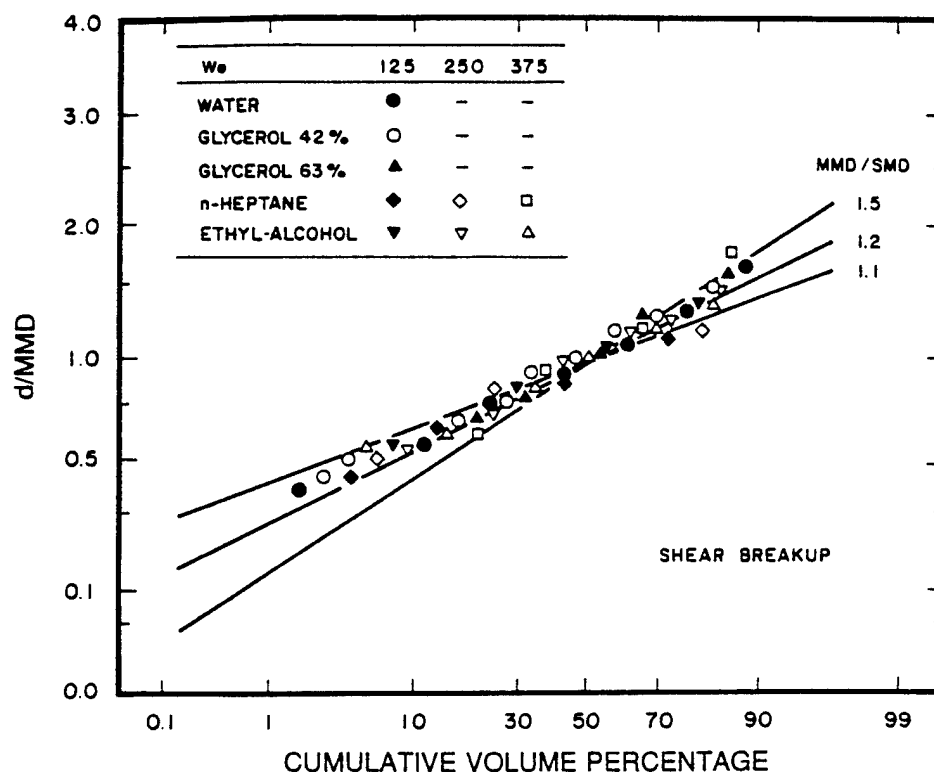
[b]Percentage glycerin by mass.

Figure 1. Drop diameter distribution after shear breakup, excluding the core drop.

In principle, the SMD can be found from the correlation given by Hsiang & Faeth (1992) which was obtained using results in the bag, multimode and shear breakup regimes. Fortunately, removing the core drop from the drop population when finding the SMD for shear breakup has a negligible effect on this correlation for available test conditions, in comparison to experimental uncertainties. Thus, use of the correlation of Hsiang & Faeth (1992) for all three breakup regimes is recommended as before, with the properties of the core drop after shear breakup then added to the distribution.

3.2. Core Drop Velocity

The velocity and size of the core drop at the end of breakup must be known, in order to treat it separately from the rest of the drop population after shear breakup. Since drops stripped from the core drop were not observed to undergo subsequent breakup, the end of shear breakup coincides with the end of drop stripping from the core drop. In the following, the velocity of the core drop at the end of breakup will be considered first. Then given information about core drop velocities, subsequent stability considerations yield its size.

In order to assist data correlation, a simplified analysis was used to estimate core drop velocities at the end of breakup. The major assumptions of the analysis are as follows: virtual mass, Bassett history and gravitational forces were ignored; gas velocities were assumed to be constant; mass stripping from the core drop was ignored; and a constant average drag coefficient was used over the period of breakup. For present conditions, virtual mass and Bassett history forces are small due to the large liquid/gas density ratio of the flow (Faeth 1987). Similarly, gravitational forces are not a factor. e.g. drop motion was nearly horizontal and drag forces were much larger than gravitational forces. Uniform gas properties, were a condition of the present experiments. However, the constant core drop mass assumption, taken to be the original drop mass, is questionable. For example, core drop diameters only were 12–30% of the original drop diameter for present test conditions so that the bulk of the original drop mass was lost during stripping. Nevertheless, selecting some other average drop size over the period of breakup only introduces factors on the

order of unity so that the original size of the drop was chosen for convenience. Similarly, drop drag coefficients. C_D, based on the original drop size vary considerably over the drop breakup period. For example, in the deformation period prior to breakup, C_D varies from values 0.4–0.5 at the start of breakup to 4.8–6.4 when the maximum deformation conditions is reached, over the present test range (Hsiang & Faeth 1992). Subsequently, values of C_D based on d_0 become even larger due to the increased responsiveness of the core drop as it becomes smaller. Nevertheless, the scaling of C_D was such that an effective average value could be found to correlate core drop velocities in spite of the crudeness of the approximations of the analysis.

Based on the previous assumptions, conservation of momentum yields the following equation for the motion of the core drop:

$$du/dt = -3\bar{C}_D\rho_G u^2/(4\rho_L d_0),$$ [1]

where u is the relative velocity at time t after the arrival of the shock wave disturbance and $\bar{C}_D$ is an approximate average drag coefficient over the time of breakup. Integrating [1] yields the relative velocity of the core drop during the breakup period, as follows:

$$u = u_0/[1 + (3\bar{C}_D t/4t^*)(\rho_G/\rho_L)^{1.2}],$$ [2]

where t^* is the characteristic breakup time of Ranger & Nicholls (1969), e.g. $t^* = d_0(\rho_L/\rho_G)^{1.2}/u_0$. Then substituting the breakup time, t_b, into [2], and rearranging, yields the following expression for the absolute velocity of the core drop at the end of breakup, $u_b' = u_0 - u_b$, where u_b is the relative velocity at the end of breakup, as follows:

$$(u_b'/u_0)(\rho_L/\rho_G)^{1.2}(1 + 3C) = 3\bar{C}_D(t_b/t^*)/4,$$ [3]

where

$$C = (3\bar{C}_D t_b/4t^*)(\rho_G/\rho_L)^{1.2}.$$ [4]

Earlier work has shown that $t_b/t^* = 5$ for $10 < We < 10^6$ and $Oh < 0.1$ (Liang et al. 1988; Hsiang & Faeth 1992). Thus, the right-hand side of [3] should be a constant if a constant average value of C_D for the shear breakup process can be found. A reasonable correlation of the present measurements of u_b'/u_0 was obtained by taking $\bar{C}_D = 5$, which is comparable to values observed near the maximum deformation condition (Hsiang & Faeth 1992). This yields $3\bar{C}_D(t_b/t^*)/4 = 19$ on the right-hand side of [3].

The measurements of core drop velocities at the end of breakup, normalized as suggested by [3], are plotted as a function of We in figure 2. Measurements are shown for all the drop liquids over the test range of the shear breakup regime, $100 < We < 600$, along with the fitted prediction of [3]. The correlation for u_b'/u_0 is relatively independent of We over this range as anticipated from [3]. The measurements also are in fair agreement with [3], based on the estimates of t_b/t^* and $\bar{C}_D$ discussed earlier.

The velocity measurements indicated that the relative velocity of the core drop at the end of breakup only was 30–40% lower than the initial relative velocity. This implied that the local We of the core drop when breakup ended generally were greater than the critical Weber number (We_{cr}) for the onset of drop breakup due to shock-wave disturbances ($We = 13$). Thus, the criterion for the end of drop stripping from the core drop differs from the criterion for the onset of breakup. A discussion of this behavior, which leads to an estimation of the core drop diameter, will be considered next.

3.3. Core Drop Size

The dynamic state of a drop at the start of secondary breakup, where the drop is round and the drop liquid is motionless, clearly differs from the state of the core drop when shear breakup ends, where the drop is deformed and liquid motion associated with drop stripping is present. Thus, it is not surprising that local We of the core drop at the end of shear breakup, We_{cr}, are different from (and generally exceed) the We_{cr} associated with the onset of secondary breakup. Instead, conditions defining the end of drop stripping for shear breakup appear to be related more closely to the onset of breakup for more gradual drop motions, such as the breakup of freely-falling drops.
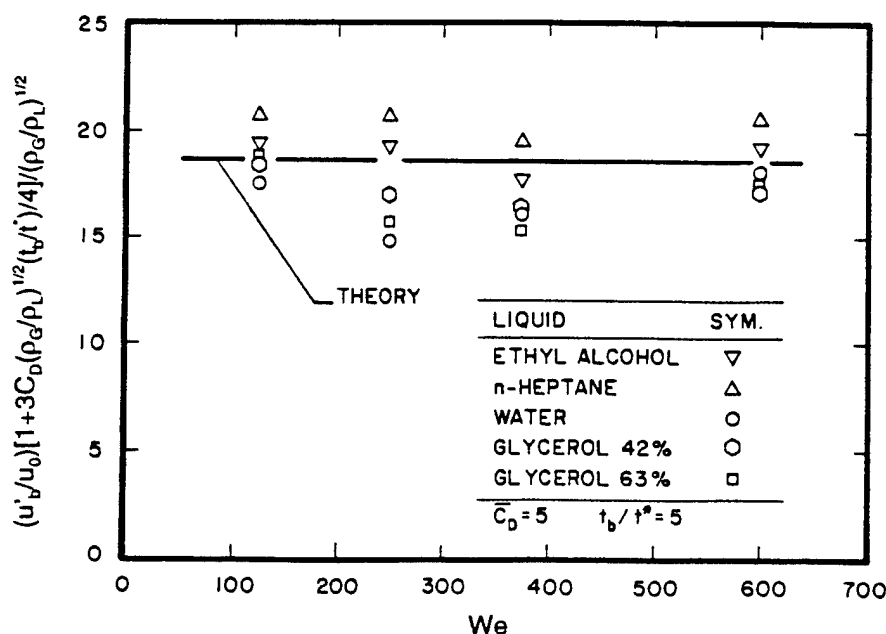
Figure 2. Velocities of the core drop at the end of shear breakup.

This correspondence is exploited in the following to find a criterion for the end of core drop stripping and a method for estimating the size of the core drop at this condition.

The deformation and size of freely-falling drops generally are correlated in terms of the Eötvös number, Eo. The appropriate expression when the drop acceleration, a, is due to gas motion relative to the drop is as follows (Clift *et al.* 1978):

$$Eo = a|\rho_L - \rho_G|d^2/\sigma \approx a\rho_L d^2/\sigma,$$ [5]

where the latter approximation follows because $\rho_L/\rho_G \gg 1$ for present test conditions. It is anticipated that drop stripping ends when a critical value of Eötvös number, Eo_{cr}, is reached, based on the behavior of freely-falling drops. The acceleration of the core drop can be found by differentiating [2] with respect to time, because this expression provided reasonably good estimates of core drop velocities at the end of breakup (cf. figure 2). This yields

$$a = (3\bar{C}_D u_0/4t^*)(\rho_G/\rho_L)^{1/2}(1 + Ct/t_b)^2.$$ [6]

Then evaluating [6] at $t = t_b$, substituting this value of the acceleration into [5], and noting that $d = d_b$ at t_b, yields the following expression for the Eo_{cr} at the end of shear breakup:

$$Eo_{cr} = (3\bar{C}_D We/4)(d_b/d_0)^2/(1 + C)^2.$$ [7]

The values of Eo_{cr} were found for all shear breakup conditions, using $t_b/t^* = 5$ and $\bar{C}_D = 5$ as before. The resulting values of Eo_{cr} for ethyl alcohol, n-heptane and water drops are plotted as a function of We in figure 3. Results for the glycerol mixtures are not included in the plot because an effect of Oh_{cr} was observed, tending to increase Eo_{cr}, that is currently being studied for a wider variation of liquid viscosities. Similar to u_b/u_0 in figure 2, the Eo_{cr} of the core drop at the end of shear breakup is relatively independent of We and liquid type over the range of the measurements, yielding a mean value, $Eo_{cr} = 16$. This behavior also is similar to the breakup requirements of freely-falling drops, as discussed later.

Given Eo_{cr} and the initial conditions of breakup, [7] can be solved to find the diameter of the core drop at the end of shear breakup, d_b. It also is of interest to examine the Weber number of the core drop at this condition, We_{cr}. This can be done by finding u_b and d_b from [3] and [6] and
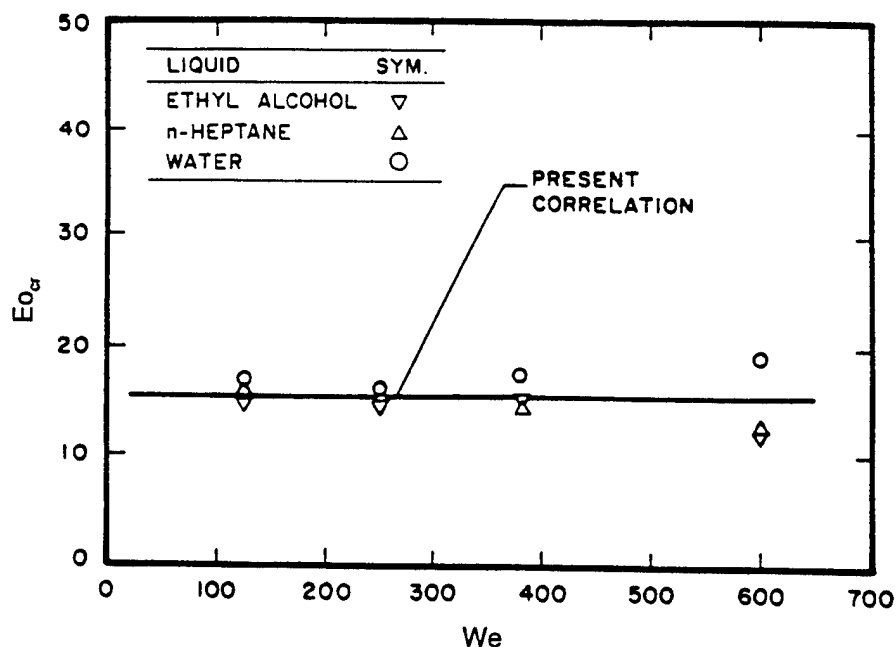
Figure 3. Eo_{cr} of the core drop at the end of shear breakup.

substituting into the normal definition of We, noting that the relative velocity of the core drop is $u_0 - u_b'$, to yield:

$$We_{cr} = (4Eo_{cr}We/3\bar{C}_D)^{1/2}/(1 + C).$$ [8]

Adopting $Eo_{cr} = 16$ and $\bar{C}_D = 5$ as discussed earlier, the coefficient in [8], $(4Eo_{cr}/3\bar{C}_D)^{1/2} = 2.3$.

The present measurements of We_{cr} for shear breakup are plotted as suggested by [8] in figure 4. Similar to figure 3, these results are limited to ethyl alcohol, n-heptane and water drops, pending resolution of the large Oh_{cr} effects observed for the glycerol mixtures. The range of the

Figure 4. We_{cr} of the core drop at the end of shear breakup.

Table 2. Eo_{cr} for gradual termination and initiation of drop breakup

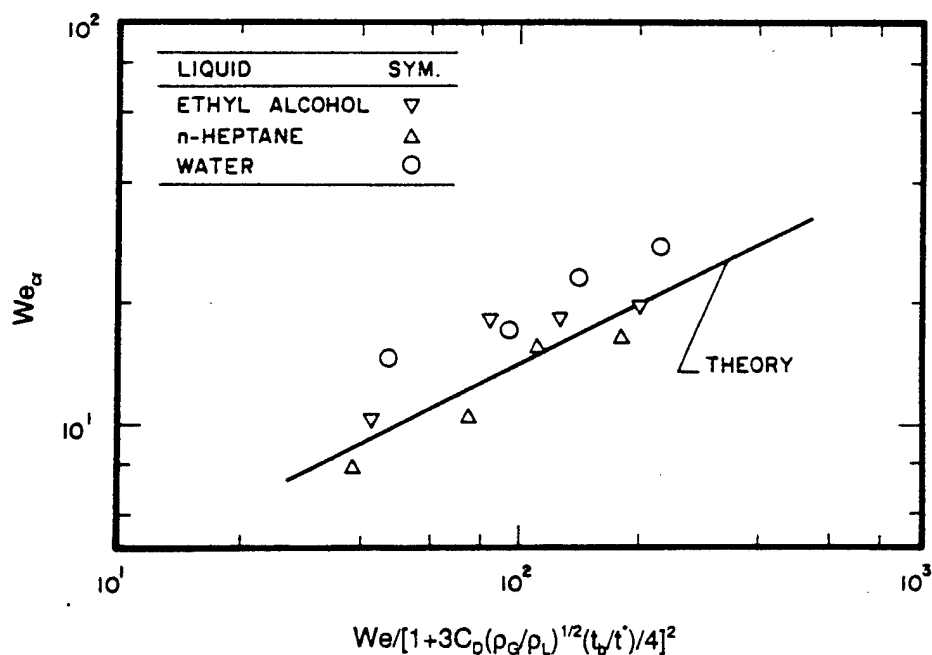| Drop liquid	d (mm)	ρ_L (kg/m³)	$\mu_L \times 10^4$ (kg/ms)	$\sigma \times 10^3$ (N/m)	Oh_{cr}	We_{cr}	Eo_{cr}
(a) End of shear breakup							
In air, present study:							
Water	0.15–0.30	997	8.9	71	0.007–0.010	15.1–28.5	17.5
n-Heptane	0.12–0.26	694	4.0	20	0.007–0.010	7.8–16.0	14.9
Ethyl alcohol	0.13–0.29	800	16.0	24	0.021–0.032	10.5–19.0	14.4
(b) Initiation of bag breakup of freely-falling drops							
In air, Merrington & Richardson (1947):							
Water	10.0	1000	9.8	72	0.0012	—	13.5
Carbon tetachloride	3.6	1577	7.8	41	0.0018	—	8.0
In air, Finlay (1957):							
Water	8.0	1000	9.8	72	0.0013	11.0	8.5
Tetrabromomethane	3.5	2950	92.9	36	0.0150	12.0	7.2
In air, Ryan (1976):							
Water	9.1	1000	9.8	72	—	12.2	11.2
Water + surfactant	7.5	1000	—	50	—	12.4	11.1
Water + surfactant	6.9	1000	—	40	—	—	11.6
Water + surfactant	6.1	1000	—	33	—	14.5	12.2
Water + surfactant	5.2	1000	—	25	—	—	10.6
Water + surfactant	4.7	1000	—	20	—	—	10.9
Water + surfactant	4.4	1000	—	17	—	12.0	11.0
In water, Hu & Kintner (1955):							
Tetrabromomethane	5.1	2950	92.9	36	0.0126	7.4	13.8
Dibromoethane	6.7	2150	15.8	32	0.0023	8.2	16.0
Ethyl bromide	9.1	1448	4.9	30	0.0008	7.0	12.3
Nitrobenzene	15.4	1195	17.4	24	0.0026	8.6	19.1
Bromobenzene	11.3	1488	10.7	38	0.0013	7.8	13.5
Tetrachloroethylene	10.4	1614	9.0	44	0.0010	8.2	14.8
Carbon tetrachloride	10.4	1577	7.8	41	0.0009	7.9	15.1

measurements is $100 < We < 1000$. Finally, [8] is illustrated on the plot, using the fitted values of Eo_{cr}, $\bar{C}_D$ and t_b/t^* discussed earlier. The scatter of the data is relatively large because products of the measurements are involved, e.g. $We_{cr} = \rho_G d_b (u_0 - u_b)^2/\sigma$. Nevertheless, [8] provides a reasonable fit of the measurements. The results show that the end of drop stripping from the core drop involves a range of We, generally greater than $We_{cr} = 13$, which is the critical condition for the onset of secondary breakup from shock-wave disturbances. This comes about in the formulation because $We_{cr} \sim We^{1/2}$ in [8] so that We_{cr} reaches large values as We increases in the shear breakup regime. Nevertheless, drop stripping still ends at these high values of We_{cr} because the rate of acceleration of the drop is below critical levels for the gradual variation of drop disturbance levels near the end of the shear breakup process.

It is of interest to compare present values of Eo_{cr} at the end of drop stripping from the core drop during shear breakup with values observed for the breakup of freely-falling drops, which also represents a gradual variation of drop disturbance levels. Thus, table 2 is a summary of Eo_{cr} for the core drop at the end of shear breakup, as well as values of Eo_{cr} measured for freely-falling drops of various liquids in both gases and liquids from Merrington & Richardson (1947), Finlay (1957), Ryan (1976) and Hu & Kintner (1955). The conventional definition of the Eötvös number for freely-falling drops is as follows (Clift *et al.* 1978):

$$Eo_{cr} = g|\rho_L - \rho_G|d^2/\sigma,$$ [9]

where d is the maximum stable drop diameter, g is the acceleration of gravity and ρ_G should be interpreted as the density of the continuous phase (and is liquid for freely-falling drops in liquids). In addition to Eo_{cr}, table 2 provides the values of d, ρ_L, μ_L, σ, Oh_{cr} and We_{cr} for the various breakup processes.

For conditions at the end of shear breakup in table 2, d_b, Oh_{cr} and We_{cr} vary over ranges set by the present test conditions, which is evident from figure 4, even though Eo_{cr} is relatively constant. In contrast, stable freely-falling drop conditions involve single values of d, Oh_{cr} and We_{cr} for given

drop and continuous phases. In this case, We_{cr} and Eo_{cr} are closely related because the freely-falling drops eventually stabilize at their terminal velocity where the maximum value of We is reached. Remarkably, the average values of Eo_{cr} are not very different for the end of shear breakup and for the onset of breakup for freely-falling drops in both gases and liquids, 16 and 12, respectively. Differences of this order certainly are reasonable because one process involves the end of drop stripping from the core drop, while the other represents a limit for the onset of bag breakup (Clift *et al.* 1978).

Loparev (1975) reports We_{cr} for the onset of drop breakup, generally by bag breakup, during gradually accelerating and decelerating gas flows in converging passages. An extensive range of conditions was studied but unfortunately the information provided is not sufficient to find values of Eo_{cr}. Nevertheless, values of We_{cr} for low-Oh_{cr} drops are similar to those in table 2 for freely-falling drops, suggesting similar values of Eo_{cr} as well. An interesting aspect of these measurements is that We_{cr} increases with increasing Oh_{cr} for glycerol mixtures, similar to the behavior observed during the present study for the end of shear breakup. This is not surprising, due to past observations of increasing We at the onset of breakup for shock-wave disturbances as Oh increases (Hinze 1955; Krzeczkowski 1980; Hsiang & Faeth 1992). Pending resolution of this issue, however, the present value of Eo_{cr} should be used with caution to find core drop properties when values of $Oh_{cr} > 0.032$.

The previous considerations suggest that We, Eo and time all are factors in drop breakup events at low Oh. These interactions are highlighted by the local values of We_{cr}, Eo_{cr} and t_{cr}/t^* for the various breakup events summarized in table 3. For abrupt disturbances, like the onset of secondary breakup due to shock-wave disturbances, local values of We_{cr} and Eo_{cr} were estimated at the time of breakup using measured values of drop drag in the deformation period. Thus, these values are lower than criteria normally given for breakup regime transitions due to drop acceleration prior to the onset of breakup. Similar to the normalized breakup time, the normalized time at the onset of breakup for shock-wave disturbances is a constant over a wide range of We, $t_{cr}/t^* = 1.6$. For this process, drops in the deformation period have local values of We and Eo that exceed limits for the onset of breakup, however, breakup does not begin until the drop has had time to deform and achieve a dynamical condition in the liquid that allows drops to separate from the parent drop. The characteristics of We_{cr}, Eo_{cr} and t_{cr}/t^* are somewhat different for gradual disturbances. In the case of bag breakup for a freely-falling drop, Eo, based on the actual drop acceleration, is a maximum at the start of free fall while t_{cr}/t^* is large due to the relatively slow acceleration of the drop. Thus, liquid properties are roughly quasisteady at each relative velocity condition and breakup only occurs when forces on the drop surface due to drag are too large to be stabilized by surface tension, i.e. when the We of the drop reaches a critical value. Finally, the end of drop stripping for shear breakup also involves near-quasisteady liquid behavior with the dynamical state of the drop being stabilized by surface tension once the forces on the surface, represented by the drop acceleration, become lower than a critical value represented by Eo_{cr}. A range of We_{cr} is associated with this condition due to the large variation of the drag coefficient with the degree of deformation of the drop. Thus, various breakup events are associated with required minimum values of We, Eo and time, with one of these parameters generally serving as the controlling parameter for a particular process.

Table 3. Criteria for secondary breakup processes[a]

Process	We_{cr}	Eo_{cr}	t_{cr}/t^*
Abrupt (shock-wave) disturbances			
Start of bag breakup (in gases)	8–23	24–70	1.6
Start of multimode breakup (in gases)	23–53	70–160	1.6
Start of shear breakup (in gases)	≥53	≥160	1.6
Gradual disturbances			
Start of bag breakup (in gases)[b]	11–13	11	Large
Start of bag breakup (in liquids)[b]	7–9	15	Large
End of shear breakup (in gases)	8–29[c]	16	5.5

[a]Oh < 0.05, We_{cr} and Eo_{cr} subsequently increase with increasing Oh.
[b]Freely-falling drops in a motionless environment.
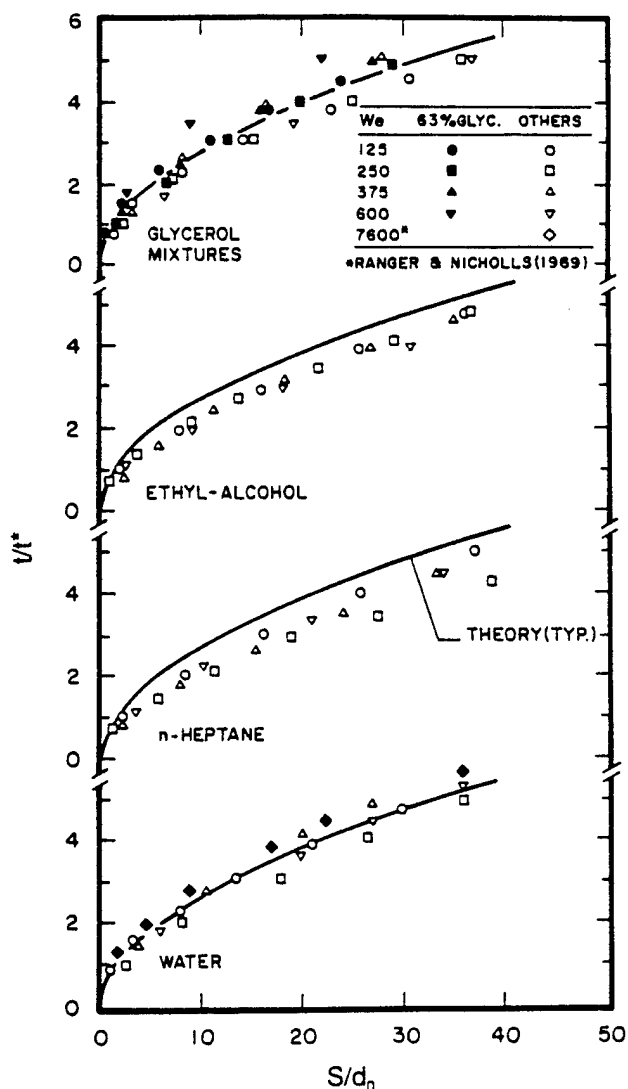[c]Present test range with wider range probable.

Figure 5. Displacements of core drops during the breakup period.

3.4. Core Drop Displacement

The analysis to find core drop velocities after secondary breakup was extended to find the displacement of the core drop as a function of time during secondary breakup. This provides a means of further evaluating the simplified analysis using measurements of core drop displacements, as well as providing a measure of the spatial extent of the shear breakup process.

The displacement of the core drop was found using the same assumptions employed to find the velocity of the core drop at the end of secondary breakup. This involved substituting u from [2] into the expression for the absolute velocity of the core drop, $u' = u_0 - u$, and integrating the resulting expression with respect to time. This yields the following expression for the displacement of the core drop, S, as a function of time after the arrival of the velocity disturbance:

$$S/d_0 = 3\bar{C}_D(t_b/2Ct^*)^2[Ct/t_b - \ln(1 + Ct/t_b)], \qquad [10]$$

where C is found from [4] using $t_b/t^* = 5$ and $\bar{C}_D = 5$, as before. Having made these selections, S/d_0 as a function of t/t^* only varies with the gas/liquid density ratio when C is computed from [4].

Predicted and measured core drop displacements are plotted as a function of time in figure 5. Measured results for the glycerol mixtures are combined on one plot because values of the gas/liquid density ratio are nearly the same for the two mixtures. Results for ethyl alcohol,

n-heptane and water are plotted separately in order to reduce the overlap of the data. The earlier measurements of Ranger & Nicholls (1969) for water also are shown on the plot: these results are in good agreement with the present measurements. In view of the simplifications used to find [10], the comparison between predictions and measurements is reasonably good. The main discrepancies are observed for ethyl alcohol and n-heptane, where the time required to reach a particular displacement is overestimated by roughly 10% for conditions near the end of breakup. Finally, the values of S/d_0 are roughly 40 at the end of breakup, thus, secondary breakup is approximated only crudely as a local event.

3.5. Drop-Size/Velocity Correlation

The last aspect of secondary breakup considered was the drop-size/velocity correlation at the completion of secondary breakup. These results will include all the drops in the bag and multimode breakup regimes. However, the core drop will be excluded in the shear breakup regime because its properties have already been established.

A simplified analysis, similar to the approach used for core drop velocities, was used to assist the correlation of drop velocity data. This involved neglecting virtual mass, Bassett history and gravitational forces and taking gas properties to be constant, as before. It also was assumed that a constant average drag coefficient was appropriate over the period of breakup, but provision was made to vary the average drag coefficient with drop size due to the large range of drop sizes that must be considered. Similarly, drops of various sizes are formed at different times during the breakup period, so that variations of residence times as separated drops in the gas phase were considered as well. Although the resulting approach still is rather crude, it did yield results that were useful for correlating the velocity measurements.

Based on these assumptions, the governing equation of conservation of momentum for a drop having a diameter, d, and relative velocity, u, and an average drag coefficient, $\bar{C}_{Dd}$, is as follows:

$$\mathrm{d}u/\mathrm{d}t = -3\bar{C}_{Dd}\rho_G u^2/(4\rho_L d).\qquad\qquad[11]$$

integrating [11] from $t = 0$, where $u = u_0$, to $t = t_d$, where $u = u_b$, yields the following expression for the final relative velocity of the drop:

$$u_0/u_b - 1 = (3\bar{C}_D t_b/4t^*)(\bar{C}_{Dd}/\bar{C}_D)(t_d/t_b)(\rho_G/\rho_L)^{1/2}(d_0/d).\qquad\qquad[12]$$

The functions, $\bar{C}_{Dd}/\bar{C}_D$ and t_d/t_b are unknown but based on [12] it seems reasonable to plot $u_0/u_b - 1$ as a function of $(\rho_G/\rho_L)^{1/2}(d_0/d)$.

The resulting drop-size/velocity correlation based on these considerations is plotted in figure 6. The test results involve all drop liquids over the data range summarized in table 1, including the bag, multimode and shear breakup regimes. Results for the core drops have been shown as dark symbols, for comparison purposes, but they are not included in the following drop-size/velocity correlation. The measured results clearly are independent of the breakup regime and can be correlated reasonably well using the following empirical fit based on [12]:

$$u_0/u_b - 1 = 2.7[(\rho_G/\rho_L)^{1/2}d_0/d]^{2/3}.\qquad\qquad[13]$$

Thus, the reduction of the power of $[(\rho_G/\rho_L)^{1/2}d_0/d]$ from [12] to [13] is relatively modest in view of potential complications due to $\bar{C}_{Dd}/\bar{C}_D$ and t_d/t_b. Additionally, [13] appears to be rather robust over the three breakup regimes, the range of liquid types and the flow conditions considered during the present experiments. Even the results for core drops are in fair agreement with [13], however, the specific relationships for core drops discussed earlier provide a better estimate of their velocities. Finally, the results indicate that relative velocities are reduced 30–70% over the period of breakup, with the smallest drops experiencing the largest reduction of relative velocity due to their smaller relaxation times.

4. CONCLUSIONS

The outcome of secondary breakup after shock-wave-initiated disturbances was studied, considering drops of water, n-heptane, ethyl alcohol and glycerol in air at normal temperature and
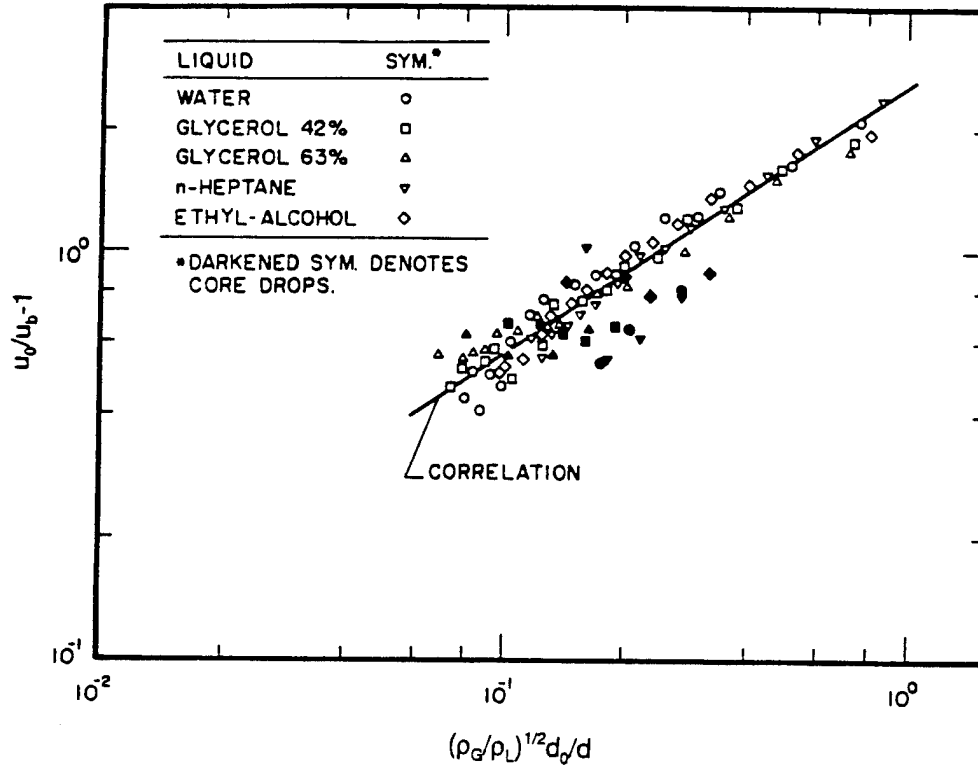
Figure 6. Correlation of drop velocities after secondary breakup as a function of drop size.

pressure (We of 15–600, Oh of 0.0025–0.039, ρ_L/ρ_G of 579–985 and Re of 1060–15080). The major conclusions of the study are as follows:

1. Earlier problems with the drop size distribution after shear breakup (Hsiang & Faeth 1992) were resolved by removing the core drop from the drop population and treating it separately. With this change, drop sizes after breakup in all three breakup regimes satisfy Simmons' universal root normal distribution with MMD/SMD = 1.2. Removal of the core drop from the drop size distribution has a negligible effect on the SMD correlation of Hsiang & Faeth (1992) which can be used as before.

2. The velocity and size of the core drop after shear breakup were correlated and successfully based on simplified considerations of drop motion during breakup, [3], and the observation that the Eo at the end of drop stripping was a constant, [7], i.e. $Eo_{cr} = 16$.

3. The relative velocities of the drop liquid are significantly reduced during secondary breakup (30–70%, depending on drop size) due to the large drag coefficients during the drop deformation stage and the reduced relaxation times of smaller drops. These effects were correlated successfully based on variables from simplified analysis of drop motion (figure 6 and [13]).

4. At low Oh, criteria for various drop breakup processes can be represented by critical values of We, Eo and t/t^*. While certain minimum values are required for all three parameters, reaching a critical local value of one of the parameters tends to control the onset of particular breakup events: t_{cr}/t^* for the onset of breakup after a shock-wave disturbance, We_{cr} for the onset of breakup of a freely-falling drop and Eo_{cr} for the end of drop stripping from the core drop during shear breakup.

The present findings generally were limited to Oh < 0.039, with results concerning core drop properties limited to Oh < 0.011. Increasing Oh tends to impede drop deformation and breakup

processes and should modify secondary breakup behavior considerably from the results observed during the present study. The liquid/gas density ratios of present work also were relatively limited and are most appropriate for sprays at atmospheric pressure. Effects of both Oh and ρ_L/ρ_G clearly merit additional study in order to better understand secondary breakup properties.

REFERENCES

BORISOV, A. A., GEL'FAND, B. E., NATANZON, M. S. & KOSSOV, O. M. 1981 Droplet breakup regimes and criteria for their existence. *Inzh.-Fiz. Zh.* **40**, 64–70.

CLIFT, R., GRACE, J. R. & WEBER, M. E. 1978 *Bubbles, Drops and Particles*, pp. 26 & 339–347. Academic Press, New York.

DABORA, E. K. 1967 Production of monodisperse sprays. *Rev. Scient. Instrum.* **38**, 502–506.

FAETH, G. M. 1987 Mixing, transport and combustion in sprays. *Prog. Energy Combust. Sci.* **13**, 293–345.

FINLAY, B. A. 1957 Ph.D. Thesis, Univ. of Birmingham, W. Midlands, U.K.

GEL'FAND, B. E., GUBIN, S. A. & KOGARKO, S. M. 1974 Various forms of drop fractionation in shock waves and their special characteristics. *Inzh.-Fiz. Zh.* **27**, 119–126.

GIFFEN, E. & MURASZEW, A. 1953 *The Atomization of Liquid Fuels*. Chapman & Hall, London.

HANSON, A. R., DOMICH, E. G. & ADAMS, H. S. 1963 Shock-tube investigation of the breakup of drops by air blasts. *Phys. Fluids* **6**, 1070–1080.

HINZE, J. O. 1955 Fundamentals of the hydrodynamic mechanism of splitting in dispersion processes. *AIChE Jl* **1**, 289–295.

HSIANG, L.-P. & FAETH, G. M. 1992 Near-limit drop deformation and secondary breakup. *Int. J. Multiphase Flow* **18**, 635–652.

HU, S. & KINTNER, R. C. 1955 The fall of single drops through water. *AIChE Jl* **1**, 42–48.

KRZECZKOWSKI, S. A. 1980 Measurement of liquid droplet disintegration mechanisms. *Int. J. Multiphase Flow* **6**, 227–239.

LANGE, N. A. 1952 *Handbook of Chemistry*, 8th edn, pp. 1134 & 1709. Handbook Publishers, Sandusky, OH.

LIANG, P. Y., EASTES, T. W. & GHARAKHARI, A. 1988 Computer simulations of drop deformation and drop breakup. AIAA Paper No. 88-3142.

LOPAREV, V. P. 1975 Experimental investigation of the atomization of drops of liquid under conditions of a gradual rise of the external forces. *Izv. Akad. Nauk SSSR Mekh. Zhidkosti i Gaza* **3**, 174–178.

MERRINGTON, A. C. & RICHARDSON, E. G. 1947 The break-up of liquid jets. *Proc. Phys. Soc. (Lond.)* **59**, 1–13.

RANGER, A. A. & NICHOLLS, J. A. 1969 The aerodynamic shattering of liquid drops. *AIAA Jl* **7**, 285–290.

REINECKE, W. G. & MCKAY, W. L. 1969 Experiments on waterdrop breakup behind Mach 3 to 12 shocks. Report SC-CR-70-6063, Sandia Corp., Albuquerque, NM.

REINECKE, W. G. & WALDMAN, G. D. 1970 A study of drop breakup behind strong shocks with applications to flight. Avco Report AVSD-0110-70-77.

RUFF, G. A., WU, P.-K., BERNAL, L. P. & FAETH, G. M. 1992 Continuous- and dispersed-phase structure of dense nonevaporating pressure-atomized sprays. *J. Propul. Power* **8**, 280–289.

RYAN, R. T. 1976 The behavior of large low-surface-tension water drops falling at terminal velocity in air. *J. Appl. Met.* **15**, 157–165.

SANGIOVANNI, J. & KESTIN, A. S. 1977 A theoretical and experimental investigation of the ignition of fuel droplets. *Combust. Sci. Technol.* **16**, 59–70.

SIMMONS, H. C. 1977 The correlation of drop-size distributions in fuel nozzle sprays. *J. Engng Power* **99**, 309–319.

WHITE, F. M. 1974 *Viscous Fluid Flow*. McGraw-Hill, New York.

WIERZBA, A. & TAKAYAMA, K. 1987 Experimental investigations on liquid droplet breakup in a gas stream. *Rep. Inst. High Speed Mech., Tohoku Univ.* **53**, 1–99.

WIERZBA, A. & TAKAYAMA, K. 1988 Experimental investigation of the aerodynamic breakup of liquid drops. *AIAA Jl* **26**, 1329–1335.

WU, P.-K. & FAETH, G. M. 1992 Aerodynamic effects on primary breakup of turbulent liquids. *Atomiz. Sprays*. In press.

WU, P.-K.. RUFF, G. A. & FAETH, G. M. 1991 Primary breakup in liquid/gas mixing layers. *Atomiz. Sprays* **1**, 421–440.

WU, P.-K., TSENG, L.-K. & FAETH, G. M. 1992 Primary breakup in gas/liquid mixing layers for turbulent liquids. *Atomiz. Sprays* **2**, 295–317.

Appendix B: Hsiang, L.-P. and Faeth, G.M. (1995) Drop deformation and breakup due to shock wave and steady disturbances. <u>Int. J. Multiphase Flow</u> 21, 545-560.

Pergamon

0301-9322(94)00095-6

DROP DEFORMATION AND BREAKUP DUE TO SHOCK WAVE AND STEADY DISTURBANCES

L.-P. HSIANG and G. M. FAETH†

Department of Aerospace Engineering, The University of Michigan, Ann Arbor, MI 48109-2118, U.S.A.

Abstract—An experimental study of drop deformation properties induced by both shock wave and steady disturbances is described. Three test facilities were used, as follows: a shock tube facility for measurements of effects of shock wave disturbances on drops in gases, a 10 m high drop tube facility for measurements of effects of steady disturbances on drops in gases and a 1 m high drop tube facility for measurements of effects of steady disturbances on drops in liquids. Various dispersed and continuous phase gases and liquids were considered to provide dispersed continuous phase density ratios of 1.15–12,000, Ohnesorge numbers of 0.0006–600, Weber numbers of 0.004–700 and Reynolds numbers of 0.03–16,000. At low Ohnesorge numbers (< 0.1) for all types of disturbances, significant drop deformation (5%) began at Weber numbers of roughly unity, with the deformation regime ending due to the onset of breakup at Weber numbers of 10–20. These transitions were relatively unaffected by the Ohnesorge number for steady disturbances, however, increasing Ohnesorge numbers caused progressive increases of the Weber number range for both deformation and breakup regimes for shock wave disturbances—an effect that could be explained using phenomenological theory. Another transition, between dome- and bowl-shaped drops (related to the transition between bag and shear breakup), was correlated mainly in terms of Weber and Reynolds numbers for present conditions. Drop deformation for steady disturbances was relatively independent of dispersed continuous phase density ratios but generally was smaller than for shock wave disturbances at comparable conditions due to the absence of overshoot from inertial effects. In contrast, drop drag coefficients, normalized by the drag coefficient of a solid sphere at the same Reynolds number, were correlated quite well by the degree of deformation alone.

Key Words: drop deformation, drop dynamics, drop breakup, atomization, pulsed holography

1. INTRODUCTION

Processes of deformation and secondary breakup of drops have received significant attention as important classical multiphase flow phenomena with numerous practical applications, e.g. industrial and agricultural sprays, liquid-fueled power and propulsion systems, and rainfall, among others. In particular, recent studies suggest that secondary breakup is a rate-controlling process in the near-injector region of pressure-atomized sprays, through its effect on drop sizes (Ruff *et al.* 1992). Additionally, primary breakup at the surface of non-turbulent and turbulent liquids yields drops that intrinsically are unstable to secondary breakup (Wu *et al.* 1991, 1992), supporting the classical description that atomization occurs by primary breakup near a liquid surface followed by secondary breakup (Faeth 1990). Finally high pressure combustion involves conditions where the drop surface tension becomes small because the liquid surface approaches the thermodynamic critical point: such conditions also imply significant effects of secondary drop deformation and breakup. Motivated by these observations, the objectives of the present investigation were to extend earlier studies of secondary drop deformation and breakup in this laboratory, due to Hsiang & Faeth (1992, 1993), emphasizing the properties of drop deformation from both shock wave and continuous disturbances.

Past work on drop deformation and breakup will only be considered briefly [see Wierzba & Takayama (1987), Giffen & Muraszew (1953), Hinze (1955), Krzeczkowski (1980), Clift *et al.* (1978) and references cited therein, for more complete reviews]. Past work generally has been limited to two kinds of well-defined disturbances that cause deformation and breakup of drops: shock wave disturbances that provide step changes in the ambient environment of a drop, e.g. representing a

†To whom correspondence should be addressed.

drop at the end of rapid primary breakup: and steady disturbances. e.g representing freely-falling drops in a rainstorm or a mixing column. Effects of shock wave disturbances have received the most attention with high-speed photography used to identify deformation and secondary breakup regimes. Measurements of transitions between breakup regimes have been limited to dispersed continuous-phase density ratios. $\rho_d/\rho_c > 500$ and Reynolds numbers. $Re = \rho \, d_o u_o \, \mu_c > 500$. where d_o and u_o denote the original drop diameter and relative velocity and μ_c is the continuous-phase viscosity. For these conditions. Hinze (1955) shows that breakup regime transitions largely are functions of the ratio of drag to surface tension forces. represented by the Weber number. $We = \rho_c d_o u_o^2 \, \sigma$. and the ratio of liquid viscous to surface tension forces. represented by the Ohnesorge number. $Oh = \mu_d \, /(\rho_d d_o \sigma)^{1/2}$, where σ is the surface tension and μ_d is the dispersed-phase viscosity. At low Oh. drop deformation becomes significant at We of roughly 1 and drop breakup becomes significant at We of roughly 10. with bag. multimode and shear breakup regimes observed at progressively larger We [see Wierzba & Takayama (1987). Giffen & Muraszew (1953). Hinze (1955). Krzeckowski (1980) and Clift et al. (1978) for photographs and detailed descriptions of the various types of drop breakup]. With increasing Oh. however. progressively larger We are required for the onset of drop deformation and breakup because viscous forces inhibit drop deformation which is the first stage of the breakup process. This behavior has been confirmed by several investigations. however. maximum values of $Oh < 4$ so that behavior at large Oh has not been resolved. This is unfortunate because high pressure combustion processes involve large Oh as a result of drop surfaces approaching the thermodynamic critical point. This behavior occurs because surface tension becomes small while liquid viscosity remains finite as liquid surfaces approach their thermodynamic critical point (Faeth 1990). Thus. whether combustion at high pressures involves enhanced. or entirely suppressed. effects of secondary breakup has not yet been resolved.

The time required for breakup is another aspect of secondary breakup that has received significant attention for shock wave disturbances at $\rho_d/\rho_c > 500$. At low Oh. Liang et al. (1988) found that breakup times normalized by the characteristic breakup time of Ranger & Nicholls (1969). $t^* = d_o(\rho_d \, \rho_c)^{1/2} \, u_o$. were remarkably independent of both the breakup regime and We. As might be expected from the effect of Oh on breakup regimes. however. breakup times have been observed to increase with increasing Oh (Hsiang & Faeth 1992). Additionally. processes of drop deformation. and the variation of drop drag coefficient with time. also appear to scale systematically in terms of t^* at low Oh but behavior at large Oh is uncertain.

Finally. the outcome of secondary breakup for shock wave disturbances at $\rho_d \, \rho_c > 500$ and small Oh also has received attention (Hsiang & Faeth 1993: Gel'fand et al. 1974). It was found that drop size distributions after secondary breakup satisfied the universal root normal distribution of Simmons (1977) in all three breakup regimes. after removing the core (or drop forming) drop from the drop population for shear breakup. The size and velocity of the core drop after shear breakup then was correlated successfully based on the observation that the end of drop stripping corresponded to a constant Eötvös number. $Eo = a\rho_d d_o^2 \, \sigma$ where $a =$ drop acceleration (Hsiang & Faeth 1993). The relative velocities of the drop liquid were significantly reduced after secondary breakup. which could be correlated successfully based on simplified phenomenological theory (Hsiang & Faeth 1993). These results showed that secondary breakup processes extend over a significant region. roughly 40 initial drop diameters. Thus. secondary breakup is not a particularly localized event which raises concerns about its dynamics. e.g. liquid motion during breakup. the distribution of drop liquid in space and time. etc. Work treating these issues. however. has not yet been reported.

Drop deformation and breakup for steady disturbances also has been studied. motivated by interest in the properties of rain and liquid–liquid extraction equipment. The main objective of this work has been to develop ways to estimate the velocity of fall of particular sized drops in gas and liquid environments. and to determine conditions for drop breakup. It has been found that We for breakup are comparable for steady and shock wave disturbances. However. the properties of breakup for steady disturbances are not well understood due to the intrusion of processes of drop formation. For example. whether the mechanism of breakup is due to nozzle-induced disturbances. bag breakup. simple splitting into a few drops or is significantly affected by collisions. still has not been resolved (Pruppacher & Pitter 1971; Ryan 1976). Other areas of uncertainty involve relationships between drop deformation and drag. effects of large Oh and the relationships between

the parameters of dispersed and continuous phases and the drop shape. Since steady disturbances provide conditions where drop deformation and breakup response to disturbance levels are relatively simple to interpret and to correlate, it is clear that more progress on effects of steady disturbances must be made before the more complex processes involving shock wave or more general disturbances can be understood.

The objective of the present investigation was to extend the work of Hsiang & Faeth (1992, 1993) in order to help resolve some of the issues discussed in the preceding review of the literature. Foremost among these issues is the nature of the deformation and breakup regime map for shock wave disturbances at large Oh. Other issues considered involved factors influencing drop deformation and shape, emphasizing effects of the dispersed continuous phase density ratio, and the relationship between drop drag and deformation in various environments. These problems were addressed using three test facilities, as follows: a shock tube facility for measurements of effects of shock wave disturbances on drops in gases, a 10 m high drop tube facility for measurements of effects of steady disturbances on drops in gases, and a 1 m high drop tube facility for measurements of effects of steady disturbances on drops in liquids. Various dispersed and continuous phase gases and liquids were used to provide ρ_d/ρ_c of 1.15–12,000, Oh of 0.0005–600, We of 0.004–700 and Re of 0.03–16,000. Phenomenological analysis was used to help interpret and correlate some aspects of the measurements.

The paper begins with a discussion of experimental methods. Results are then considered, treating drop deformation and breakup regimes, drop deformation and drop drag, in turn.

2. EXPERIMENTAL METHODS

2.1. Shock tube

Apparatus. The shock tube apparatus involved a driven section open to the atmosphere, similar to earlier work in this laboratory (Hsiang & Faeth 1992, 1993). The driven section had a rectangular cross section (38 mm wide × 64 mm high) and a length of 6.7 m with the test location 4.0 m from the downstream end. This provided test times of 17–21 ms in the uniform flow region behind the incident shock wave. In particular, worst-case variations of continuous phase properties during breakup processes were less than 5%. The test location had quartz windows (25 mm high × 305 mm long, mounted flush with the interior side walls of the shock tube) to allow observation of drop breakup. Breakup was observed in air initially at 98 kPa and 297 ± 2 K in the driven section of the shock tube with shock Mach numbers in the range 1.08–1.31. Instrumentation was synchronized with the passing of the shock wave using the piezoelectric pressure transducers that monitored the strength of the shock wave in the driven section.

Two different drop generator systems were used for the shock tube experiments. Operation at low and moderate Oh involved the use of a vibrating capillary tube drop generator, similar to Dabora (1967), which generated a stream of drops. This drop stream passed through 6 mm diameter holes in the top and bottom of the shock tube, crossing the central plane of the driven section at the test location. An electrostatic drop selection system, similar to Sanjiovanni & Kestin (1977), was used to deflect a fraction of the drops out of the stream. This yielded a drop spacing of roughly 7 mm so that drops were always present in the region observed while interactions between drops during secondary breakup were eliminated.

Drop generation for large Oh conditions required a different approach. In particular, it is very difficult to form a drop that has a large Oh; instead, such drops generally evolve to these conditions after formation at low Oh, e.g. large Oh conditions are approached during high pressure combustion because the drop surface eventually becomes heated to conditions near the thermodynamic critical point. The approach taken during the present investigation was to form a low Oh drop from a liquid solution, and to levitate the drop at the test location until the solvent evaporated away, leaving a small drop consisting of a highly viscous liquid which provided the desired large Oh condition. Dow Corning 200 Fluids having unusually large viscosities (10,000 and 30,000 mP) were used for the viscous liquids, with *n*-heptane used as the volatile solvent. Original drop diameters were in the range 320–700 μm, with final drop diameters of 160–350 μm, which required several minutes to complete evaporation of the solvent.

The levitation system consisted of a horn and reflector having diameters of 10 mm that were positioned near the top and bottom of the test section (roughly 55 mm apart). Two 50 mm diameter piezoelectric ceramic elements, combined with a central mount and a resonator, were used to power the horn. The horn operated at a frequency of roughly 47 kHz with the tip of the horn having an amplitude of roughly 200 μm. The piezoelectric ceramic elements were actuated using a Wilcoxan, Model PA8-1 power supply (110 V, 8 A maximum output conditions) operating at the required frequency. A step up transformer was used to increase the output voltage to 1000 V in order to properly drive the ceramic elements. This circuit also incorporated proper impedance matching circuitry for the ceramic elements. The horn driving unit was cooled with an air blower system. The long shank of the horn also helped to minimize thermal disturbances, due to the large power dissipation of the horn driving unit, within the test section. The drops were placed in the acoustic field of the horn and reflector system using a hypodermic syringe. Access to the test section for the syringe was provided by a port that could be sealed by a cap screw, whose inner end was flush with the inside wall of the test section.

Instrumentation. The deformation and breakup process was observed using pulsed shadowgraph motion pictures, similar to earlier work (Hsiang & Faeth 1992, 1993). A copper vapor laser was used as the light source with a 35 mm drum camera used to record the shadowgraph images at unity magnification. A function generator was used to pulse the laser when the shock wave neared the drop stream location, with pulse frequencies of 6–8 kHz for 20 pulses. Each laser pulse duration was 30 ns, which was sufficient to stop the motion of the drop on the rotating film drum. The drum camera recorded the images with an open shutter within a darkened room. The time between shadowgraph pictures was monitored by recording the signal generator output using a digital oscilloscope.

The film records were analyzed using a Gould FD 5000 Image Display. The procedure was to obtain three motion picture shadowgraphs for a particular test condition and group the data to obtain statistically-significant results as ensemble averages. Experimental uncertainties (95% confidence) of the measurements reported here are as follows: relative velocities, less than 10%; initial drop diameter and subsequent drop dimensions, less than 10%; and drop drag coefficients, less than 30%, limited by the accuracy of finding drop centroid motion at small times after passage of the shock wave. Corresponding uncertainties of parameters reported here will be presented when the parameters are discussed.

Test conditions. Test conditions are summarized in table 1. Including results of earlier work (Hsiang & Faeth 1992), test drops of water, *n*-heptane, mercury, two Dow Corning 200 Fluids and various glycerol mixtures were used to provide a wide range of liquid properties. The liquid properties listed in table 1 were obtained from Lange (1952), except for the properties of the Dow Corning 200 Fluids which were obtained from the manufacturer, and the surface tensions of the glycerol mixtures which were measured in the same manner as Wu *et al.* (1991). Initial drop diameters were in the range 150–1550 μm. Ranges of other variables are as follows: ρ_d/ρ_c of 500–12,000, Oh of 0.0006–560, We of 0.5–680 and Re of 340–15,760. The We range includes

Table 1. Summary of liquid–air shock tube test conditions[†]

Dispersed phase	ρ_d (kg m^{-1})	$\mu_d \times 10^4$ (kg ms)	$\sigma \times 10^3$ (N m)	d_o (mm)	We	Oh	Re
Water	997	8.94	70.8	1.0	0.5–236	0.0038	340–8250
n-Heptane	683	3.94	20.0	0.5	14–137	0.0036	720–2270
Mercury	13,600	15.0	475.0	0.85	10–13	0.00062	3510–4500
DC200 Fluid[‡]	980	100,000	20.0	0.15–0.35	35–100	120–185	980–1700
DC200 Fluid[‡]	980	300,000	20.0	0.15–0.35	100–680	365–555	1170–5200
Glycerol 21%	1050	16.0	67.3	1.2	8–130	0.0071	1540–6390
Glycerol 63%	1162	108.0	64.8	1.2	1–129	0.0390	480–6420
Glycerol 75%	1195	356.0	63.8	1.2	2–128	0.0990	730–6270
Glycerol 84%	1219	1000	63.2	1.2	1–127	0.260	500–6210
Glycerol 92%	1240	3270	62.5	1.2	1–268	1.050	530–8330
Glycerol 97%	1253	8350	62.4	1.5	1–205	1.700	600–8880
Glycerol 99.5%	1260	12,500	62.0	1.55	1–612	3.850	630–15760

[†]Air initially at 98.8 kPa and 298 ± 3 K in a driven section of shock tube with shock Mach numbers in the range 1.01–1.24.
  Properties of air taken at normal temperature and pressure: $\rho_c = 1.18$ kg m^3, $\mu_c = 18.5 \times 10^{-6}$ kg/m s.
[‡]Dow Corning 200 fluid.

processes from no deformation into the shear breakup regime of interest to phenomena within dense sprays (Faeth 1990), but does not reach the catastrophic breakup regime studied by Reinecke *et al.* (1969, 1970). The Re range of these measurements is higher than conditions where gas viscosity plays a strong role in drop drag properties; within the present Reynolds number range, the drag coefficient for spheres only varies in the range 0.6–0.4 (Faeth 1990; White 1974). The shock waves were weak to modest so that the physical properties of the gas were essentially the same as room temperature air.

2.2. Drop towers

Apparatus. Gas–liquid and liquid–liquid drop towers were used for tests with steady disturbances. The gas-liquid drop tower was constructed of PVC pipe having an inside diameter of 300 mm and a height of 9.2 m, that was open at the top and the bottom. Drops were released along the axis of the tube, at its top, using a simple buret system. The drops were widely spaced, and reached terminal velocities at roughly 5 m, well before the tube exit. Measurements were made when the drops were roughly 200 mm below the bottom of the tube. Instrumentation was synchronized with the passing of the drop using a simple light interception triggering system based on a HeNe laser directed across the exit of the PVC pipe. Drops were collected in a flask at the end of their fall.

The liquid–liquid drop tower was constructed of Plexiglas to provide a 150×150 mm cross section and a vertical height of 1.2 m. The dispersed (drop) and continuous phase liquids were immiscible, and were fully saturated with the other liquid prior to testing. The drop liquid was released using a buret discharging under the surface of the continuous phase liquid. The method of drop introduction was not important for present results, however, because terminal velocity conditions were reached well before the region where measurements were made. Present test conditions did not involve oscillating drops. Measurements were made roughly 300 mm above the bottom of the tank. Drop motion for these conditions was very slow so that it was possible to use manual synchronization when obtaining test records. Drops simply collected at the bottom of the drop tower as an immiscible liquid layer that was removed from time to time.

Instrumentation. Drops were observed using single- and double-pulsed shadowgraph photographs. The light source was a General Radio lamp (type U-31A) with a flash duration of roughly 1 μs. The lamp output was collimated and directed horizontally through the axis of the drop tower. The image was recorded using a Graphlex camera (4×5 in. film format, Polaroid Type 55 film) at a magnification of 6:1. The photographs were obtained in a darkened room using an open camera shutter. The time of separation between pulses was controlled by a function generator. As noted earlier, the time of the first photograph was controlled by a light interception system for the liquid-gas experiments, and manually for the liquid–liquid experiments. These images were processed similar to the shock tube measurements. Experimental uncertainties (95% confidence) of the measurements reported here are as follows: drop velocities, less than 5%; drop dimensions, less than 5%; and drop drag coefficient, less than 10%. The latter two uncertainties were dominated by finite sampling accuracy. As before, corresponding uncertainties of parameters reported here will be presented when the parameters are discussed.

The effective diameters of the drops were computed similar to earlier work (Hsiang & Faeth 1992, 1993). This involved measuring maximum and minimum diameters through the centroid of the image: d_{max} and d_{min}. Assuming ellipsoidal shapes, the diameter was then taken to be the diameter of a sphere having the same volume; namely, $d^3 = d_{min}^2 d_{max}$.

Test conditions. Test conditions for drops falling at their terminal velocities in air are summarized in table 2. In this case, test liquids were limited to water and various glycerol mixtures, with properties found as described for table 1. Initial drop diameters were in the range 2.0–7.8 mm while the ranges of other variables were as follows: ρ_d / ρ_c of 845–1070, Oh of 0.0012–2.9, We of 1.2–9.8 and Re of 830–4600. In this case, the range of We was rather narrow because smaller values resulted in negligible drop deformation, while larger values caused drop breakup, over the available range of Oh. Similar to the test conditions of table 1, the present Reynolds number range involves a rather modest variation of drop drag coefficients.

Test conditions for the liquid–liquid drop tower experiments are summarized in table 3. Test liquids for the dispersed phase included water, ethylene glycol, various glycerol mixtures, carbon disulfide and a Dow Corning 200 Fluid having a viscosity of 30,000 ci". Test liquids for the

Table 2. Summary of liquid–air drop tower test conditions[†]

Dispersed phase	ρ_d (kg m³)	$\mu_d \times 10^4$ (kg ms)	$\sigma \times 10^3$ (N m)	d_o (mm)	We	Oh	Re
Water	997	8.94	70.8	2.0–7.8	1.2–9.8	0.0012–0.0024	830–46000
Glycerol 42%	1105	35.0	65.4	2.0–7.8	1.4–9.5	0.0046–0.0091	870–4210
Glycerol 63%	1162	108.0	64.8	2.0–7.8	1.5–9.8	0.0140–0.0275	880–4390
Glycerol 84%	1219	1000	63.2	2.0–7.8	1.7–9.5	0.126–0.248	940–4260
Glycerol 92%	1240	3270	62.5	2.5–6.4	2.5–8.6	0.455–0.729	1180–3500
Glycerol 99.5%	1260	12,500	62.0	2.4–6.4	2.3–8.6	1.74–2.90	1060–3450

[†]Air initially at 98.8 kPa and 297 ± 2 K. Properties of air taken at normal temperature and pressure: $\rho_c = 1.18$ kg m³, $\mu_c = 18.5 \times 10^{-6}$ kg m s.

Table 3. Summary of liquid–liquid drop tower test conditions[†]

Dispersed phase	Water	Ethylene glycol	Glycerol 84%	Glycerol 99.5%	Carbon disulfide	DC200 fluid
Continuous phase	Paraffin oil	Paraffin oil	Paraffin oil	Paraffin oil	Water	Paraffin oil
ρ_d (kg m³)	997	1110	1219	1260	1263	970
ρ_c (kg m³)	870	870	870	870	997	870
$\mu_d \times 10^4$ (kg ms)	8.9	145	632	12,500	6.5	300,000
$\mu_c \times 10^4$ (kg ms)	710–1050	1050	1050	1050	8.9	1050
$\sigma \times 10^3$ (N m)	46.8	39.0	39.5	32.1	45.6	22.0
d_o (mm)	6.8–58	4.0–31	5.2–7.3	6.0–22.5	1.8–5.6	0.1–0.6
We	0.2–20	0.1–7.4	0.5–2.0	0.5–24	0.2–3.5	0.004–0.06
Re	3.3–64	1.5–40	4.5–10	2.1–58	150–1190	0.03–0.75
Oh	$0.54–1.6 \times 10^{-1}$	$1.3–3.5 \times 10^{-2}$	0.16–0.20	1.3–2.5	$1.1–2.0 \times 10^{-1}$	77–215

[†]Liquids at 298 ± 3 K.

continuous phase included paraffin oil and water. Liquid properties were found as described in table 1, except that the properties of the paraffin oil also were obtained from the manufacturer. Initial drop diameters were in the range 0.1–58 mm while ranges of other variables were as follows: ρ_d/ρ_c of 1.15–1.45, Oh of 0.0005–215, We of 0.004–24 and Re of 0.03–1190. The We range was limited to conditions where interesting effects of deformation were observed but limited by the onset of breakup. The Re range extends from the Stokes regime to the region where the drag coefficient becomes relatively independent of Re (Faeth 1990; White 1974).

3. RESULTS AND DISCUSSION

3.1. Deformation and breakup regimes

Results for shock wave disturbances mainly involved extending the deformation and breakup regime map of Hsiang & Faeth (1992) to higher Oh, based on present results using the Dow Corning 200 Fluids. The resulting deformation and breakup regime map, showing transitions as functions of We and Oh similar to Hinze (1955) and Krzeczkowski (1980), is illustrated in figure 1. The experimental uncertainties (95% confidence) of present data values of We and Oh are less than 23 and 5%, respectively, due to the uncertainties of present drop diameter and velocity measurements. As noted in Hsiang & Faeth (1992), the various breakup regimes identified by Hinze (1955) and Krzeczkowski (1980), are in excellent agreement with the present measurements in the region where they overlap. This includes bag breakup at the onset of breakup, shear breakup that involves the stripping of liquid from the periphery of the drop, and the complex multimode breakup regime between them which merges aspects of the two bounding breakup regimes.

The transitions to the non-oscillatory and oscillatory deformation regimes illustrated in figure 1 have not been reported by others but are important because they define conditions where drop drag behavior departs significantly from that of a solid sphere. Thus, the first deformation regime involves the maximum (cross stream) dimension (normalized by the original drop diameter) in the range 1.05–1.10; with subsequent deformation regimes defined by this ratio being in the range 1.10–1.20 and greater than 1.20 but prior to transition to oscillatory deformation (at low Oh) or bag breakup (at large Oh). The oscillatory deformation regime is discussed in Hsiang & Faeth (1992): it is defined by conditions where the drop oscillated with a weakly damped amplitude (where the second peak of the drop diameter fluctuations exceeds a diameter ratio of 1.1).
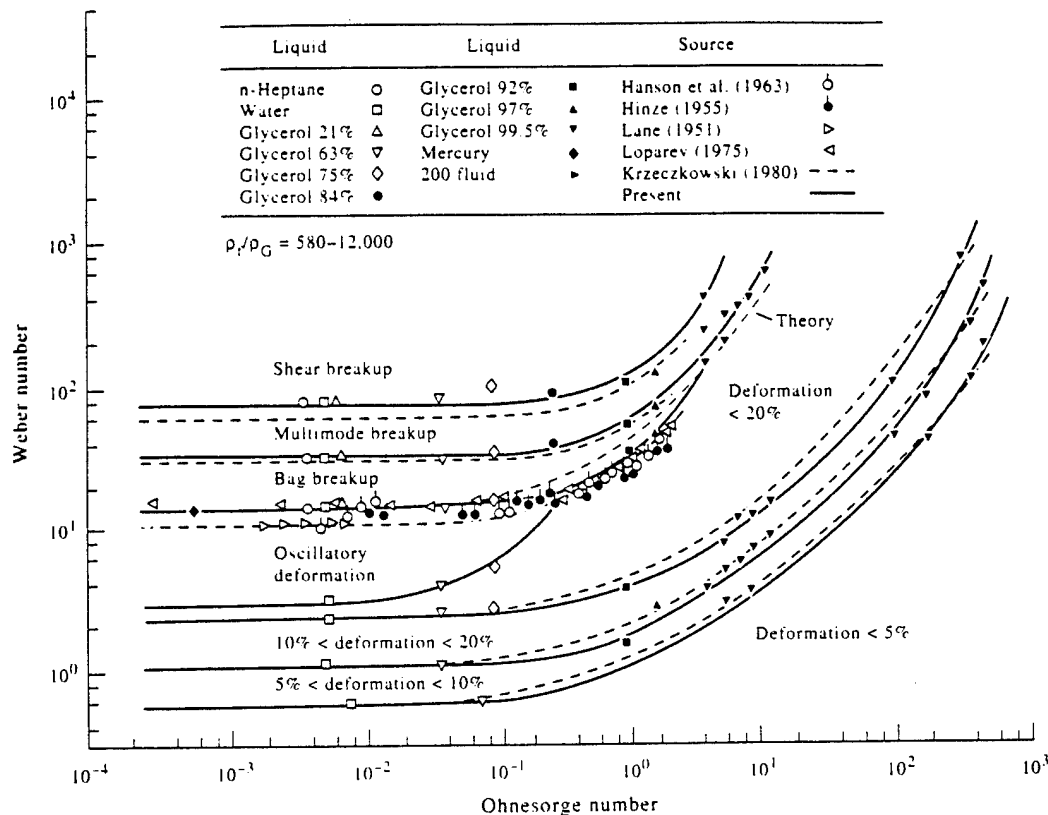
Liquid		Liquid		Source	
n-Heptane	O	Glycerol 92%	■	Hanson et al. (1963)	○
Water	□	Glycerol 97%	▲	Hinze (1955)	●
Glycerol 21%	△	Glycerol 99.5%	▼	Lane (1951)	▷
Glycerol 63%	▽	Mercury	◆	Loparev (1975)	◁
Glycerol 75%	◇	200 fluid	►	Krzeczkowski (1980)	− − −
Glycerol 84%	●			Present	——

Figure 1. Drop deformation and breakup regime map for shock wave disturbances.

Perhaps the most striking feature of figure 1 is that while the We required for particular deformation and breakup regime transitions remain relatively constant for small Oh (values less that 0.1), the We required for the various transitions progressively increase with increasing Oh at large Oh (values greater than 1). Thus the onset of deformation (5–10% deformation) and breakup (bag breakup) occur at We of roughly 0.6 and 13 for Oh < 0.1; however, breakup no longer is observed for We < 1000 when Oh > 10 while deformation (5–10% deformation) disappears for a similar We range when Oh > 1000. Other deformation and breakup regimes observed at low Oh also disappear with increasing Oh, e.g. oscillatory deformation at Oh of roughly 0.3 and bag breakup at Oh of roughly 4. Hinze (1955) observed this tendency for the limited range of Oh available at the time (Oh < 1) and conjectured that breakup might no longer be observed for Oh > 2. However, the large Oh behavior observed in figure 1 does not suggest such a limitation; rather, there is a progressive (almost linear) increase of We at the deformation and breakup transitions, with increasing Oh. Clearly it is crucial to establish whether large Oh implies no deformation or breakup as suggested by Hinze (1955), or simply rather large values of We at the transitions, as suggested by the measurements illustrated, in figure 1. Thus, phenomenological analysis is considered next in order to gain more insight about effects of large Oh on deformation and breakup regime transitions.

Based on drop deformation results for steady disturbances, to be discussed subsequently, it did not appear that the liquid viscosity had a significant effect on the shape and hydrodynamic state of a deformed drop. Instead, the main effect of liquid viscosity for shock wave disturbances appeared to be reduction of the rate of deformation of the drop. This behavior allows more time for drop relaxation to the local ambient velocity, tending to reduce the relative velocity and thus the driving potential for drop deformation, at each stage of the deformation process. A simple analysis incorporating these ideas was carried out, in order to quantify the effect of liquid viscosity (represented by large Oh behavior) on deformation and breakup regime transitions.

The major assumptions of regime transition analysis were similar to earlier analysis of drop motion during breakup (Hsiang & Faeth 1992, 1993), as follows: virtual mass, Bassett history and

L.-P. HSIANG and G. M. FAETH

gravitational forces were ignored; gas velocities, and other properties, were assumed to be constant; drop mass was assumed to be constant; and a constant average drag coefficient was used over the period of interest. For present conditions, virtual mass and Bassett history forces are small because ρ_d/ρ_c is large (Faeth 1990). Similarly, gravitational forces are not a factor because drop motion was nearly horizontal and drag forces were much greater than gravitational forces. Additionally, uniform gas velocities, and other properties, were a condition of the experiments. Similarly, present considerations are limited to deformation and breakup regime transitions so that there is no mass loss of the drop. Finally, although drop drag coefficients vary considerably when drops are deformed, use of the original diameter and a constant average drag coefficient have been effective for earlier considerations of drop motion (Hsiang & Faeth 1993). Based on these assumptions, the equation governing the relative velocity, u, of the drop can be written as follows (Hsiang & Faeth 1993):

$$\mathrm{d}u/\mathrm{d}t = -3\bar{C}_D \rho_c u^2/(4\rho_d d_o) \tag{1}$$

where the initial relative velocity is equal to u_o and $\bar{C}_D$ is an appropriate average drag coefficient. Now, previous results showed that the time required for breakup, etc., of large Oh drops could not be scaled systematically in terms of the characteristic low Oh breakup time, t^*, of Ranger & Nicholls (1969). Thus, the more appropriate characteristic time for large Oh conditions defined by Hinze (1948) was used instead as follows:

$$\tau = \mu_d/(\rho_c u_o^2) \tag{2}$$

Then, it was assumed that the maximum deformation condition, or the onset of breakup condition occurs at a time $t = K\tau$, where K is an empirical constant for the process being considered. Thus, completing the integration of [1] from $t = 0$ where $u = u_o$ to $t = K\tau$ where $u = u$, yields:

$$u_o/u = 1 + K'\mu_d/(\rho_d d_o u_o) \tag{3}$$

where

$$K' = 3\bar{C}_D K/4 \tag{4}$$

Using [3], the local Weber number of the drop can be expressed as follows:

$$\rho_c u^2 d_o/\sigma = We/(1 + K'Oh(\rho_c/\rho_d)^{1/2}/We^{1/2})^2 \tag{5}$$

where $We = \rho_c u_o^2 d_o/\sigma$ is the value based on initial conditions, as before. Then it was assumed that the local Weber number must reach a particular value, We_{cr}, for the regime transition of interest to occur. Finally, solving for the initial We to achieve the required We_{cr}, yields:

$$We = (We_{cr}/4)(1 + 4K'OhWe_{cr}^{-1/2}(\rho_c/\rho_d)^{1/2}) \tag{6}$$

Values of We_{cr} and K' were fitted to [6] to yield best-fit predicted transitions for the 5–10, 10–20 and 20% deformation regime transitions as well as the first breakup regime transition (typically for bag breakup). The resulting theoretical predictions of the regime transitions are illustrated in figure 1. In view of the simplifications of the theory, the agreement between predicted and measured regime transitions is seen to be reasonably good. Notably, [6] suggests that the transition We ~ Oh at large Oh rather than an ultimate limit for particular transitions at large Oh, as suggested by Hinze (1955). This is a very important difference in behavior that has significant relevance for processes of high pressure combustion, as noted earlier; therefore, this issue clearly merits additional study. In addition, whether present predictions of regime transitions apply for Oh and We > 1000 must still be established.

3.2. Dome/bowl transition

The present drop tower experiments were designed to define the properties of the deformed drop, and did not reveal strong effects of Oh over the available test range. Thus, a deformation and breakup regime map analogous to figure 1 for shock wave disturbances was not developed for steady disturbances (although effects of We on deformation for steady disturbances will be considered subsequently). However, a transition in drop shape, from dome- to bowl-shaped drops, was explored which will be discussed in the following.
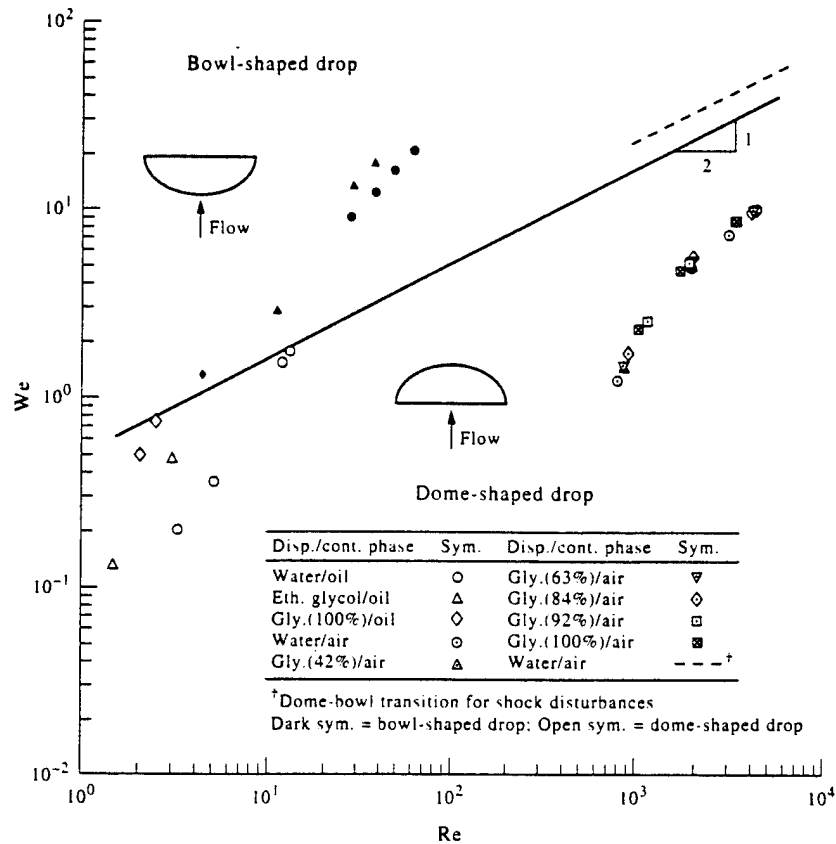
Figure 2. Dome- and bowl-shaped drop regime map.

Dome- and bowl-shaped drops are observed for both shock wave and steady disturbances. The general appearances of dome- and bowl-shaped drops are illustrated in figure 2. The windward or forward stagnation point side of a dome-shaped drop is flattened while the downstream side is rounded. This shape is similar to the appearance of a drop during bag breakup for shock wave disturbances, just at the start of the period where the bag begins to grow due to deformation of the center of the drop in a downstream direction (Hsiang & Faeth 1992). Thus, conditions for dome-shaped drops are somewhat analogous to conditions for bag breakup, and appear to involve interactions between drag and surface tension forces.

In contrast, for a bowl-shaped drop, as illustrated in figure 2, the forward stagnation region is rounded while the downstream side of the drop tends to be flattened, or even cup shaped in some instances. This shape is similar to the appearance of a drop during shear breakup for shock wave disturbances, just at the start of the period where drops are stripped from the periphery of the core (or drop forming) drop (Hsiang & Faeth 1993). Thus, conditions for bowl-shaped drops are somewhat analogous to conditions for shear breakup, and appear to involve interactions between drag and viscous forces.

The appearances of dome- and bowl-shaped drops suggest a simple means for establishing these regimes from the ratio of shear stresses to surface tension stresses. In doing this, shear stresses shall be estimated for the continuous phase, exploiting the fact that shear stresses are continuous at the drop surface, barring significant effects of surface tension gradients. Other major assumptions for these considerations are as follows: shear stresses are approximated by conditions for a laminar plane boundary layer, dispersed phase velocities are assumed to be small so that relative velocities are directly related to the velocity of the center of mass of the dispersed phase, and fluid properties are assumed to be constant. Then taking the length of the boundary layer to be proportional to the initial drop diameter, the characteristic shear stress, τ_w, becomes,

$$\tau_w = C\mu_c u_o / (\mu_c d / \rho_o u_o)^{1/2}$$

[7]

where C is a constant of proportionality. The corresponding surface tension stress is proportional to σd_o, assuming that d_o is a reasonable measure of the curvature of the drop surface. Equating these stresses then yields an expression for the transition Weber number between dome- and bowl-shaped drops, as follows:

$$We = C'Re^{1/2} \qquad [8]$$

where C' is a constant of proportionality.

The dome- to bowl-shaped drop transition expression of [8] was evaluated using available data for both steady and shock wave disturbances. The results are plotted according to the variables of [8] in figure 2. The results for steady disturbances involve both liquid–liquid and liquid–gas systems, with experimental uncertainties (95% confidence) of present Re and We determinations less than 7 and 11%, respectively. The liquid–gas systems generally involve relatively large Re and relatively small We so that these conditions are well within the dome-shaped drop regime. Thus, the transition criterion illustrated in figure 2 was found using the liquid–liquid measurements, to yield the following correlation based on [8]

$$We = 0.5\,Re^{1/2}, \text{ steady disturbances} \qquad [9]$$

Results for shock wave disturbances of drops in gases at low Oh also were considered. This transition was based on the observation that dome- and bowl-shaped drops are observed within the multimode breakup regime, near the end of the deformation period for values of We smaller and larger than roughly 40, respectively. This implies, for Oh < 0.1, the following relationship

$$We = 0.7\,Re^{1/2}, \text{ shock wave disturbances} \qquad [10]$$

which has been entered on the plot as a dashed line.

In spite of the wide range of conditions, the different kinds of disturbances, and the different density ratios, the dome- to bowl-shaped drop transition illustrated in figure 2 is reasonably consistent with [8]. Furthermore, the transition over the present test range is reasonably expressed by either [9] or [10]. Perhaps this is not surprising; in fact, a number of investigators have suggested [8] as a criterion for the onset of shear breakup, as discussed by Borisov et al. (1981). However, it should be noted that this result generally pertains to conditions where Re is substantially greater than the Stokes regime (typically Re > 10). In contrast, other criteria known for the Stokes flow regime where a somewhat similar transition (from an oblate to a prolate spheroid) has been studied for some time, see Wellek et al. (1966), and references cited therein. Thus, more work is needed to reconcile these drop shape and breakup regime transitions within the Stokes and moderate Reynolds number regimes.

3.3. Drop deformation

Earlier work for shock wave disturbances found a relatively simple relationship between drop deformation and Weber number at small Oh (Hsiang & Faeth 1992). This result was based on phenomenological analysis of the interaction between surface tension and pressure forces when a drop is drawn into a flattened (oblate spheroid) shape due to relative motion of the continuous phase. The main assumptions of this analysis were as follows: the pressure difference between the bulk of the drop liquid and the continuous phase at the periphery of the drop is assumed to be proportional to the dynamic head of the flow, $\rho_c u^2/2$; this pressure difference is assumed to be stabilized by surface tension forces acting near the drop periphery; and the volume of the drop is assumed to be preserved, e.g. $d_{min}d_{max}^2 \sim d_o^3$. These ideas yielded the following expressions for the maximum and minimum dimensions of a drop, at the condition of maximum deformation for a shock wave disturbance, when Oh is small (Hsiang & Faeth 1992):

$$d_{max}/d_o = (d_{min}/d_o)^{-1/2} = 1 + CWe^{1/2} \qquad [11]$$

where C is an empirical constant, as before. During the present investigation, drop deformation measurements were summarized as d_{max}/d_{min}. Thus, based on [11] this ratio becomes:

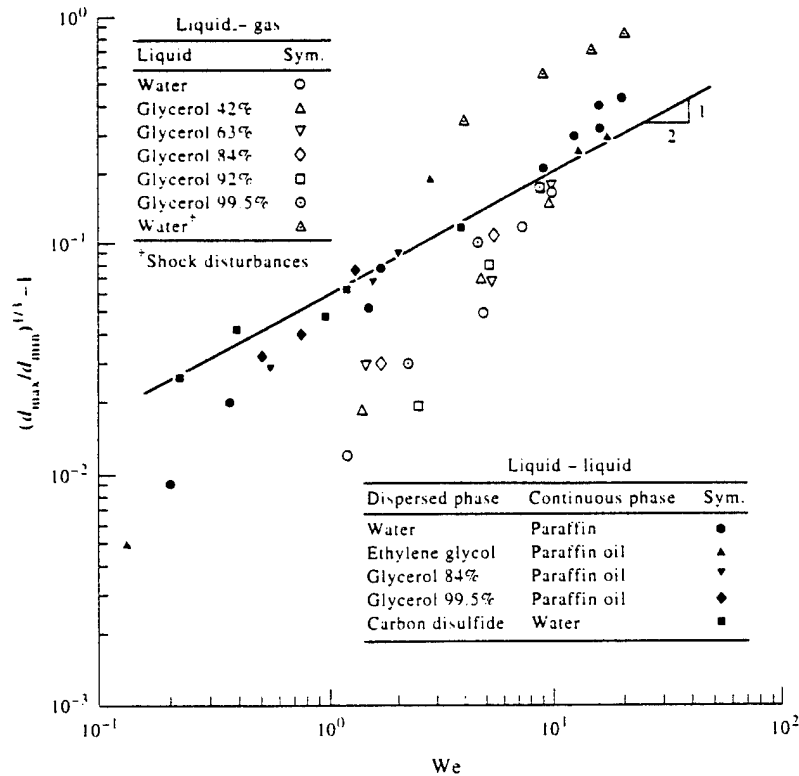$$d_{max}/d_{min} = (1 + CWe^{1/2})^3 \qquad [12]$$

Figure 3. Drop deformation as a function of Weber number.

In view of earlier findings for deformation and breakup regime transitions for shock wave disturbances, it seemed reasonable that drop deformation for steady disturbances might satisfy an expression similar to [12] for both small and large Oh. In particular, the main effect of Oh for shock wave disturbances was to slow the rate of drop deformation so that local We at particular levels of deformation were reduced, rather than to modify the nature of the deformation at a particular local We condition. Thus, since drops have unlimited time to accommodate to a steady disturbance, it seems reasonable that the effect of Oh on deformation might be much reduced, as well.

Drop deformations for steady disturbances are plotted as suggested by [12] in figure 3. Results illustrated in the figure include drops at their terminal velocities in both gases and liquids. The experimental uncertainties (95% confidence) of the dependent variable is relatively large because the diameter ratio is near unity, e.g. on the order of 30 and 100% at values of the dependent variable of 0.1 and 0.03, respectively; the corresponding uncertainties of We are less than 11%. A representative result for water drops subjected to shock wave disturbances in air also is illustrated on the plot, where these results pertain to the maximum state of deformation of the drop during the period of interaction between the drop and the gas. A best-fit correlation of the steady disturbance measurements, according to [12] also is shown on the plot, as follows:

$$d_{max}/d_{min} = (1 + 0.07\,We^{1\,2})^3 \tag{13}$$

The measurements illustrated in figure 3 only are in fair agreement with the correlation of [13]. First of all, d_{max}/d_{min} for liquid–liquid systems are consistently larger than gas–liquid systems at a particular We. This behavior could be due to the effect of motion within the dispersed phase, which represents a larger fraction of the velocity difference between the dispersed and continuous phases for liquid–liquid than gas–liquid systems. In addition, significant circulatory motion within the dispersed phase would be expected to increase d_{max} due to centrifugal forces, as seen in the measurements of figure 3. Another deficiency of [13] is that the measurements decrease more rapidly as We decreases than is suggested by the correlation even though behavior at large We is represented reasonably well. This deficiency, however, is less significant because the discrepancies between the measurements and the correlation in this region are relatively small in comparison to
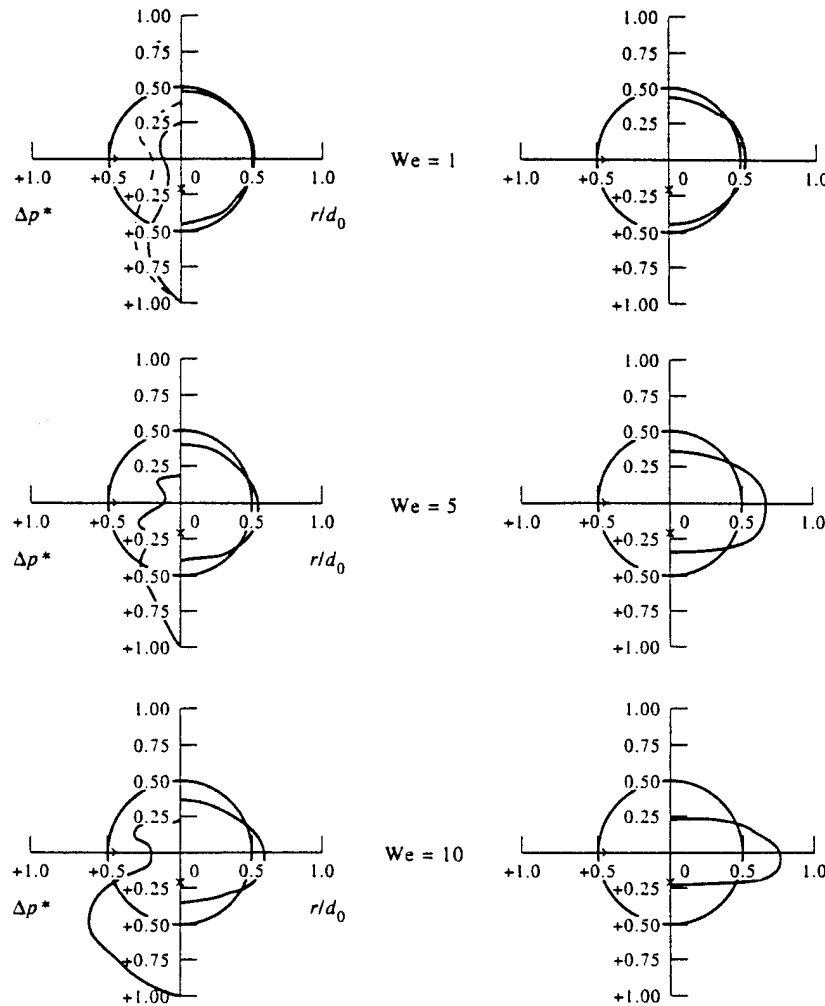
Figure 4. Drop shape and pressure distribution for steady (left-hand column) and shock wave (right-hand column) disturbances.

experimental uncertainties. Thus, [13] is provisional at best, pending more detailed measurements. Nevertheless, the measurements illustrated in figure 3 indicate that deformation mainly depends on We with density ratio, Oh and Re being secondary factors over the range of present measurements.

Comparing results for shock wave and steady disturbances in figure 3 shows that the maximum deformations for shock wave disturbances are greater than for steady disturbances at comparable conditions. This behavior is caused by inertial phenomena analogous to oscillatory deformation discussed in connection with figure 1. Thus, inertial effects cause the drop deformation to overshoot levels pertinent to steady disturbances at the same We.

The nature of overshoot effects on drop deformation is illustrated more thoroughly in figure 4. In this figure, drop shapes are plotted for We = 1, 5 and 10 for both steady (left hand column) and shock wave (right hand column) disturbances. As before, the shock wave disturbances pertain to the condition of maximum deformation of the drop for the indicated We. Additionally both sets of measurements are for liquid drops in gases. Finally, all the results illustrated in figure 4 are for We lower than required for the onset of secondary breakup, and are within the dome-shaped drop regime. The effect of overshoot is quite evident for the shock wave disturbances, which exhibit substantially larger maximum deformations than the steady disturbances at each value of We. Finally, the progressive increase of deformation with increasing We is very evident. This increased deformation provides a substantial increase of the drag forces acting on the drop due to the increased cross sectional area of the drop alone; furthermore, subsequent considerations will show

that drag coefficients are increased by deformation as well. Thus, drop deformation near the conditions for the onset of secondary breakup have a significant effect on drop dynamics.

3.4. Drop drag

The drop shape results for steady disturbances illustrated in figure 4 were used to obtain some insight about drop drag properties. This was done by estimating the static pressure, p, distribution around the drop, allowing for both hydrostatic and surface tension forces. The major assumptions of these calculations were as follows: effects of liquid motion within the drop were neglected, drops were assumed to be axisymmetric, effects of surface tension gradients were ignored and the hydrostatic pressure variation in the gas phase was neglected. The resulting static pressure estimates are plotted in figure 4 in terms of an effective pressure coefficient, defined as follows:

$$\Delta p^* = (1 + (p - p_x)/(\rho_c u_0^2/2))/2 \tag{14}$$

where p_x is the static pressure far from the drop. The corresponding variation of Δp^* for flow over a solid sphere for a comparable Re range found from White (1974), also is illustrated in the figure for reference purposes (the dashed line illustrated for We = 1).

There are several interesting features about the static pressure distributions plotted in figure 4 for steady disturbances. First of all, Δp^* is unity at the forward stagnation point by definition. Secondly, static pressures decrease with increased angle from the forward stagnation point and tend to reach a minimum slightly before or near the 90° condition. Static pressures in the wake, however, do not recover to levels near the forward stagnation point because Re > 10 and the flow is separated in the wake region. This implies that 80–95% of the drag is due to form drag, caused by the static pressure distribution around the drop. Additionally, the increased drop deformation as We increases tends to increase the extent of the region of high static pressures near the forward stagnation point, which causes corresponding increases of the drag coefficient with deformation that will be discussed subsequently. Thus, while shear forces affect the mechanism of breakup of
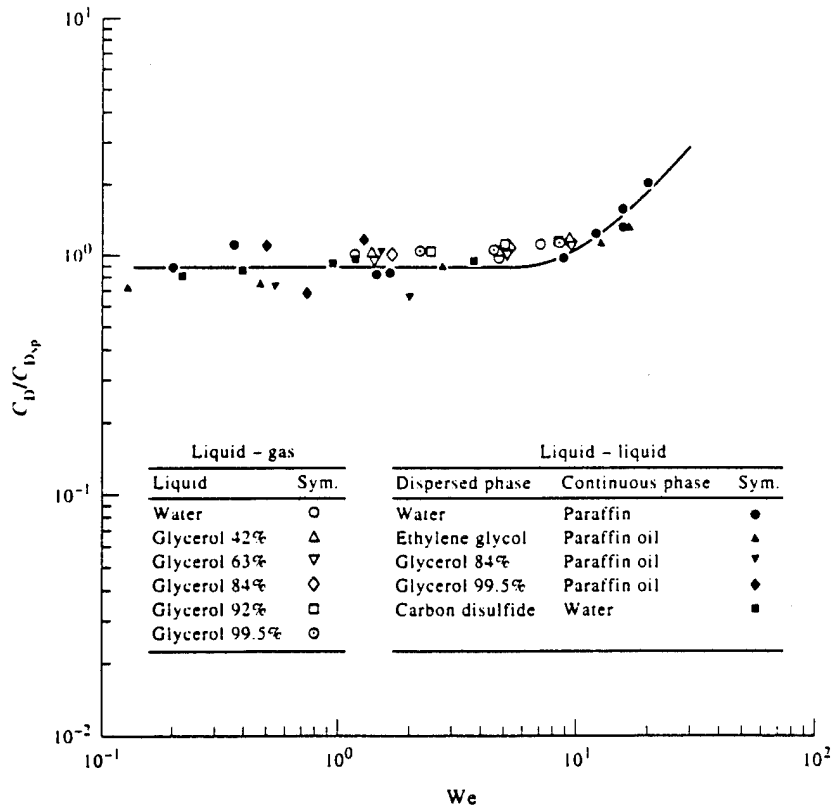

Figure 5. Drop drag coefficient as a function of deformation for steady disturbances.

the drop. as well as the transition between dome- and bowl-shaped drops. they really do not play a major role in the development of drop drag properties.

Drop drag coefficients. C_D. were defined in the usual manner. based on the maximum cross stream dimension of the drop and the relative velocity between the drop and continuous phases. The resulting drag coefficients for steady disturbances are plotted in figure 5. These results are plotted as $C_D/C_{D_{sp}}$. where $C_{D_{sp}}$ is the drag coefficient of a sphere at the same Re. as a function of We. The experimental uncertainties (95% confidence) of the drag ratio are less than 10% while those for We are less than 11%. The values of We range from 0.1 to roughly 20. with the latter corresponding to maximum values of We without secondary breakup for steady disturbances. The measurements include results for drops in both gases and liquids.

Even though drops in gases exhibit a somewhat smaller deformation than drops in liquids at the same We. see figure 3. the results illustrated in figure 5 show that they generally have somewhat larger drag coefficients. In fact. drops in liquids have somewhat smaller drag coefficients than solid spheres for We < 4. This effect probably is due to motion of the drop liquid which is a larger fraction of the relative velocity for drops in liquids than drops in gases. e.g. the characteristic velocity for the drop phase is $(\rho_c/\rho_d)^{1/2} u$. Nevertheless. this reduction of the drag coefficient is not major in comparison to experimental uncertainties. e.g. $C_D/C_{D_{sp}}$ is roughly 0.9 and 1.0 for We < 4 for drops in liquids and gases. respectively. Thus. it does not appear that density ratio has a significant effect on the drag coefficient for drops.

Considering all available data for the drag coefficients of drops in gases and liquids, and for shock wave and steady disturbances. it appears that C_D largely is a function of degree of deformation of the drop. This behavior is illustrated in figure 6. where present measurements of C_D for steady disturbances. and those of Hsiang & Faeth (1992) for shock wave disturbances. are plotted as a function d_{max}/d_{min}. The experimental uncertainties (95% confidence) of C_D for the steady disturbances are less than 10% while those for the shock wave disturbances are less than 30%. The corresponding uncertainties of the diameter ratio for steady and shock wave disturbances are less than 14 and 7%. respectively. It is evident that the results yield a single correlation with the main difference between the steady and shock wave disturbances being the larger range of d_{max}/d_{min} available prior to the onset of breakup for the latter. The range of the measurements is
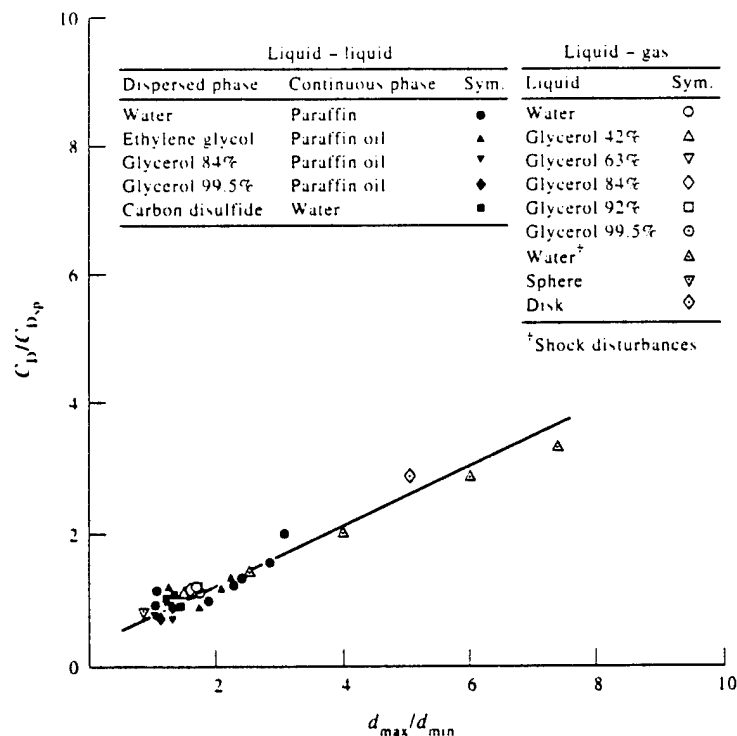

Figure 6. Drop drag coefficient as a function of deformation for both shock wave and steady disturbances.

C_D/C_{Dsp} of 1.0–3.5 for d_{max}/d_{min} of 1.0–7.5. Thus there is roughly a 3:1 increase of drag coefficient in going from a round drop to a highly deformed and flattened drop, which is reasonable because the change is comparable to the change of C_D between a round sphere and a thin disk (White 1974). This behavior, combined with the increased cross-sectional area of the drop, causes a substantial increase in the drag forces acting on deformed drops in comparison to the original undeformed drop. For example, the ratio of the drag forces is $(d_{max}/d_o)^2(C_D/C_{Dsp})$ which becomes $(d_{max}/d_{min})^2(C_D/C_{Dsp})$ from [11] and [12]. Applying this equation to the results illustrated in figure 6 then yields deformed non-deformed drag force ratios of roughly 4 and 13 for drops having maximum deformations for steady and shock wave disturbances, respectively.

4. CONCLUSIONS

Drop deformation and breakup for both shock wave and steady disturbances were studied. Several liquids were considered for the dispersed (drop) phase, including water, n-heptane, mercury, Dow Corning 200 Fluids, various glycerol mixtures, ethylene glycol and carbon disulfide. Continuous phases included air, paraffin oil and water. Overall test conditions involved ρ_d/ρ_c of 1.15–12,000, Oh of 0.0005–600, We of 0.004–700 and of 0.03–16,000. The major conclusions of the study are as follows:

(1) For shock wave disturbances at small Oh (Oh < 0.1), significant drop deformation (5–10% deformation regime) was observed at We of roughly 0.6 while bag, multimode and shear breakup began at We = 13, 35 and 80, respectively.

(2) For shock wave disturbances at large Oh (Oh > 1) the critical We for the onset of various deformation and breakup regimes became roughly proportional to Oh, which could be attributed to increased resistance of drops to deformation at large Oh, based on phenomenological analysis (note that behavior for Oh and We > 1000 still must be studied, however). In addition, the oscillatory deformation and the bag breakup regimes disappeared with increasing Oh, at Oh = 0.3 and 4, respectively.

(3) An important transition from dome- to bowl-shaped drops (which is related to the transition between bag and shear breakup) appears to be controlled by $We/Re^{1/2}$ for the present Re range, but other criteria known for analogous transitions in the Stokes flow regimes must still be reconciled with this behavior.

(4) Drop deformation for steady disturbances mainly varied with We, while minor effects of ρ_d/ρ_c on deformation mainly were attributed to corresponding variations of Re. Thus, the main effect of increased drop viscosity (represented by Oh) on drop deformation and breakup for general disturbances is to reduce rates of drop distortion so that drop relaxation reduces relative velocities when the maximum deformation is reached, and thus the propensity for drop deformation and breakup.

(5) Drop drag coefficient ratios, C_D/C_{Dsp}, were relatively independent of the type of disturbance, ρ_d/ρ_c, We, Oh and Re; instead, these ratios correlated mainly with drop deformation, while evolving from values near unity for small distortions to values typical of thin disks for large distortions. This increase in C_D and the corresponding increase of the cross-sectional area of the drop, due to distortion, causes drag forces to increase by factors of roughly 4 and 13 at deformation conditions typical of the onset of breakup for steady and shock wave disturbances, respectively, which clearly has an important impact on breakup dynamics.

REFERENCES

Borisov, A. A., Gel'fand, B. E., Natanzon, M. S. & Kossov, O. M. 1981 Droplet breakup regimes and criteria for their existence. *Inzh.-Fizich. Zl* **40**, 64–70.

Clift, R. Grace, J. R. & Weber, M. E. 1978 *Bubbles, Drops and Particles*, pp. 26 and 339–347. Academic Press, New York.

Dabora, E. K. 1967 Production of monodisperse sprays. *Rev. Scient. Instrum.* **38**, 502–506.

Faeth, G. M. 1990 Structure and atomization properties of dense turbulent sprays. In *Twenty-Third Symposium (International) on Combustion*, The Combustion Institute, Pittsburgh, pp. 1345–1352.

Gel'fand, B. E., Gubin, S. A. & Kogarko, S. M. 1974 Various forms of drop fractionation in shock waves and their special characteristics. *Inzh.-Fizich. Zl* **27**, 119–126.

Giffen, E. & Muraszew, A. 1953 *The Atomization of Liquid Fuels*. Wiley, New York.

Hanson, A. R., Domich, E. G. & Adams, H. S. 1963 Shock-tube investigation of the breakup of drops by air blasts. *Phys. Fluids* **6**, 1070–1080.

Hinze, J. O. 1948 Critical speeds and sizes of liquid globules. *Appl. Sci. Res.* **11**, 273–287.

Hinze, J. O. 1955 Fundamentals of the hydrodynamic mechanism of splitting in dispersion processes. *AIChE Jl* **1**, 289–295.

Hsiang, L.-P. & Faeth, G. M. 1992 Near-limit drop deformation and secondary breakup. *Int. J. Multiphase Flow* **18**, 635–652.

Hsiang, L.-P. & Faeth, G. M. 1993 Drop properties after secondary breakup. *Int. J. Multiphase Flow* **19**, 721–735.

Krzeczkowski, S. A. 1980 Measurement of liquid droplet disintegration mechanisms. *Int. J. Multiphase Flow* **6**, 227–239.

Lane, W. R. 1951 Shatter of drops in streams of air. *Ind. Engng Chem.* **43**, 1312–1317.

Lange, N. A. 1952 *Handbook of Chemistry*, 8th edn, pp. 1134 and 1709. Handbook Publishers Inc., Sandusky, OH.

Liang, P. Y., Eastes, T. W. & Gharakhari, A. 1988 Computer simulations of drop deformation and drop breakup. AIAA Paper No. 88-3142.

Loparev, V. P. 1975 Experimental investigation of the atomization of drops of liquid under conditions of a gradual rise of the external forces. *Izvestiya Akad. Nauk SSSR, Mekh. Zhidkosti Gaza* **3**, 174–178.

Pruppacher, H. R. & Pitter, R. L. 1971 A semi-empirical determination of the shape of cloud and rain drops. *J. Atmos. Sci.* **28**, 86–94.

Ranger, A. A. & Nicholls, J. A. 1969 The aerodynamic shattering of liquid drops. *AIAA Jl* **7**, 285–290.

Reinecke, W. G. & McKay, W. L. 1969 Experiments on waterdrop breakup behind Mach 3 to 12 shocks. Sandia Corp. Report SC-CR-70-6063.

Reinecke, W. G. & Waldman, G. D. 1970 A study of drop breakup behind strong shocks with applications to flight. Avco Report AVSD-0110-70-77.

Ruff, G. A., Wu, P.-K., Bernal, L. P. & Faeth, G. M. 1992 Continuous- and dispersed-phase structure of dense non-evaporating pressure-atomized sprays. *J. Prop. Power* **8**, 280–289.

Ryan, R. T. 1976 The behavior of large low-surface-tension water drops falling at terminal velocity in air. *J. Appl. Meteorol.* **15**, 157–165.

Sangiovanni, J. & Kestin, A. S. 1977 A theoretical and experimental investigation of the ignition of fuel droplets. *Combust. Sci. Technol.* **6**, 59–70.

Simmons H. C. 1977 The correlation of drop-size distributions in fuel nozzle sprays. *J. Engng Power* **99**, 309–319.

Wellek, R. M., Agrawal, A. K. & Skelland, A. H. P. 1966 Shape of liquid drops moving in liquid media. *AIChE Jl* **12**, 854–862.

White, F. M. 1974 *Viscous Fluid Flow*. McGraw-Hill, New York.

Wierzba, A. & Takayama, K. 1987 Experimental investigations on liquid droplet breakup in a gas stream. Rep. Inst. High Speed Mech., Tohoku Univ., Vol. 53, No. 382, pp. 1–99.

Wu, P.-K., Ruff, G. A. & Faeth, G. M. 1991 Primary breakup in liquid/gas mixing layers. *Atom. Sprays* **1**, 421–440.

Wu, P.-K., Tseng, L.-K. & Faeth, G. M. 1992 Primary breakup in gas/liquid mixing layers for turbulent liquids. *Atom. Sprays* **2**, 295–317.

Appendix C: Chou, W.-H., Hsiang, L.-P. and Faeth, G.M. (1995) Temporal variation of drop properties and formation rates during secondary breakup. AIAA Paper No. 95-2426.

⟳AIAA

AIAA 95-2426
Temporal Variation of Drop Properties and Formation Rates During Secondary Breakup

W.-H. Chou, L.-P. Hsiang and G. M. Faeth
Department of Aerospace Engineering
The University of Michigan
Ann Arbor, MI

31st AIAA/ASME/SAE/ASEE
Joint Propulsion Conference and Exhibit
July 10-12, 1995/San Diego, CA

TEMPORAL VARIATION OF DROP PROPERTIES
AND FORMATION RATES DURING SECONDARY BREAKUP

by

W.-H. Chou,[*] L.-P. Hsiang[†] and G.M. Faeth[**]
Department of Aerospace Engineering
The University of Michigan
Ann Arbor, MI 48109-2118, U.S.A.

Abstract

The properties of drops produced by secondary breakup in the shear breakup regime were measured as a function of time for shock-wave-initiated disturbances in air at normal temperature and pressure. The test liquids included water, ethyl alcohol and various glycerol mixtures to yield Weber numbers of 125-375, Ohnesorge numbers of 0.0034-0.039, liquid/gas density ratios of 678-984 and Reynolds numbers of 3070-11150. Measurements involved double-pulse holography to yield drop sizes and velocities at various times during the breakup process. The size distributions of drops produced by secondary breakup satisfied Simmons' universal root normal distribution function at each instant of time. The Sauter mean diameters of the drops produced by secondary breakup were successfully correlated by a phenomenological analysis which implied that drop sizes were related to the thickness of the liquid boundary layer formed by the action of drag on the upstream surface of the parent drop. The velocity distribution functions of drops produced by secondary breakup were uniform, with mean drop velocities nearly equal to the mean velocities of the parent drop at each instant of time, and rms drop velocity fluctuations on the order of 10% of the mean relative streamwise velocity between the gas and the parent drop. Phenomenological analysis, that combined the results for drop size and velocity distributions, yielded a successful correlation for the degree of mass removal from the parent drop as a function of time during breakup. Finally, integrating drop size, velocity and formation rate properties over the period of breakup showed that the spray-containing region at the end of breakup extended over a region having a streamwise distance of roughly 40-100 initial drop diameters, which implies that secondary breakup should be treated as a rate process, rather than by jump conditions, in some instances.

Nomenclature

C_b	=	empirical constant
C_c	=	empirical constant
C_D	=	drop drag coefficient
$\overline{C}_D$	=	mean drop drag coefficient over breakup period
C_e	=	empirical constant
C_s	=	empirical constant
d	=	drop diameter
d_{max}, d_{min}	=	maximum and minimum dimensions of a drop
MMD	=	mass median drop diameter
Oh	=	Ohnesorge number, $\mu_f / (\rho_f d \sigma)^{1/2}$
Re	=	Reynolds number, ud/ν_g
Re_{fo}	=	drop liquid Reynolds number, $(\rho_g/\rho_f)^{1/2} u_o d_o / \nu_f$
SMD	=	Sauter mean diameter
t	=	time
t^*	=	characteristic breakup time, $d_o(\rho_f / \rho_g)^{1/2}/u_o$
t_c	=	characteristic time for liquid motion transition
u	=	streamwise velocity
v	=	cross-stream velocity
$\overline{v'}$	=	rms cross-stream velocity fluctuation
$\overline{v}$	=	mean cross-stream velocity
We	=	Weber number, $\rho_g d u^2/\sigma$
δ	=	thickness of boundary layer within parent drop
δ_c	=	critical boundary layer thickness for steady-state breakup
μ	=	molecular viscosity
ν	=	kinematic viscosity

---

[*] Graduate Student Research Assistant.

[†] Post-Doctoral Research Fellow.

[**] Professor, Fellow AIAA

ρ   =   density
σ   =   surface tension
Subscripts
e   =   property at end of breakup
f   =   liquid-phase property
g   =   gas-phase property
p   =   parent drop property
o   =   property at the start of breakup

Introduction

The secondary breakup of drops is an important fundamental process of sprays. In particular, drops formed by primary breakup are intrinsically unstable to secondary breakup, while secondary breakup can be the rate controlling process within dense sprays in much the same way that drop vaporization can be the rate controlling process within dilute sprays.[1,2] Motivated by these observations, the objective of the present investigation was to extend earlier studies of the regimes and outcomes of secondary drop breakup due to shock-wave disturbances,[3-5] to consider the evolution of both the properties and rate of formation of drops resulting from secondary breakup as a function of time during shear breakup processes.

Earlier studies of secondary breakup are discussed by Wu et al.,[1] Faeth,[2] Giffen and Muraszew,[6] Hinze,[7] Clift et al.,[8] Krzeczkowski[9] and Wierzba and Takayama,[10] among others. Shock-wave disturbances were considered during most earlier studies, providing a step change of the ambient environment of a drop, similar to conditions experienced by drops at the end of primary breakup. The main findings of this work included the conditions required for particular deformation and breakup regimes, the times required for the onset and end of breakup, the drag properties of deformed drops, and the drop size and velocity distributions at the end of the breakup process (i.e., the jump conditions). An interesting feature of these results is that secondary breakup extended over appreciable regions of time and space and was not properly described by jump conditions in some instances. For example, Liang et al.[11] show that breakup times are 5.5 t* (where t* is defined by Ranger and Nicholls[12] as a characteristic secondary breakup time for shear breakup) for a wide range of drop conditions, which is comparable to flow residence times within the dense spray region where secondary breakup is a dominant process.[1,2] Viewed another way, the original (or parent) drop moves roughly 40 initial drop diameters while the smallest drops formed by secondary breakup move up to 100 initial drop diameters during the period of breakup within the shear breakup regime.[4,5] Such distances can represent a significant fraction of the length of the dense spray region. These observations suggest that the time-resolved features of secondary breakup eventually must be understood, i.e., the size and velocity distributions of the drops, and the rate at which liquid is removed from the parent drop, must be known as a function of time during secondary breakup. The present study seeks to provide a portion of this information by carrying out new measurements within the shear breakup regime, where secondary breakup proceeds by stripping drop liquid from the periphery of the parent drop. Phenomenological theories also were developed, in order to help interpret and correlate the measurements.

The present measurements were carried out using a shock tube facility, with the environment of the test drops during breakup roughly approximating air at normal temperature and pressure. Properties during breakup were observed using double-pulse holography in order to find both the size and velocity properties of drops produced by secondary breakup, as well as liquid removal rates from the parent drop, as a function of time. Test conditions were limited to relatively large liquid/gas density ratios ($\rho_f / \rho_g > 500$), in order to minimize potential complications due to the inertia of the continuous phase, and relatively small initial Ohnesorge numbers ($Oh_0 < 0.1$), in order to minimize potential complications due to effects of liquid viscosity. As a result, the present test conditions are most representative of secondary breakup within sprays near atmospheric pressure. The experiments also were confined to the shear breakup regime. For present ranges of ρ_f / ρ_g and Oh_0, this implies $We_0 > 90$ in order to exceed the multimode/shear breakup regime transition and $We_0 < 1000$ in order not to exceed the shear/drop-piercing (or shear/catastrophic) breakup regime transition.[6,13,14] Drop liquids included water, ethyl alcohol and various glycerol mixtures in order to provide information about effects of drop liquid properties.

The paper begins with a description of experimental methods. Results are then discussed, considering drop size properties, drop velocity properties, drop formation rates and the extent of the drop-containing region, in turn.

Experimental Methods

Apparatus

The test apparatus will only be described briefly because it was similar to earlier work.[3-5] A shock tube with the driven section open to the atmosphere was used for the measurements, similar to the arrangement used by Ranger and Nicholls.[12] The driven section had a rectangular cross section (38 mm wide and 64 mm high) and a length of 6.7 m, with the

test location 4.0 m from its downstream end. This configuration provided test times of 17-21 ms in the uniform flow region behind the incident shock wave.

The test location had quartz windows (25 mm high and 305 mm long, mounted flush with the interior of the side walls) to allow observations of drop breakup. A vibrating capillary tube drop generator, similar to the arrangement described by Dabora,[15] was used to generate a stream of drops having a constant diameter. This drop stream passed through 6 mm diameter holes in the top and bottom of the driven section of the shock tube, crossing the central plane of the driven section at the test location. Test drops had diameters of roughly 1 mm, while the spacing between drops was 3-4 mm; therefore, drops always were present within the region observed while interactions between adjacent drops during shear breakup were negligible.

Instrumentation

Double-pulsed holography was used to measure the properties of the parent drop, and the size and velocity distribution functions of drops produced by secondary breakup, as a function of time during breakup. The holocamera system involved two frequency doubled YAG lasers (Spectra Physics Model GCR-130, 532 nm wavelength, 7 ns pulse duration, up to 200 mJ per pulse) which could be controlled to provide pulse separations as small as 100 ns. An off-axis holocamera arrangement was used with the optics providing a 25 mm diameter field of view at the test drop location and a 3:1 primary magnification of the hologram image. The laser pulse times were sufficiently short to stop the motion of the drops on the film. Reconstruction of the double-pulse holograms yielded two images of the spray so that drop velocities could be found given the time of separation between pulses (which was measured with a digital oscilloscope). The second laser pulse was somewhat weaker than the first, which allowed directional ambiguity to be resolved because stronger pulses yield sharper reconstructed images.

The hologram reconstruction system also was modified from the arrangement used by Hsiang and Faeth.[3-5] A helium-neon laser (Spectra Physics Model 124B, cw laser, 35 mW of optical power) was used to reconstruct the image. The reconstructed image was observed using a CCD camera (SONY, Model XC-77) with optics to yield a magnification of 300:1 and a field of view of the image (on the monitor) of 1.2 × 1.4 mm. The optical data was obtained using a frame grabber (Data Translation DT 2851) and stored on personal computer (Micron, Pentium 90). The images were processed using Media Cybernetics Image-Pro Plus software. Various locations in the hologram

reconstruction were observed by traversing the hologram in two directions, and the video camera of the image display in the third direction. Positions were selected for viewing using stepping motor driven linear traversing systems (Velmex, Model VP9000) having 1 μm positioning accuracies. The combined holocamera/reconstruction system allowed objects as small as 3 μm to be observed and objects as small as 5 μm to be measured with 5% accuracy.

Drop sizes and velocities were measured in the same manner as Hsiang and Faeth.[3-5] The diameters of mildly irregular objects were found by measuring their maximum and minimum diameters, d_{max} and d_{min}, through the centroid of the image. Then assuming that the drop had an ellipsoidal shape, the drop diameter was taken to be equal to the diameter of a sphere having the same volume as the ellipsoid, e.g., $d^3 = d_{min}^2 d_{max}$. More irregular objects were sized by finding the cross-sectional area and perimeter of the image and proceeding as before for an ellipsoid having the same properties. The velocity of each drop was found by measuring the distance between the centroid of its two images on a double-pulse hologram and dividing by the known time between laser pulses. Results at each condition were summed over at least four realizations, considering 100-200 liquid elements, in order to provide drop diameter and velocity correlations. Experimental uncertainties caused by the present definition of drop diameters are difficult to quantify, however, they are felt to be small in comparison to the accuracy of the size and distance measurements and sampling limitations. Estimated experimental uncertainties (95% confidence) based on the latter effects are less than 10% for drop diameters and less than 15% for streamwise drop velocities.

Test Conditions

The test conditions are summarized in Table 1. Test drops of water, ethyl alcohol and various glycerol mixtures were used to provide a reasonably wide range of liquid properties within the low Ohnesorge regime. The liquid properties were obtained from Lange,[16] except for the surface tension of the glycerol mixtures which was measured in the same manner as Wu et al.[17] Initial drop diameters were in the range 0.78-1.00 mm. The ranges of other variables were as follows: ρ_f / ρ_g = 678-984, Oh_0 = 0.0034-0.039, Re_0 = 3070-11150 and We_0 = 125-375. The We_0 range, 125-375, is limited to the shear breakup regime which begins at the transition from the multimode breakup regime at We_0 = 80,[3] and ends at the onset of the drop-piercing (or catastrophic) breakup regime at We_0 of 1000-10000,[13,14] for Oh_0 < 0.1. The Re_0 range of the present experiments is higher than conditions where gas

viscosity has a significant effect of drop drag properties, e.g. C_D for spheres only varies in the range 0.4-0.5 for this Reynolds number range.[18] Shock Mach numbers were relatively low, less than 1.3; therefore, the physical properties of the gas in the uniform flow region behind the shock wave were nearly the same as room air.

Results and Discussion

Drop Sizes

Drop Size Distribution. The evolution of drop size distributions during secondary breakup was considered first because this affects the information needed to characterize secondary breakup properties. The main issue was to determine whether drop sizes varied appreciably from the universal root normal distribution with MMD/SMD = 1.2, proposed by Simmons,[19] which was found to be satisfactory for a variety of primary[1,2] and secondary[3-5] drop breakup processes. This behavior vastly simplifies the presentation of data because the root normal distribution only has two moments (see Belz[20] for a discussion of the properties of the root normal distribution function); therefore, with the MMD/SMD equal to a constant, the drop size distribution is entirely specified by the SMD alone.

Typical results from the drop size distribution measurements are illustrated in Fig. 1. These measurements involve various liquids, We_o and times during the breakup process. The times have been normalized by t^*, the characteristic shear breakup time discussed earlier. It should be recalled, that drop breakup is only observed for t/t^* in the range 1.5-5.5 for a wide range of shear breakup conditions;[3-5] therefore, the present data are limited accordingly.

The number of drops available to define the drop size distribution for each breakup condition and t/t^* is limited, which accounts for the significant scatter of drop size distribution properties seen in Fig. 1. Nevertheless, within the scatter of the data, drop sizes produced by secondary breakup are represented reasonably well by the universal root normal size distribution function with MMD/SMD = 1.2. This result is plausible because primary and secondary breakup processes, as well as drops at various positions within dense sprays, generally satisfy the root normal size distribution function.[1-5] In fact, the main exception observed thus far involves distortion of the size distribution function at the end of shear breakup when the parent drop is included in the distribution,[4] which clearly is not a factor here. As a result, the SMD is sufficient to characterize the entire drop size distribution and will be used for this purpose in the following discussion of secondary breakup properties.

Transient/Steady-State Breakup Transition. A correlating expression for the SMD as a function of time during secondary breakup in the shear breakup regime was sought using methods similar to Hsiang and Faeth[3] and Wu et al.[17] This involved noting that drops or ligaments are stripped from the liquid-phase boundary layer that forms on the upstream (windward) side of the drop during secondary breakup in the shear breakup regime. In particular, earlier work suggested that drop sizes after secondary breakup mainly are dependent upon the viscosity, rather than the surface tension, of the liquid-phase.[3] In addition, initial measurements during the present investigation supported a strong effect of liquid viscosity on the variation of drop sizes produced by secondary breakup as a function of time during secondary breakup processes. In particular, two basic types of behavior were observed, as follows: (1) a regime where there was a progressive increase of the SMD of drops formed as a function of time during breakup, which was mainly seen when the liquid viscosity was small; and (2) a regime where the SMD of drops formed was relatively independent of time, which was mainly seen when the liquid viscosity was large (although it should be recalled that present test conditions always involved small Ohnesorge numbers where variations of liquid viscosity do not affect the criteria for the onset of breakup). Both behaviors suggest effects of vorticity within the drop; therefore, phenomenological analyses to find drop sizes were based on the configurations appearing in Figs. 2 and 3. Both figures are sketches of the parent drop after the deformation period, when drops are being formed from the periphery of the parent drop. It is assumed that drops are formed from the vortical region in the liquid, or the liquid boundary layer, that develops on the upstream side of the drop; and that this layer is laminar with SMD ~ δ, similar to earlier considerations of drop sizes after secondary breakup due to Hsiang and Faeth.[3] Then the two types of behavior represent different states of transient development of the vortical region. For small liquid viscosity, Fig. 2, the rate of temporal development of the liquid boundary layer is slow so that $\delta(t) \sim (\nu_f t)^{1/2}$ as discussed by Schlichting.[21] On the other hand, for large liquid viscosity, Fig. 3, the rate of development of the liquid boundary layer is rapid so that the liquid boundary layer reaches its steady state boundary layer thickness, as discussed by Hsiang and Faeth.[3] The transition between these two regimes can be found as the time, t_c, required for the vorticity to propagate to some fraction of the initial drop diameter, or $\delta_c \sim (\nu_f t_c)^{1/2} \sim d_o$. This expression can be conveniently rewritten, as follows:

$$t_c/t^* = C_c(\rho_g/\rho_f)^{1/2} u_o d_o/\nu_f = C_c Re_{fo} \qquad (1)$$

where C_c is an empirical factor on the order of unity. Then when $t_c/t^* \gg 1$, the transient growth of the boundry layer thickness determines the drop sizes produced by breakup, as illustrated in Fig. 2; in contrast, when $t_c/t^* \ll 1$, the drop diameter restricts the boundary layer thickness, and thus the drop sizes produced by breakup, as illustrated in Fig. 3.

Transient Breakup Regime. Phenomenological analysis of the transient growth regime ($t_c/t^* \gg 1$), illustrated in Fig. 2; then proceeds by assuming a laminar boundary layer in the liquid and $SMD(t) \sim \delta(t)$, similar to the earlier considerations of drop sizes after secondary breakup due to Hsiang and Faeth.[3] This implies:

$$SMD(t) = C_S (\nu_f t)^{1/2}, \quad t_c/t^* \gg 1 \qquad (2)$$

where C_S is an empirical constant on the order of unity. Then, normalizing time by the characteristic secondary breakup time, t^*, an expression for $SMD(t)$ is obtained, as follows:

$$SMD(t)/(\nu_f t^*)^{1/2} = C_S(t/t^*)^{1/2}, \quad t_c/t^* \gg 1 \qquad (3)$$

Present measurements of $SMD(t)$, for drops having a relatively small liquid viscosity, are correlated according to Eq. (3) in the upper plot of Fig. 4. These results include all test conditions considered during the present investigation, except for glycerol 63% which involved relatively large liquid viscosities, although it should be recalled that the available time range is somewhat limited because drops are only formed during the normalized time period, t/t^* of 1.5-5.5.[11] The theoretical correlation shown on the plot is a least-squares fit based on Eq. (3), as follows:

$$SMD(t)/(\nu_f t^*)^{1/2} = 1.8 \, (t/t^*)^{1/2}, \quad t_c/t^* \gg 1 \qquad (4)$$

The standard deviation of the coefficient on the right hand side of Eq. 4 is 15%, with the correlation coefficient of the fit being 0.91, which is reasonably good. If the power on the RHS of Eq. (4) is found from a least-squares fit, a value of 0.6 with a standard deviation of 0.16 is obtained, which is not statistically different from the power based on theory used in Eq. (4).

The consistency of Eq. (4) with the earlier measurements of Hsiang and Faeth[3] of the SMD at the end of shear breakup, for low viscosity liquids, was also examined. In particular, assuming that drop sizes at the end of breakup are dominated by the largest drop sizes, which also are generated at the end of breakup, there results from Eq. (3):

$$SMD_e/(\nu_f t^*)^{1/2} = C_e C_S(t_c/t^*)^{1/2}, \quad t_c/t^* \gg 1 \qquad (5)$$

where C_e is an empirical factor on the order of unity. Then introducing t^* and rearranging yields:

$$SMD_e/d_o = C_e C_S(t_e/t^*)^{1/2}(\rho_f / \rho_g)^{1/4}(d_o u_o/\nu_f)^{1/2}, \quad t_c/t^* \gg 1 \qquad (6)$$

which is identical to the findings of Hsiang and Faeth[3] if $C_e C_S(t_e/t^*)^{1/2} = 6.2$. Recalling that $C_S = 1.8$ and $t_e/t^* = 5.5$ implies that $C_e = 1.5$, which is a value on the order of unity, as expected. Thus, present findings for the evolution of SMD as a function of time during shear breakup are consistent with the jump conditions found earlier for secondary breakup in Ref. 3.

An interesting feature of both Eq. (4) for $SMD(t)$ and Eq. (6) for SMD_e is that neither result depends on the surface tension, and thus We_o, even though conditions required for the appearance of the shear breakup regime at low Oh_o and large ρ_f / ρ_g are controlled by We_o, and thus σ. In a sense, this behavior is somewhat analogous to the role of Reynolds number for turbulent mixing, where the presence of turbulent mixing for jets, wakes, etc., depends on the Reynolds number of the flow even though the rate of mixing itself is essentially independent of the Reynolds number once the flow is turbulent.

Similar to the earlier correlation of SMD_e,[3] Eq. (4) can be put into a form emphasizing the Weber number of drops produced by secondary breakup, as follows:

$$\rho_g SMD(t) u_o^2/\sigma = C_S(\rho_f / \rho_g)^{1/4}(t/t^*)^{1/2} \\ We_o/Re_o^{1/4}, \quad t_c/t^* \gg 1 \qquad (7)$$

where the left hand side (LHS) of Eq. (7) can be recognized as the Weber number of the drops formed by secondary breakup based on the initial relative drop velocity and the SMD. Then, similar to previous considerations for the jump conditions resulting from secondary breakup based on SMD_e,[3,4] Eq. (7) shows that the Weber number based on $SMD(t)$ and u_o can readily exceed values of We_o needed to initiate secondary breakup by a shock-wave disturbance. As discussed by Hsiang and Faeth,[4,5] however, subsequent tertiary breakup does not occur because these drops have had time to adjust to the disturbance and are subject to different criteria for breakup. Finally, even though Eq. (7) involves surface tension, it should be recalled from the earlier discussion that surface tension only affects the requirements for the onset of breakup for present

conditions, while drop sizes after secondary breakup are independent of surface tension, see Eqs. (4)-(6).

Steady-State Breakup Regime.
Phenomenological analysis of the steady-state breakup regime ($t_c/t^* \ll 1$), illustrated in Fig. 3, proceeds by assuming that the liquid boundary layer is laminar and fully developed, and that SMD ~ δ, following Hsiang and Faeth.[3] This yields an expression for SMD(t), as follows:

$$SMD(t)/(\nu_f t^*)^{1/2} = C_b, \quad t_c/t^* \ll 1 \qquad (8)$$

where C_b is an empirical constant on the order of unity. At this limit, Eq. (8) reveals that the SMD is independent of time, as suggested by the measurements for large liquid viscosities.

Present measurements of SMD(t), for drops having relatively large liquid viscosities, are correlated according to Eq. (8) in the lower plot of Fig. 4. These results include all test conditions for the glycerol 63% which involved relatively large liquid viscosities. It is evident that Eq. (8) provides a reasonably good correlation of the data, with $C_b = 1.5$, which is on the order of unity as anticipated by the derivation. Other properties of this regime are similar to the earlier findings of Hsiang and Faeth.[3] Additional experimental results are needed to fully exercise the phenomenological theory, and to properly define the transition condition between the transient and steady-state breakup regimes; work along these lines is currently in progress.

Drop Velocities

Velocities of Drops Produced by Secondary Breakup. Drop velocity distributions were measured as a function of time for all test conditions. It was found that the streamwise velocities of drops produced by secondary breakup were comparable to the streamwise velocity of the parent drop at each instant of time. Thus, the streamwise drop velocity data was summarized as the streamwise drop velocity relative to the parent drop, normalized by the streamwise parent drop velocity relative to the gas. This streamwise drop velocity ratio is plotted as a function of d/MMD, where MMD(t) is the local mass median drop diameter, in Fig. 5. Similar to the drop diameter results illustrated in Fig. 4, there is appreciable scatter of the drop velocity results in Fig. 5. This behavior comes about because relatively few drops are available to find an appropriate average drop velocity for a given breakup condition and time, supplemented by random (a turbulent-like velocity variation that is more evident for cross-stream drop velocities to be discussed subsequently). Nevertheless,

it is evident that the mean streamwise drop velocity ratio varies very little with drop size, yielding:

$$(\overline{u} - u_p)/(u_g - u_p) = 0.23 \qquad (9)$$

with a standard deviation of the constant on the RHS of Eq. (9) of 0.10 and the uncertainty of the value of the constant itself less than 0.03. This result suggests an appreciable acceleration of the drop liquid during breakup, as a result of motion in the liquid vortical layer as illustrated in Figs. 2 and 3, as well as acceleration of liquid motion in ligaments prior to final breakup into drops.

The behavior of drop velocities as the drops are formed, given by Eq. (9), is in marked contrast to the drop velocity distribution as a function of drop size at the end of breakup (the jump conditions) discussed by Hsiang and Faeth.[4,5] In the case of the jump conditions, drop velocities relative to the gas become progressively smaller as the drop sizes become smaller, rather than remaining constant similar to the results illustrated in Fig. 5. This behavior comes about because the characteristic relaxation times of small drops are smaller than those of large drops;[3] therefore, small drops undergo a greater acceleration after they are formed than large drops, and more closely approach the gas velocity as a result.

Consideration of the cross-stream velocities of drops produced by shear secondary breakup also is of interest because these velocities affect the cross-stream spread of a spray. Present measurements of cross-stream velocities indicated that the mean cross-stream velocities were small, e.g., $\overline{v}/u_g = 0.3\%$. In contrast, velocity fluctuations relative to the mean were relatively significant as shown by the probability density plot of v illustrated in Fig. 6. The standard deviation of the cross-stream velocity fluctuations illustrated in Fig. 6, is comparable to the standard deviation of the streamwise velocity fluctuations illustrated in Fig. 5, or $\overline{v}'/u_g = 8\%$.

Parent Drop Velocities. The results illustrated in Fig. 5 highlight the importance of the parent drop velocity for determining the evolution of the velocities of drops produced by shear secondary breakup as a function of time. This information was correlated based on the phenomenological analysis of Hsiang and Faeth.[4] The major assumptions of this analysis are as follows: virtual mass, Bassett history and gravitational forces ignored; gas velocities assumed to be constant; mass removal from the parent drop ignored; and constant average drag coefficient assumed over the period of breakup. For present conditions, virtual mass and Bassett history forces are small due to the large

values of ρ_f / ρ_g for the flows.[2] Similarly, gravitational forces were not a factor because drop motion was nearly horizontal and drag forces were much larger than gravitational forces. In addition, uniform gas properties were a condition of the present experiments. In contrast, the uniform parent drop size approximation was not really justified for present conditions because parent drop diameters at the end of breakup were only 12-30% of the original drop diameter and vary considerably over the period of breakup.[4] Nevertheless, accounting for these changes by adopting the original drop diameter and selecting a mean drag coefficient to best fit the measurements yielded reasonably good results in the past,[4] and was continued during present study as a result.

The analysis to find parent drop velocities as a function of time under the preceding approximations is presented by Hsiang and Faeth.[4] These results can be placed in the following form:

$$(u_p - u_{p_0})/(u_g - u_p) = 3\overline{C}_D(t/4t^*)/(\rho_f / \rho_g)^{1/2} \qquad (10)$$

where for present conditions $u_{p_0} = 0$. Earlier evaluation of parent drop velocities at the end of secondary breakup yielded a best-fit value of $\overline{C}_D = 5$ in Eq. (10).[4]

Measurements of drop velocities for various secondary breakup conditions, and times during secondary breakup, were obtained from both the present investigation and from the earlier work of Hsiang and Faeth.[4] These results are plotted according to Eq. (10) in Fig. 7. A best-fit correlation according to Eq. (10) also is shown on the figure. The comparison between the measurements and the correlation is seen to be quite good in spite of the approximations of the simplified analysis. This yields the same best-fit value, $\overline{C}_D = 5.0$, as the results found earlier by Hsiang and Faeth,[4] with an uncertainty(95% confidence) of the fit of 15%.

Drop Formation Rates

Drop formation rates were estimated using a simplified analysis. This involved the following major assumptions: liquid removal rates were proportional to the thickness of the boundary layer in the liquid on the upstream surface of the drop; liquid removal rates were proportional to the velocity of the drops formed relative to the velocity of the parent drop, estimated from Eq. (9); liquid removal rates were proportional to the perimeter of the drop; and breakup begins and ends at $t/t^* = 1.5$ and 5.5, respectively, as determined by Liang et al.[11] The resulting formulation for the rate of

production of dispersed liquid drops by secondary breakup, for the two breakup regimes, is relatively complex. It was noted, however, that the amount of liquid removed from the drop could be approximated by a clipped Gaussian function which simplifies the treatment of the onset and end of secondary breakup. Thus, only the simplified approach will be presented here because it should be useful for detailed analysis of drop breakup processes.

Present measurements of the cumulative volume of liquid removed from the parent drop as a function of time are plotted in Fig. 8. These results include all test conditions considered during the present investigation. The best-fit correlation of these results, according to a clipped Gaussian function, also is shown on the plot. It is evident that the clipped Gaussian function provides a good fit of the cumulative loss of volume of the parent drop as a function of t/t^*. This formula also provides a reasonably good fit of the rate of removal of drop liquid from the parent drop, except for the singular points at the beginning and end of the period where drop mass is being removed.

Drop-Containing Region

The region in the streamwise direction that contains drops will be considered in the following in order to provide information needed to evaluate when secondary breakup should be treated as a rate process rather than by jump conditions. This information can be summarized most compactly by plotting the boundaries of the drop-containing region, normalized by the initial drop diameter, as a function of t/t^*. These boundaries are given by the motion of the parent drop, and the motion of the smallest drop formed at the onset of breakup. Thus, it is evident that these boundaries are fixed by the motion of the parent drop whose velocity is given by Eq. (10). Based on this result, recalling that $\overline{C}_D$ was found to be a constant for present test conditions, it is evident that ρ_f / ρ_g is the only parameter of the problem. Thus, the boundaries of the drop-containing region were found for $\rho_f / \rho_g = 500$ and 1000, which bound the range of conditions considered during the present investigation.

The growth of the spray-containing region in the streamwise direction is plotted as a function of t/t^* in Fig. 9. Results are shown for the two different values of ρ_f / ρ_g that bound the present measurements, with the limiting values of t/t^* at the onset and end of drop breakup marked on the plot for reference purposes. The span of the drop-containing region increases with both the liquid/gas density ratio and time. For example, the drop-containing region at

the end of breakup is in the range $x/d = 40$-120 for $\rho_f / \rho_g = 1000$ but only $x/d = 38$-85 for $\rho_f / \rho_g = 500$. Similarly, the mean drop-containing region increases from zero at $t/t^* = 1.5$ to roughly $x/d = 40$-100 at $t/t^* = 5.5$. As noted earlier, the span of the secondary breakup time, distance traveled by the parent drop, and the span of streamwise distances where drops are present, at the end of breakup can be significant in some instances. In such cases, the information found during the present investigation about the temporal evolution of the sizes and velocities of drops produced by secondary breakup, as well as the rate of liquid removal from the parent drop during secondary breakup, should be helpful.

Conclusions

The properties of drops produced by secondary breakup in the shear breakup regime were studied as a function of time for shock-wave-initiated disturbances in air at normal temperature and pressure. The test liquids included water, ethyl alcohol and various glycerol mixtures to yield We_O of 125-375, Oh_O of 0.0034-0.0130, ρ_f / ρ_g of 678-936 and Re_O of 3070-11150. The major conclusions of the study are as follows:

1. Drops produced by shear breakup at low Ohnesorge numbers satisfy the universal root normal distribution of Simmons,[19] with MMD/SMD = 1.2, at each instant of time during the breakup process.

2. The evolution of SMD as a function of time for drops formed by shear breakup at low Ohnesorge numbers could be correlated in terms of a simple phenomenological analysis which implied that drop sizes were related to the thickness of the liquid boundary layer formed by the action of drag on the upstream surface of the parent drop.

3. The mean velocities of drops formed by shear breakup at low Ohnesorge numbers were relatively independent of drop size, and were nearly equal to the mean velocities of the parent drop at each instant of time.

4. The rms velocity fluctuations of drops formed by shear breakup at low Ohnesorge numbers were relatively independent of drop size, and were on the order of 10% of the mean relative streamwise velocity between the gas and the parent drop.

5. The velocities of the parent drop as a function of time during shear breakup at low Ohnesorge numbers could be correlated reasonably well based on the simple phenomenological theory developed during earlier work.[4]

6. The rate of liquid removal from the parent drop was represented reasonably well by a simplified phenomenological theory accounting for the variation of drop sizes and velocities as a function of time during the breakup process.

Present conclusions are limited to the large liquid/gas density ratio and low Ohnesorge number conditions that are most representative of sprays at atmospheric pressure. In addition, the evolution of secondary drop breakup processes in the bag, multimode, drop-piercing and catastrophic breakup regimes, along with effects of heat and mass transport on drop breakup processes, must be resolved in order to achieve the technology base needed to analyze dense sprays in a rational manner.

Acknowledgments

References

[1]Wu, P.-K., Hsiang, L.-P. and Faeth, G.M., "Aerodynamic Effects on Primary and Secondary Breakup," Prog. Astro. Aero., in press.

[2]Faeth, G.M., "Structure and Atomization Properties of Dense Turbulent Sprays," Twenty-Third Symposium (International) on Combustion, The Combustion Institute, Pittsburgh, 1990, pp. 1345-1352.

[3]Hsiang, L.-P. and Faeth, G.M., "Near-Limit Drop Deformation and Secondary Breakup," Int. J. Multiphase Flow, Vol. 18, 1992, pp. 635-652.

[4]Hsiang, L.-P. and Faeth, G.M, "Drop Properties After Secondary Breakup," Int. J. Multiphase Flow, Vol. 19, 1993, pp. 721-735.

[5]Hsiang,L.-P. and Faeth, G.M., "Drop Deformation and Breakup due to Shock Wave and Steady Disturbances," Int. J. Multiphase Flow, Vol. 21, No. 4, 1995, pp. 545-560.

[6]Giffen, E., and Muraszew, A., The Atomization of Liquid Fuels, Chapman and Hall, London, 1953.

[7]Hinze, J.O., "Fundamentals of the Hydrodynamic Mechanism of Splitting in Dispersion Processes," AIChE J., Vol. 1, 1955, pp. 289-295.

[8]Clift, R., Grace, J.R. and Weber, M.E., Bubbles, Drops and Particles, Academic Press, New York, 1978, pp. 26 and 339-347.

[9]Krzeczkowski, S.A., "Measurement of Liquid Droplet Disintegration Mechanisms," Int. J. Multiphase Flow, Vol. 6, 1980, pp. 227-239.

[10]Wierzba, A. and Takayama, K., "Experimental Investigations on Liquid Droplet Breakup in a Gas Stream," Rep. Inst. High Speed Mech., Tohoku Univ., Vol. 53, 1987, pp. 1-99.

[11]Liang, P.Y., Eastes, T.W. and Gharakhari, A., "Computer Simulations of Drop Deformation and Drop Breakup," AIAA Paper No. 88-3142, 1988.

[12]Ranger, A.A. and Nicholls, J.A., "The Aerodynamic Shattering of Liquid Drops," AIAA J., Vol. 7, 1969, pp. 285-290.

[13]Reinecke, W.G. and McKay, W.L., "Experiments on Waterdrop Breakup Behind Mach 3 to 12 Shocks," Sandia Corp., Rept. SC-CR-70-6063, 1969.

[14]Reinecke, W.G. and Waldman, G.D., "A Study of Drop Breakup Behind Strong Shocks with Applications to Flight," Avco Rept. AVSD-0110-70-77, 1970.

[15]Dabora, E.K., "Production of Monodisperse Sprays," Rev. Sci. Inst., Vol. 38, 1967, pp. 502-506.

[16]Lange, N.A., Handbook of Chemistry, 8th ed., Handbook Publishers, Inc., Sandusky, Ohio, 1952, pp. 1134 and 1709.

[17]Wu, P.-K., Ruff, G.A. and Faeth, G.M., "Primary Breakup in Liquid/Gas Mixing Layers," Atomization and Sprays, Vol. 1, 1991, pp. 421-440.

[18]White, F.M., Viscous Fluid Flow, McGraw-Hill, New York, 1974.

[19]Simmons, H.C., "The Correlation of Drop-Size Distributions in Fuel Nozzle Sprays," J. Engr. for Power, Vol. 99, 1977, pp. 309-319.

[20]Belz, M.H., Statistical Methods in the Process Industries, Wiley, New York, 1973, pp. 103-104.

[21]Schlichting, H., Boundary Layer Theory, 7th ed., Pergamon Press, New York, 1975, pp. 234-235 and 599.
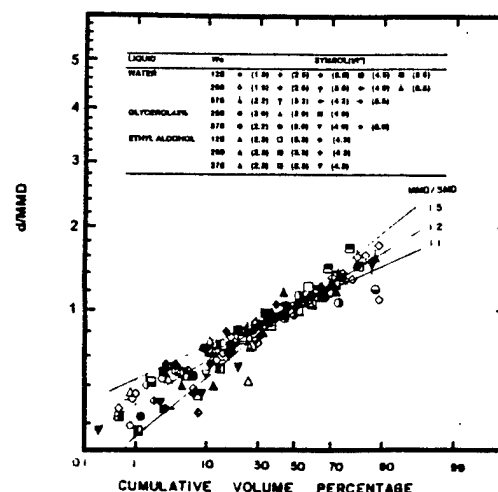
Figure 1. Diameter distributions for drops produced by shear breakup plotted according to the root normal size distribution function.

Table 1. Summary of Test Conditions[a]

Drop Liquid	d_o (mm)	ρ_f/ρ_g (-)	$\mu_f \times 10^4$ (kg/ms)	$\sigma \times 10^3$ (N/m)	$Oh_o \times 10^3$ (-)	Re_o (-)
Water	1.00	845	8.94	70.8	3.40	6240-11150
Ethyl Alcohol	0.78	678	16.0	24.0	11.0	3070-5570
Glycerol (42%)[b]	1.00	936	35.0	65.4	13.0	6000-10720
Glycerol (63%)[b]	1.00	984	108.0	64.8	39.0	5840-8550

[a]Breakup for We_o = 125-375 in air initially at 98.8 kPa and 297 ± 2K in the driven section of the shock tube with shock Mach numbers in the range 1.08-1.31. Properties of air taken at normal temperature and pressure: ρ_g = 1.18 kg/m³ and μ_g = 18.5 × 10⁻⁶ kg/ms.

[b]Percentage glycerin by mass.
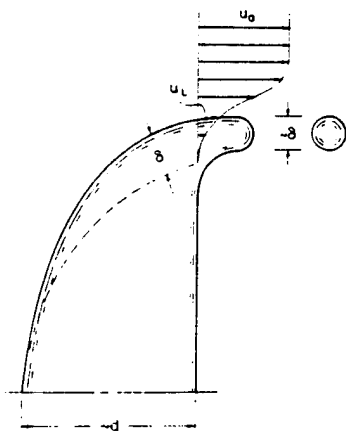
Figure 2. Sketch of the transient shear breakup mechanism for $t_c/t^* \gg 1$.
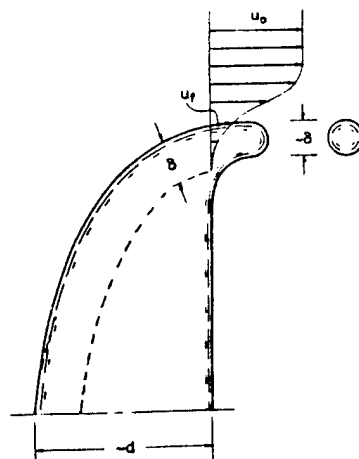
Figure 3. Sketch of the steady-state shear breakup mechanism for $t_c/t^* \ll 1$.
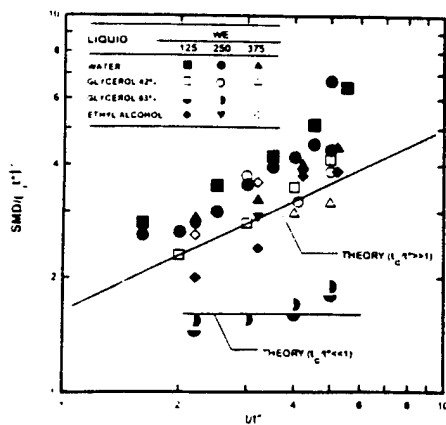
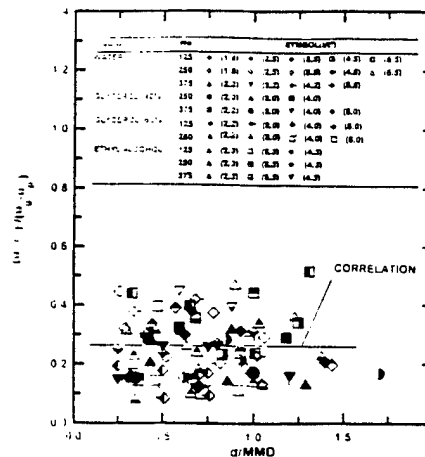Figure 4. Temporal variation of the SMD of drops produced by shear breakup

Figure 5. Streamwise velocity distributions as a function of size for drops produced by shear breakup.
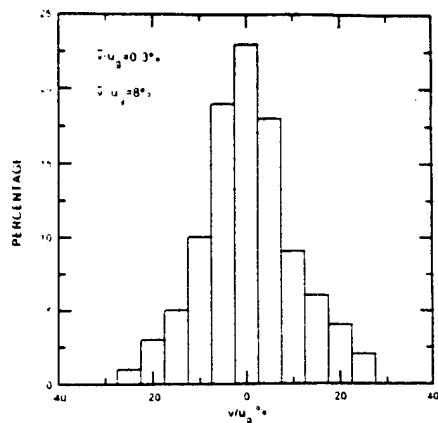
Figure 6.   Prob ability density function of cross-stream velocity fluctuations.
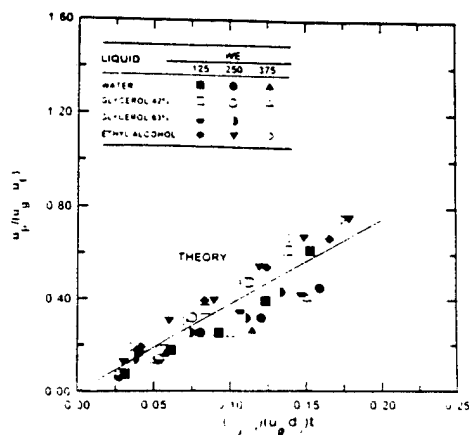

Figure 7.   Parent drop velocities as a function of time during shear breakup.
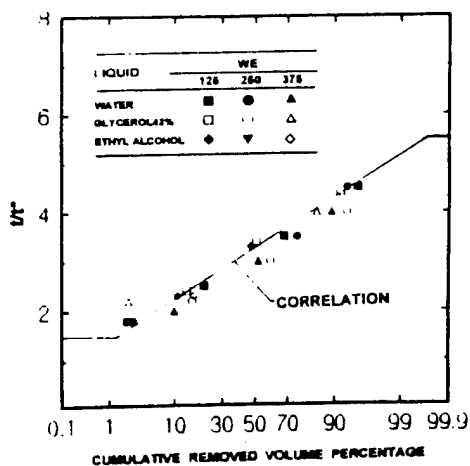

Figure 8.   Degree of mass removal from the parent drop as a function of time during shear breakup.
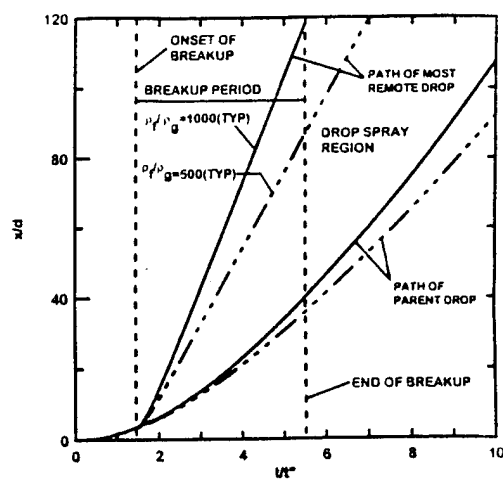

Figure 9.   Growth of the spray-containing region during shear breakup.

11

Appendix D: Wu, J.-S. and Faeth, G.M. (1993) Sphere wakes in still surroundings at intermediate Reynolds numbers. <u>AIAA J</u>. 31, 1448-1455.

Sphere Wakes in Still Surroundings at Intermediate Reynolds Numbers

J.-S. Wu* and G. M. Faeth†
University of Michigan, Ann Arbor, Michigan 48109

The wakes of spheres in a still environment were studied for sphere Reynolds numbers Re in the range 30–4000. The experiments consisted of towed spheres in quiescent baths of glycerin and water mixtures. Measurements included dye traces illuminated by a laser light sheet for visualization and laser velocimetry for streamwise velocities. The recirculation region on the downstream side of the sphere was stable and symmetric for $Re < 200$, stable and unsymmetric for $200 \leq Re \leq 280$, and unstable with vortex shedding for $Re \geq 280$. Three wake regions were identified: a fast-decay region that was observed only when vortex shedding was present, followed in succession by turbulent and laminar wake regions. Vortex shedding increased the distance to the onset of the turbulent wake region by an order of magnitude due to the presence of the fast-decay wake region. Mean velocities within the turbulent and laminar wake regions scaled according to classical similarity theories, with transition between these regions at conditions where their estimates of mean streamwise velocities along the axis were the same: this occurred at a local wake Reynolds number $Re_w \approx 10$. Within the turbulent wake region, turbulence intensities along the axis were roughly 85% for $Re_w > 70$; however, as the onset of the laminar wake region was approached, turbulence intensities along the axis were proportional to $Re_w^{7/4}$, which is consistent with scaling proposed earlier for the final decay period of axisymmetric wakes.

Nomenclature

a = velocity decay exponent in fast-decay wake region
C = constant for final decay period, Eq. (11)
C_D = drag coefficient
d = sphere diameter
ℓ = characteristic wake width, Eq. (3)
ℓ_t = scaled characteristic wake width, Eq. (9)
R = sphere radius
Re = sphere Reynolds number, dU_s/ν
Re_w = local wake Reynolds number, $\ell\bar{u}_c/\nu$
r = radial distance
t = time
U_s = sphere velocity
$(U_o)_t$ = velocity scale for turbulent wake region
$\bar{u}$ = mean streamwise velocity
$\bar{u}'$ = rms streamwise velocity fluctuation
x = streamwise distance from center of sphere
θ = initial momentum thickness of wake, Eq. (1)
ν = kinematic viscosity

Subscripts

c = centerline value
cm = uncorrected centerline value
o = virtual origin condition
tr = transition from turbulent to laminar wake
∞ = ambient condition

Introduction

THE flow associated with spheres has attracted attention due to numerous applications, e.g., dispersed particle-laden flows, sprays, and rainstorms, among others. Recent work on the production of turbulence by dispersed phases,[1,2] however, has shown the need for more information about the structure of sphere wakes at the intermediate sphere Reynolds

numbers ($10 < Re < 10^3$) that often are encountered for drops and particles in sprays and other dispersed flows. Particularly important issues are the effects of turbulence and vortex shedding from the sphere on wake structure, and the range of conditions for which such effects are observed. Motivated by these observations, the objective of the present investigation was to measure flow properties near spheres at intermediate Reynolds numbers, with particular emphasis on properties within the wake.

Early studies of the flow associated with spheres at intermediate Reynolds numbers are discussed in the extensive series of review articles by Torobin and Gauvin,[3] and references cited therein. Initial work emphasized drag and flow properties near the sphere, with later experimental and computational work along these lines reported by Pruppacher et al.,[4] Rimon and Cheng,[5] and Roos and Willmarth.[6] Subsequently, several studies focused on the near wake of the sphere, including the nature of the recirculation zone behind the sphere and the characteristics of vortex shedding from this region.[7-16] These results established that a recirculation zone begins to form at a Re of roughly ten, that this zone grows in size as the Re increases, and that vortex shedding from the sphere into the wake begins at roughly $Re = 300$ and continues to affect near-wake properties at higher values of Re in the intermediate Reynolds-number regime. Within the intermediate Reynolds-number regime, the configuration of vortices shed from the sphere involves closed-end double-helix vortex tubes unwinding from a cylindrical vortex sheet around the periphery of the sphere, giving the appearance of a vortex street passing into the sphere wake when viewed in cross section.[15,16] These results were obtained from flow visualization, however, so there is little quantitative information available about the effect of vortex shedding on wake properties.

Existing quantitative information about sphere wakes is limited largely to the turbulent wake (see Refs. 17–22 and references cited therein). This involved measurements in the wakes of various axisymmetric objects far enough downstream so that wake properties did not exhibit the periodic behavior associated with vortex shedding and were controlled by the drag rather than the shape of the object. These measurements generally were completed for object (sphere) Reynolds numbers on the order of 10^4 or greater, with local wake Reynolds numbers on the order of 10^2 or greater. Thus, the properties of

wakes for intermediate Reynolds numbers, or even whether turbulent wakes are present for such conditions, are unknown in spite of the importance of this Reynolds-number range for dispersed multiphase flows.[1,2]

The present investigation was undertaken to provide new information about the structure of the flow near spheres at intermediate sphere Reynolds numbers. This included visualization of the flow near the spheres to provide information about the recirculation zone and vortex shedding into the wake, measurements of mean streamwise velocities both near the spheres, and in their wakes, and measurements of rms velocity fluctuations along the flow axis, extending to conditions where the wakes were laminar. The experiments involved spheres towed through quiescent water and glycerol mixtures to achieve sphere Reynolds numbers in the range 30–4000. Within both the turbulent and laminar portions of the wakes, velocity measurements were compared with classical similarity correlations and correlations of turbulence properties in wakes,[18-27] to help define conditions for the transition between these regimes and the scaling of turbulence properties at intermediate wake Reynolds numbers.

Experimental Methods

Apparatus

A sketch of the test apparatus appears in Fig. 1. The experiment involved traversing a sphere through a still liquid bath and observing flow properties at the center of the bath. The liquid bath was filled to a depth of 875 mm within a windowed tank ($415 \times 535 \times 910$ mm). The sides and bottom of the tank were covered with insulation (not shown in Fig. 1) to minimize natural convection disturbances, aside from small openings needed for optical access. The viscosity of the bath liquid was varied so that a range of sphere Reynolds numbers could be considered using a sphere of fixed size and a modest range of velocities.

The test sphere was a 10-mm-diam plastic ball (polished polycarb ball, ± 50 μm radius tolerance, sphericity within 50 μm, surface roughness less than 16 μm). The sphere was mounted on a 125-μm-diam stainless-steel wire which passed horizontally through its center and was sealed with epoxy. The wire was mounted in tension between two struts that could be traversed down the corners of the tank. Tests with no sphere present showed that disturbances from the wire support system were negligible in comparison to background disturbances.
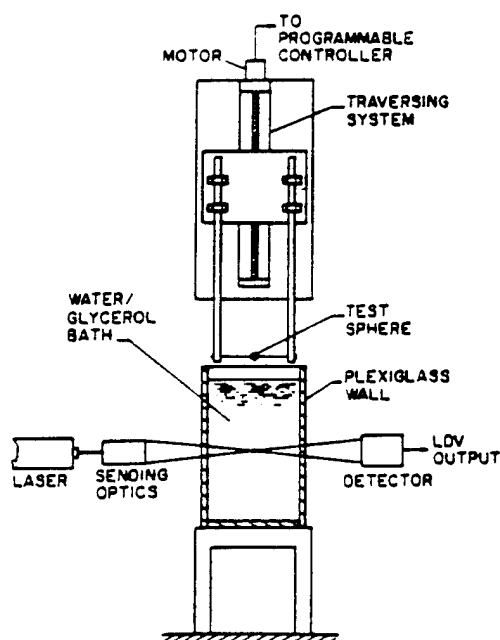

Fig. 1 Sketch of the experimental apparatus.

Additionally, the arrangement was sufficiently rigid so that sphere vibrations during a traverse could not be detected.

The traversing system involved a counterbalanced mounting plate, which could move along a linear bearing system, to support the struts. The motion of the plate was controlled by a stepping motor driven linear positioner (Daedal, Model 008-2686 single-axis positioner). The positioner was programmed so that it accelerated to the appropriate sphere velocity (147–476 mm/s) in the first 150 mm of travel, just prior to entering the bath. The test velocity was maintained for the next 700 mm (300 mm beyond the measuring station) before decelerating to a stop at the bottom of the tank in the last 150 mm of travel. The arrangement provided test sphere velocities with an accuracy of 1%, based on the position indicator of the traversing system, with velocity variations within this range for the constant speed portion of the traverse.

Instrumentation

Flow Visualization

Light sheet illuminated dye traces were used to observe the recirculation region behind the sphere and the vortex shedding process, similar to past work.[6-16] This was done by painting a liquid soluble dye (Higgins drawing ink no. 4085) near the forward stagnation point of the sphere and photographing the dye trace after illumination by a vertical light sheet passing through the axis of the flow. The light sheet was formed by focusing the 488-nm line of an argon-ion laser with a spherical lens to yield a waist diameter of 200 μm, and then spreading the beam with a cylindrical lens to illuminate a 300-mm section along the axis of motion. The resulting dye pattern was photographed using an SLR camera (3200 ASA black and white film) with exposure times of 1–4 ms to stop the motion of the fluid. Visualizations shown here extend roughly ± 30 mm from the center of the tank.

Laser Velocimetry

The laser velocimeter was identical to the fixed channel arrangement used by Parthasarathy and Faeth[1] and will be described only briefly. A dual-beam forward-scatter configuration was used which had a measuring volume diameter and length of 0.1 and 1.2 mm, respectively. Directional bias and ambiguity were eliminated using a Bragg-cell frequency shifter. The bath liquid was seeded with titanium dioxide particles (2.8 μm nominal diameter) to provide data rates in the range 0.5–2 kHz. The velocities were found from the low-pass filtered analog output of a burst-counter signal processor, using a 12-bit analog/digital converter operating at a constant sampling frequency (1–4 kHz), and storing 120 k samples per traverse.

The laser velocimeter measuring location was fixed; therefore, the trajectory of the sphere was traversed to observe various points in the flow. The streamwise traverse was carried out by the motion of the sphere itself, with distances known from the position indicator of the linear positioner. Positioning accuracy in the streamwise direction was controlled primarily by uncertainties of locating the center of the sphere at the measuring volume and the time between samples, yielding an uncertainty of 0.4 mm for each velocity determination used during ensemble averaging. Cross-stream traverses were carried out by moving the wire support points with a manual traversing system attached to the struts, yielding a positioning accuracy of 0.2 mm.

Measurements were carried out by ensemble averaging results from 20 to 120 traverses at a particular radial position and sphere Reynolds number. The number of traverses was selected to control the experimental uncertainties and was large in regions where effects of vortex shedding were important (due to large traverse-to-traverse variations of flow properties) and when rms velocity fluctuations were sought. Traverses only were initiated after bath disturbances from the previous traverse were sufficiently decayed (specified to be $\bar{u}'/U_t < 0.5\%$).

Table 1 Test conditions[a]

Re (-)	Glycerin concentration[b]	ν, mm²/s	U_s, mm/s	C_D (-)	θ, mm	$(U_o)_i/U_s$[f]
35	81	42.0	147	1.91[c]	4.88	1.9
60	81	42.0	252	1.42[c]	4.22	2.0
90	81	37.8–41.0	340–369	1.16[c]	3.81	2.3
170	76	24.0–28.0	408–476	0.36[c]	3.29	2.6
280	62	10.1–11.7	283–328	0.59[d]	2.72	2.4
400	62	10.2	408	0.603[e]	2.75	2.0
960	50	4.8	461	0.430[e]	2.32	0.9
4000	0	1.02	408	0.381[e]	2.18	0.8

[a] Sphere diameter of 10 mm; bath temperature variation <0.5 K during tests; $\bar{u}$, U'_s <0.5% before tests.
[b] Percent glycerin in water by mass.
[c] $C_D = 24(1 + Re^{2/3}/6)/Re$, from Putnam.[28]
[d] Fitted from measured radial mean velocity distribution.
[e] $C_D = 0.28 + 6/Re^{1/2} + 21/Re$, from Kürten et al.[29]
[f] Based on a fixed virtual origin at $x_o/\theta = 1$.

Experimental uncertainties varied with sphere Reynolds number and position in the wake, with measurements in the far wake terminated when background disturbances became significant in comparison to wake velocities. For data reported here, uncertainties (95% confidence) of mean streamwise velocities were less than 13%, and those of rms streamwise velocity fluctuations were less than 25%. All measurements were repeatable within these ranges over a period of testing of several months. These uncertainties are high in comparison to conventional laser velocimeter measurements due to the relatively low velocities and the ensemble averaging technique of the present tests.

Test Conditions

Test conditions are summarized in Table 1. Here and in the following, all velocities are relative to an inertial reference frame. The densities and viscosities of the test liquids were measured periodically during testing with a hydrometer and a Cannon/Fenske viscometer. Effects of bath temperature changes on kinematic viscosities were compensated by adjusting the sphere velocity to obtain the desired sphere Reynolds number.

Drag coefficients for the various sphere Reynolds numbers generally were computed from correlations due to Putnam[28] and Kürten et al.[29] The one exception was $Re = 280$, which was at the onset of vortex shedding where existing drag correlations were suspect; therefore, C_D at this condition was found from the measured velocity defect in the wake. Values of the initial momentum thickness of the wakes then were computed as follows[21]:

$$\theta = (C_D d^2/8)^{1/2} \tag{1}$$

Wake Similarity

Turbulent Wake

It is well known that mean velocity distributions in high Reynolds-number axisymmetric turbulent wakes become self-preserving far from the drag-producing object. Within the self-preserving region, mean velocities correlate reasonably well with predictions based on a constant eddy viscosity over the wake cross section, in spite of the crudeness of this approximation; see Uberoi and Freymuth[19] and references cited therein. Based on results appearing in Tennekes and Lumley,[21] this yields the following expression for streamwise mean velocities[1]:

$$\bar{u}/U_s = 2.23\left[(x - x_o)/\theta\right]^{-2/3} \exp(-r^2/2\ell^2) \tag{2}$$

where the characteristic width of the wake is given by

$$\ell/\theta = 0.47\left[(x - x_o)/\theta\right]^{1/3} \tag{3}$$

and x_o is the virtual origin of the flow. The local wake Reynolds number based on the centerline velocity and characteristic wake width then becomes

$$Re_w = \ell\bar{u}_c/\nu = 1.048(\theta U_s/\nu)\left[(x - x_o)/\theta\right]^{-1/3} \tag{4}$$
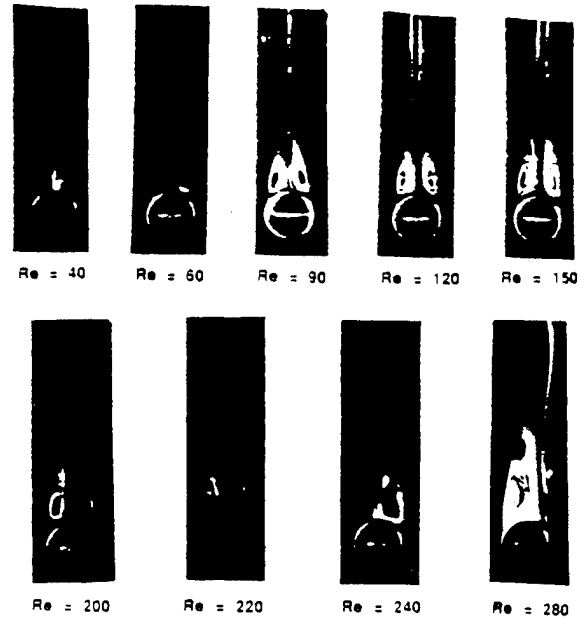

Fig. 2 Visualization of near wakes for intermediate Reynolds numbers ($Re = 40–280$).

Laminar Wake

Laminar wake regions also were observed during the experiments. Streamwise mean velocities in this region are given by classical similarity analysis, as follows[23]:

$$\bar{u}/U_s = \left[\theta^2 U_s/4\nu(x - x_o)\right] \exp(-r^2/2\ell^2) \tag{5}$$

where

$$\ell/\theta = \left[2\nu(x - x_o)/\theta^2 U_s\right]^{1/2} \tag{6}$$

From Eqs. (5) and (6), the local wake Reynolds number based on the centerline velocity and the characteristic width in the laminar wake regime becomes

$$Re_w = \ell\bar{u}_c/\nu = \theta^2\left[U_s^3/8\nu^3(x - x_o)\right]^{1/2} \tag{7}$$

The mean velocity $\bar{u}$ has been used in Eqs. (5-7), even for a steady laminar flow, because present values were obtained as ensemble averages which were influenced to some extent by background disturbances in the bath.

Results and Discussion

Near- and Fast-Decay Wake Regions

Photographs of the light-sheet illuminated dye traces for sphere Reynolds numbers in the range 40–280 appear in Fig. 2.

This range is representative of conditions where vortex shedding is not present, $Re \leq 240$, up to conditions where vortex shedding just begins, $Re \approx 280$. In the region where they overlap ($Re < 200$), present observations are very similar to those Nakamura[15] for freely falling spheres, except for minor effects due to different methods of introducing the dye. This suggests that the present horizontal wire support did not have a significant effect on flow properties near the sphere. For $20 \leq Re < 200$ (the former being the lowest value considered), a stable and symmetric recirculation zone is attached to the downstream side of the sphere, with the size of the recirculation zone progressively increasing as Re increases. Within this region, present measurements of the angle between the attachment points of the recirculation region were in good agreement with measurements for freely falling spheres due to Nakamura.[15] Throughout this region, dye traces leaving the downstream end of the recirculation zone were smooth and gave little evidence of unsteady or turbulent-like behavior over the region where they could be seen. For $20 \leq Re \leq 240$, the recirculation zone still remained attached and stable; however, it generally was no longer symmetric. Additionally, the dye trace leaving the recirculation zone remained along the axis and was only slightly more irregular than for $Re < 200$. As is evident from Fig. 2, however, this behavior changed significantly at $Re = 280$ where vortex shedding began. Typical of behavior at higher Re, where effects of vortex shedding on wake properties were very significant, the recirculation zone was very unsymmetric and the dye trace leaves the recirculation zone near its edge.

As noted earlier, the wake flow changed at $Re \approx 280$ so that the recirculation zone was no longer stable and vortex shedding began. This observation is in good agreement with results for freely falling spheres, suggesting small effects of the wire support on the vortex-shedding process. For example, Magarvey and MacLatchy[9] and Goldberg and Florsheim[10] report $Re = 300$ and 270, respectively, for this transition for freely falling spheres. Dye traces at higher Reynolds numbers
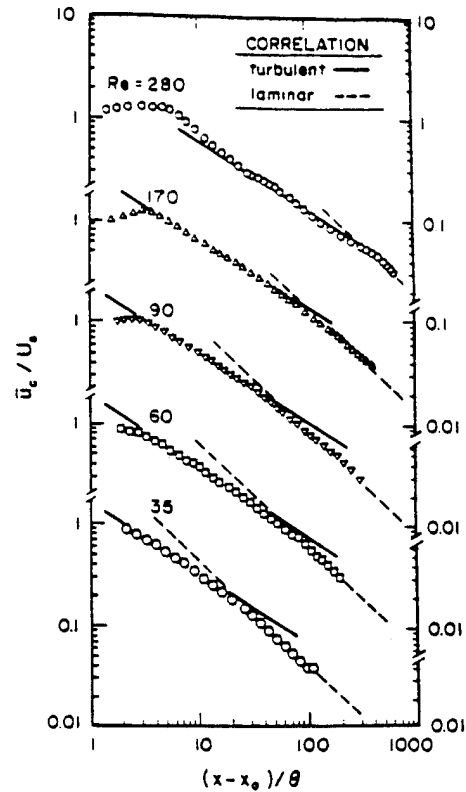

Fig. 4 Mean streamwise velocities along the wake axis ($Re = 35-280$).

Fig. 3 Mean streamwise velocities along the wake axis ($Re = 400-4000$).

were similar to the observations of others,[10,16] with increasing sphere Reynolds numbers yielding dye traces having finer scaled features and a large-scale back and forth distortion of the dye traces that is consistent with the double helix vortex tube structure thought to represent the vortex-shedding process.[16]

Streamwise mean velocities along the wake axis are illustrated in Fig. 3 for conditions where vortex shedding has a strong effect on mean velocities ($Re = 400$, 960, and 4000) and in Fig. 4 for conditions where effects of vortex shedding are either weak ($Re = 280$) or absent ($Re = 35$, 60, 90, and 170). The results are plotted as a function of x/θ [or $(x - x_o)/\theta$ with $x_o/\theta = 1$ as described later], so that they can be related to the similarity expressions for turbulent and laminar wakes, Eqs. (2) and (5). The measurements on the plots begin close to the rear stagnation point of the sphere, x/d in the range 0.5–1.0, and are ended when wake velocities become too low for accurate measurements.

The first feature evident from the results illustrated in Figs. 3 and 4 is the increase of velocity with increasing distance very near the sphere. This behavior is caused by deceleration of the backflow along the axis of the recirculation zone as the sphere is approached. The maximum velocity along the axis, however, is reached relatively close to the sphere, at $(x - x_o)/\theta$ of 4–6 or $x/d = 1.4 \pm 0.2$, with the maximum tending to approach the sphere when the recirculation zone becomes smaller as Re decreases.

When vortex shedding is present, $Re \geq 280$, mean velocities along the axis initially exhibit a more rapid decay than farther into the wake (cf. Figs. 3 and 4). The rate of decay in this region tends to decrease as Re decreases toward the onset of vortex shedding. For example, if $\bar{u}/U_s \sim x^{-a}$ in the fast-decay wake region, maximum values of a are 1.8, 1.7, 1.6, and 1.2 for $Re = 4000$, 960, 400, and 280, respectively. Thus, the strength of the vorticity being shed from the sphere affects the enhancement of near-wake mixing rates.
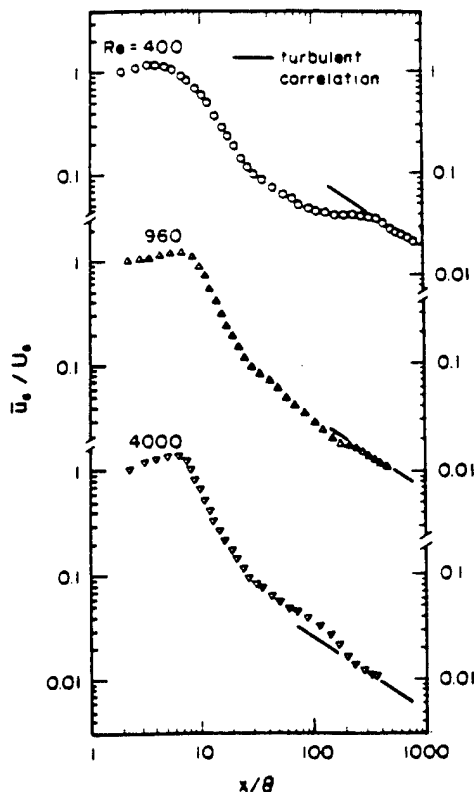
Turbulent Wake Region

The end of the fast-decay wake, and regions behaving like turbulent and laminar wakes, were identified using the classical similarity expressions of Eqs. (2) and (5). It was found that laminar wake behavior was in good agreement with Eq. (5), after choosing $x_o/\theta = 1$; therefore, these correlations are entered directly for Re in the range 35–280 where laminar wakes were observed (Fig. 4). Additionally, the turbulent portions of the wakes were in fair agreement with Eq. (2) using the same value of x_o/θ when eddy shedding was absent; however, the plots were offset when eddy shedding was present due to the influence of the fast-decay wake region on the virtual origin. Thus, to display results for the various wake regimes, with no change of virtual origin, a generalized correlation for the turbulent wake region was developed from Eqs. (2) and (3) as follows:

$$\bar{u}/U_t = (U_o)_t/U_t \left[(x-x_o)/\theta\right]^{-4} \exp(-r^2/2\ell_t^2) \qquad (8)$$

where

$$\ell_t/\theta = \left[U_t/2(U_o)_t\right]^{-1} \left[(x-x_o)/\theta\right]^{-1} \qquad (9)$$

The values of the parameter $(U_o)_t/U_t$ were selected to provide the turbulent wake fits illustrated in Figs. 3 and 4 and are summarized in Table 1. The parameter $(U_o)_t/U_t = 2.23$ for exact agreement with Eq. (2): present measurements agree with this estimate for $Re \leq 400$, with an average value and standard deviation of 2.2 and 0.3. Results at $Re = 960$ and 4000 exhibit lower values of $(U_o)_t/U_t$, near unity, which are consistent with the value of 0.9 found for the turbulent wake of a sphere at $Re = 8600$.[19]

The results plotted in Fig. 3 indicate that the turbulent wake region is reached at $x/\theta \approx 200$ for $Re \geq 960$, which corresponds to x/d in the range 40–50. This is comparable to other observations of the onset of fully developed turbulent wake properties for spheres and other blunt objects for $Re > 1000$ (which involve vortex shedding from the object).[1-19] In contrast, when vortex shedding is absent, Fig. 4 for $Re \leq 170$, the onset of the turbulent wake region is reached at $(x-x_o)/\theta \leq 4$, which corresponds to $x/d \leq 1.7$–2.5; this is comparable to Chevray's[20] observation of a rapidly developing turbulent wake behind a slender spheroid at $Re = 458,000$ (based on the body diameter) for conditions where vortex shedding also is absent. Chevray[20] also points out that his behavior agrees with Townsend's[30] prediction that the self-preserving turbulent wake should develop rapidly if production of turbulence within the separation region is small, i.e., stronger turbulence production in the presence of vortex shedding both enhances mixing rates in the fast-decay wake and causes the onset of the turbulent wake region to be deferred. Conditions at $Re = 400$ and 280 (Figs. 3

and 4) represent intermediate behavior as the onset of vortex shedding is approached; at $Re = 400$, onset of the turbulent wake region occurs near $x/\theta = 300$ or $x/d \approx 80$ while at $Re = 280$, onset occurs near $x/\theta = 20$ or $x/d \approx 5$. It is not surprising that x/d for onset of the turbulent wake becomes smaller as the onset of vortex shedding is approached; however, additional study is needed to establish that different relative rates of decay of vortices shed from the sphere and development of turbulence yield a maximum in the streamwise distance required to develop a turbulent wake structure for $Re < 10^3$.

For $Re \leq 280$, the measurements extended far enough so that a laminar wake region scaling according to Eq. (5) was reached (see Fig. 4). It is seen that the transition from turbulent to laminar wake behavior occurs where the two similarity expressions for $\bar{u}_c/U_t$ cross Eq. (2) for the turbulent wake because $(U_o)_t/U_t = 2.23$ for this range of Re and Eq. (5) for the laminar wake. Thus, an expression for the transition condition can be obtained by equating Eqs. (2) and (5) to yield

$$(x-x_o)_{tr}/\theta = 1.41 \times 10^{-3}(\theta U_t/\nu)^3 \qquad (10)$$

where this expression only has been established for $Re < 400$. Substituting Eq. (10) into either Eq. (4) or Eq. (7) yields a wake Reynolds number at transition from the turbulent to laminar wake regimes of $Re_{wtr} = 9.4$. Tennekes and Lumley[21] note that this transition should take place for Re_{wtr} on the order of unity. This is not in disagreement with present findings in view of the somewhat arbitrary selection of velocity and length scales in the definition of Re_w and the range of $(x-x_o)/\theta$ required to complete transition from turbulent to laminar wake behavior.

The radial profiles of mean streamwise velocities in the turbulent wake region are illustrated in Fig. 5. In addition to present measurements, results from Uberoi and Freymuth[19] for a sphere having a $Re = 8600$ and Chevray[20] for a slender body having a $Re = 458,000$ (which involve conditions where vortex shedding is present and absent, respectively) are shown on the plots. Variations of the virtual origin are handled by scaling in terms of $(U_o)_t/U_t$ through Eqs. (8) and (9) as before. The value of $(U_o)_t/U_t = 0.9$ for the measurements of Uberoi and Freymuth,[19] which is comparable to present results when effects of vortex shedding are strong, as noted earlier. The higher value of $(U_o)_t/U_t = 3.0$ for the measurements of Chevray[20] is typical of present measurements when vortex shedding is either absent or weak; see Table 1.

All of the results illustrated in Fig. 5 are seen to be reasonably correlated with each other and with the Gaussian velocity distribution function found from simplified similarity theory for the self-preserving turbulent wake.[21] Present measurements are identified by x/d but they extend over the full range where $\bar{u}_c/U_t$ agrees with turbulent wake scaling in Fig. 4. Thus, results illustrated in Fig. 5 extend from $Re_w > 90$ for measurements from Refs. 19 and 20 down to $Re_w \approx 10$ near transition to laminar wake behavior for the present measurements, with effects of vortex shedding both present and absent. Clearly, mean velocity distributions within turbulent wakes generally are independent of these factors, after appropriate definition of a virtual origin or a velocity scale like $(U_o)_t$.

The relative insensitivity of mean velocities within turbulent wakes to the specific properties of the turbulence are highlighted by considering streamwise rms velocity fluctuations along the axis. These results are plotted in terms of the turbulence intensity at the axis $(\bar{u}'/\bar{u})_c$ as a function of x/d in Fig. 6. The measurements of Uberoi and Freymuth[19] are shown in the figure, along with present measurements for Re in the range 280–4000 (present measurements were not feasible at lower values of Re because excessive numbers of traverses were required to establish reliable values of $\bar{u}_c'$). Results for the full range of x/d of the measurements are illustrated with the portion in the turbulent wake region (or the fully developed turbulent wake region identified in Ref. 19) denoted by solid symbols. These results have not been corrected for background disturbances due to uncertainties about these effects in
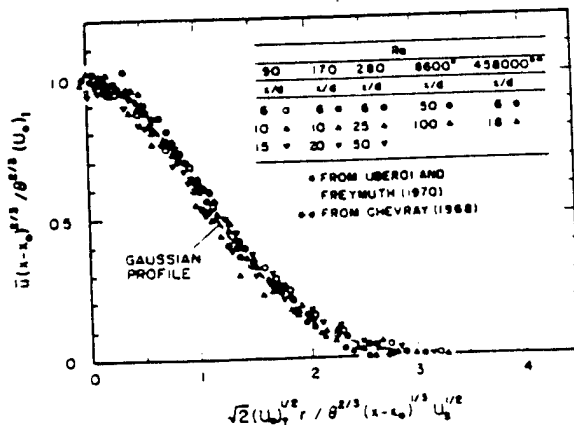

Fig. 5 Correlation of radial profiles of mean streamwise velocities in the turbulent wake region.
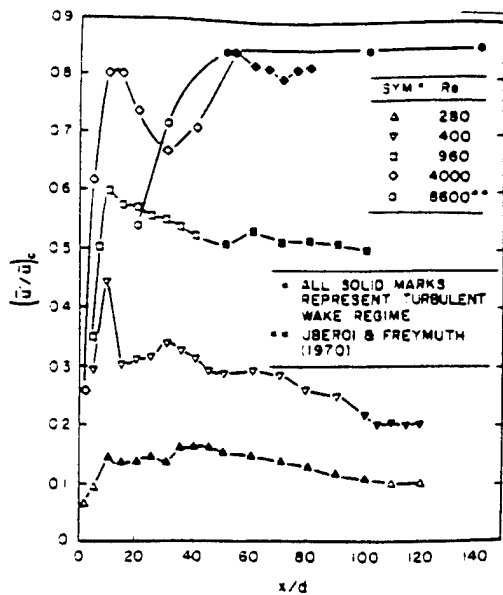
Fig. 6 Streamwise rms velocity fluctuations along the wake axis (Re = 280-8600).

the strongly directed near-wake region. Outside this region, the corrections are small except for the latter parts of the results for the wakes for $Re \leq 960$; corrected results for the turbulent wakes will be considered subsequently.

Present measurements of $(\bar{u}'/\bar{u})_c$ within the turbulent wake region at $Re = 4000$ are in reasonably good agreement with Uberoi and Freymuth[19] in Fig. 6: turbulence intensities are nearly constant at roughly 85% and the onset of this regime is in the range $x/d = 40$-60. Thus, within this regime, $\bar{u}'_c \sim (x - x_o)^{-1}$ from Eq. (2) as observed during a number of past studies. For $Re \leq 960$, however, turbulence intensities in the turbulent wake region progressively decrease with decreasing Re; nevertheless, even though these turbulence intensities are low in comparison to high Reynolds-number turbulent wakes, they still are comparable to values found in the actively turbulent flows, e.g., near the axis of turbulent jets and pipe flows.[21,22] Additionally, at these lower Reynolds numbers, there is a tendency for the turbulence intensity to decrease with increasing distance; this is particularly evident beyond the initial development region for $Re = 280$ (i.e., $x/d \geq 40$) where present measurements captured an extended turbulent wake region. Such behavior is expected as the turbulent wake decays toward transition to the laminar wake region and will be considered in more detail later.

Effects of vortex shedding on turbulence intensities in the near wake region also can be seen from the results plotted in Fig. 6. For present measurements at $Re = 4000$, the turbulence intensity reaches a peak near $x/d = 10$, due to strong effects of vortex shedding, and then decreases as the vortex pattern decays; subsequently, the development of wake turbulence causes the turbulence intensity to increase again and finally become nearly constant in the self-preserving wake region (this latter portion corresponding to behavior seen by Uberoi and Freymuth[19] at comparable Re). With strong effects of vortex shedding at low Re, e.g., $Re = 960$ and 40, the peak in turbulence intensity due to vortex shedding still is evident near the sphere; however, the intensity subsequently decays monotonically to conditions in the turbulent wake region. For $Re = 40$, the maximum turbulence intensity due to vortex shedding is largest in comparison to values in the turbulent wake region, roughly 2.5 times larger; thus, the greater decay required to reach turbulent wake conditions probably accounts for the larger x/d required to reach self-preserving turbulent wake conditions, as noted earlier. Finally, when vortex shedding is weak ($Re = 280$) there is no peak in the turbulence intensity

prior to the turbulent wake region and the onset of this region (with respect to the mean velocity distribution) occurs close to the sphere. However, turbulence still develops near the sphere, reaching a maximum intensity near $x/d = 40$, which is representative of the development region for high Reynolds-number turbulent wakes.[19]

The character of the decay of turbulence during approach to transition from turbulent to laminar wake behavior (with respect to mean velocities) is illustrated in Fig. 7. Present data on this figure has been corrected for ambient disturbances in the usual manner, i.e., $\bar{u}_c'^2 = \bar{u}_{cm}'^2 - \bar{u}_\infty'^2$, where $\bar{u}_{cm}'^2$ is the initial measured value and $\bar{u}_\infty'^2$ is the bath disturbance level prior to traversing the sphere. The results involve turbulence intensity at the wake axis plotted as a function of the local wake Reynolds number. The findings of Carmody[17] and Uberoi and Freymuth[19] a high wake Reynolds numbers are shown on the plot along with present results at moderate wake Reynolds numbers. These measurements involve fully developed turbulent wake conditions observed at $x/d \geq 40$ for Uberoi and Freymuth[19] and present tests, and at $x/d = 15$ for the high Reynolds-number results of Carmody.[17]

Taken together, the results illustrated in Fig. 7 suggest a reasonable correlation of wake turbulence properties in terms of the wake Reynolds number. For $Re_w > 70$, turbulence intensities along the axis are nearly constant with $\bar{u}_c'/\bar{u}_c$ in the range 0.85-0.92. At lower wake Reynolds numbers, however, turbulence intensities rapidly decrease (in terms of Re_w) in the final decay period as conditions for transition to a laminar wake are approached. Several proposals for the decay of turbulence energy in the final decay period have been made[24-27]; present results are in reasonable agreement with estimates for axisymmetric wakes,[25,27] where $\bar{u}'^2 \sim t^{-5/2}$. Noting that $x \sim U_t t$ for the fully developed turbulent wake region ($x/d \geq 40$) then yields the following relationship between turbulence intensity and local wake Reynolds number, using Eqs. (2) and (4):

$$(\bar{u}'/\bar{u})_c = C \, Re_w^{7/4} \qquad (11)$$

The best fit of present data ($10 < Re_w < 30$) yields $C = 1.3 \times 10^{-3}$ with a standard deviation of 4×10^{-4}.

The best-fit correlation of Eq. (11) is plotted in Fig. 7, where it is seen to provide a reasonable fit of present measurements for various values of Re and $10 \leq Re_w \leq 30$. If the same decay law was adopted from the laminar wake region, Eqs. (5) and (7) yield $(\bar{u})_c \sim Re_w^3$, which implies a much slower decay rate in terms of Re_w for laminar than turbulent wakes. Unfortunately, experimental evaluation of the transition of velocity fluctuations from turbulent to laminar wake behavior was not possible due to limitations of experimental uncertainties. Finally,
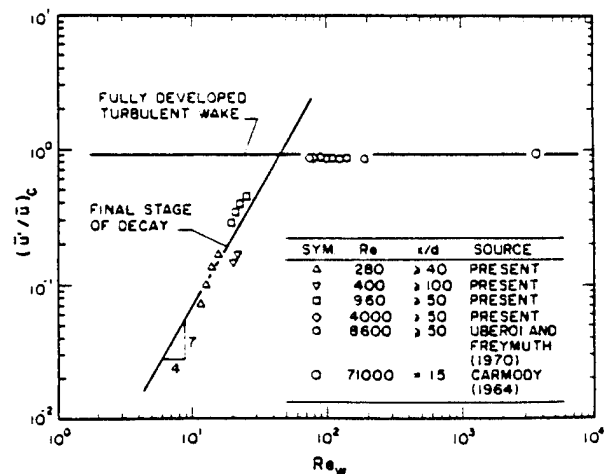

Fig. 7 Streamwise turbulence intensities along the axis as a function of wake Reynolds number in the turbulence wake region ($Re = 280$ -71,000).
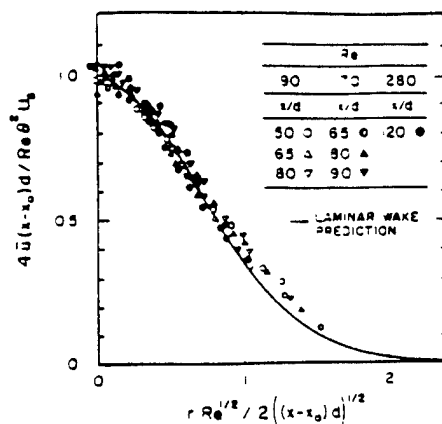
Fig. 8 Correlation of radial profiles of mean streamwise velocities in the laminar wake region ($Re = 90-280$).

the alternative final decay behavior proposed by Tan and Ling,[26] $\bar{u}'^2 \sim t^{-2}$, yields $(\bar{u}'/\bar{u})_c \sim Re_\theta^2$ and Re_w in the laminar and turbulent wake regions, the latter implying a much slower rate of decay than present observations.

Laminar Wake Region

The radial profiles of mean streamwise velocities in the laminar wake region are illustrated in Fig. 8. Results are shown for $Re = 90$, 170, and 280 for x/d in the range 50–120, plotted according to the similarity relationships of Eqs. (5) and (6) with $x_o/\theta = 1$. The measurements do not extend to the edge of the flow because low velocities in this region precluded results within the experimental uncertainties specified earlier. Over the range considered, however, the measurements agree with Eqs. (5) and (6) within experimental uncertainties in spite of the relatively high turbulence levels and the slow rate of decay of turbulence. An explanation for this behavior is that turbulence in the final decay period is not connected over the flow cross section similar to high Reynolds-number turbulent wakes; instead, it involves noninteracting localized regions of decaying turbulence (called turbulence spots, stratified turbulence, or dilute vortex streaks).[24-27] The absence of connectedness prevents mixing (entrainment or engulfment of ambient fluid) by large-scale turbulence structures that extend over a significant portion of the width of the wake, characteristic of high Reynolds-number turbulent wakes. Then, the overall mixing is dominated by laminar viscous effects so that mean velocity distributions adjust accordingly with the decaying turbulence spots only mildly affecting flow properties.

Conclusions

The major conclusions of the study are as follows:

1) The properties of the recirculation zone on the downstream side of the sphere were similar to earlier observations[7-16]: the recirculation zone was stable and symmetric for $Re \leq 200$, stable and unsymmetric for $200 < Re < 280$, and unstable with vortex shedding present for $Re \geq 280$.

2) The wakes exhibited three regions: a fast-decay wake region near the sphere that only was observed when vortex shedding was present, followed in succession by turbulent and laminar wake regions.

3) Mean velocities within the turbulent wake region scaled according to similarity predictions for self-preserving turbulent wakes, Eqs. (2), (3) or (8), (9), even though turbulence intensities along the axis varied in the range 10–85% and vortex shedding was present or absent. The main effect of vortex shedding on the turbulent wake region was to defer its onset, by an order of magnitude, due to the presence of the fast-decay wake region.

4) Transition from the turbulent to the laminar wake region occurred where similarity estimates of mean streamwise veloc-

ities along the axes for laminar and turbulent wakes were the same, Eq. (10). This corresponded to $Re_w = 10$.

5) Within the fully developed turbulent wake region ($x/d \geq 40$), $(\bar{u}'/\bar{u})_c = 85\%$ for $Re_w > 70$, typical of high Reynolds-number axisymmetric wakes; however, as conditions for transition to laminar wakes were approached, $(\bar{u}'/\bar{u})_c \sim Re_w^{-4}$, which is consistent with the final decay period of turbulence in axisymmetric wakes.[25,27]

6) Even though velocity fluctuations in the laminar wake region were significant, mean velocity distributions scaled according to laminar similarity predictions, Eqs. (6) and (7). This is plausible because turbulence in the final decay period involves isolated turbulent spots so that overall mixing is not controlled by the connected large-scale structures found in turbulent wakes; instead, mixing is dominated by laminar viscous effects and the mean velocity distributions adjust accordingly.

References

[1]Parthasarathy, R. N., and Faeth, G. M., "Turbulence Modulation in Homogeneous Dilute Particle-Laden Flows," *Journal of Fluid Mechanics*, Vol. 220, Nov. 1990, pp. 485–514.

[2]Mizukami, M., Parthasarathy, R. N., and Faeth, G. M., "Particle-Generated Turbulence in Homogeneous Dilute Dispersed Flows," *International Journal of Multiphase Flow*, Vol. 18, No. 3, May 1992, pp. 397–412.

[3]Torobin, L. B., and Gauvin, W. H., "Fundamental Aspects of Solids-Gas Flow, Part I: Introductory Concepts and Idealized Sphere Motion in Viscous Regime," *Canadian Journal of Chemical Engineering*, Vol. 37, No. 4, Aug. 1959, pp. 129–141; also "Part II: The Sphere Wake in Steady Laminar Fluids," Vol. 37, No. 5, Oct. 1959, pp. 167–176; also "Part V: The Effects of Fluid Turbulence on the Particle Drag Coefficient," Vol. 38, No. 6, Dec. 1960, pp. 189–200.

[4]Pruppacher, H. R., LeClair, B. P., and Hamielec, A. E., "Some Relations Between Drag and Flow Pattern of Viscous Flow Past a Sphere and a Cylinder at Low and Intermediate Reynolds Numbers," *Journal of Fluid Mechanics*, Vol. 44, Pt. 4, Dec. 1970, pp. 781–790.

[5]Rimon, Y., and Cheng, S. I., "Numerical Solution of a Uniform Flow Over a Sphere at Intermediate Reynolds Numbers," *Physics of Fluids*, Vol. 12, No. 5, 1969, pp. 949–959.

[6]Roos, F. W., and Willmarth, W. W., "Some Experimental Results on Sphere and Disk Drag," *AIAA Journal*, Vol. 9, No. 2, 1971, pp. 285–291.

[7]Magarvey, R. H., and Bishop, R. L., "Wakes in Liquid-Liquid Systems," *Physics of Fluids*, Vol. 4, No. 7, 1961, pp. 800–805.

[8]Magarvey, R. H., and MacLatchy, C. S., "Vortices in Sphere Wakes," *Canadian Journal of Physics*, Vol. 43, Sept. 1965, pp. 1649–1656.

[9]Willmarth, W. W., Hawk, N. E., and Harvey, R. L., "Steady and Unsteady Motions and Wakes of Freely Falling Disks," *Physics of Fluids*, Vol. 7, No. 2, 1964, pp. 197–208.

[10]Goldberg, A., and Florsheim, B. H., "Transition and Strouhal Number for the Incompressible Wake of Various Bodies," *Physics of Fluids*, Vol. 9, No. 1, 1966, pp. 45–50.

[11]List, R., and Hand, M. J., "Wakes of Freely Falling Water Drops," *Physics of Fluids*, Vol. 14, No. 8, 1971, pp. 1648–1655.

[12]Viets, H., "Accelerating Sphere-Wake Interaction," *AIAA Journal*, Vol. 9, No. 10, 1971, pp. 2087–2089.

[13]Calvert, J. R., "Some Experiments on Flow Past a Sphere," *Aeronautical Journal of the Royal Aeronautical Society*, Vol. 76, April 1972, pp. 248–250.

[14]Achenbach, E., "Vortex Shedding from Spheres," *Journal of Fluid Mechanics*, Vol. 62, Pt. 2, Jan. 1974, pp. 209–221.

[15]Nakamura, I., "Steady Wake Behind a Sphere," *Physics of Fluids*, Vol. 19, No. 1, 1976, pp. 5–8.

[16]Pao, H.-P., and Kao, T. K., "Vortex Structure in the Wake of a Sphere," *Physics of Fluids*, Vol. 20, No. 2, 1977, pp. 187–191.

[17]Carmody, T., "Establishment of the Wake Behind a Disk," *Journal of Basic Engineering*, Vol. 87, No. 4, Dec. 1964, pp. 869–883.

[18]Hwang, N. H. C., and Baldwin, L. V., "Decay of Turbulence in Axisymmetric Wakes," *Journal of Basic Engineering*, Vol. 88, No. 1,

March 1966, pp. 261-268.

[19]Uberoi, M. S., and Freymuth, P., "Turbulent Energy Balance and Spectra of the Axisymmetric Wake," *Physics of Fluids*, Vol. 13, No. 9, 1970, pp. 2205-2210.

[20]Chevray, R., "The Turbulent Wake of a Body of Revolution," *Journal of Basic Engineering*, Vol. 90, No. 2, June 1968, pp. 275-284.

[21]Tennekes, H., and Lumley, J. L., *A First Course in Turbulence*, MIT Press, Cambridge, MA, 1972, pp. 113-124.

[22]Hinze, J. O., *Turbulence*, 2nd ed., McGraw-Hill, New York, 1975, pp. 496-581.

[23]Schlichting, H., *Boundary Layer Theory*, 7th ed., McGraw-Hill, New York, 1977, pp. 234, 235, and 599.

[24]Batchelor, G. K., and Townsend, A. A., "Decay of Turbulence in the Final Period," *Proceedings of the Royal Society (London)*, Vol. A194, No. 8, Nov. 1948, pp. 527-543.

[25]Phillips, O. M., "Final Period of Decay of Non-Homogeneous Turbulence," *Proceedings of the Cambridge Philosophical Society*, Vol. 52, Pt. I, Jan. 1956, pp. 135-151.

[26]Tan, H. S., and Ling, S. C., "Final Stage of Decay of Grid-Produced Turbulence," *Physics of Fluids*, Vol. 6, No. 12, 1963, pp. 1693-1699.

[27]Lee, D. A., and Tan, H. S., "Study of Inhomogeneous Turbulence," *Physics of Fluids*, Vol. 10, No. 6, 1967, pp. 1224-1230.

[28]Putnam, A., "Integrable Form of Droplet Drag Coefficient," *American Rocket Society Journal*, Vol. 31, No. 10, 1961, pp. 1467, 1468.

[29]Kürten, H., Raasch, J., and Rumpf, H., "Beschleunigung eines Kugelförmen Feststoffteilchens im Strömungsfeld Konstanter Geschwindigkeit," *Chemi-Ingenieur-Technik*, Vol. 38, No. 9, Jan. 1966, pp. 941-948.

[30]Townsend, A. A., *The Structure of Turbulent Shear Flow*, 2nd ed., Cambridge Univ. Press, Cambridge, England, 1976, Chap. 6.

Appendix E: Wu, J.-S. and Faeth, G.M. (1994) Sphere wakes at moderate Reynolds numbers in a turbulent environment. <u>AIAA J</u>. 32, 535-541

Sphere Wakes at Moderate Reynolds Numbers in a Turbulent Environment

J.-S. Wu and G. M. Faeth

Sphere Wakes at Moderate Reynolds Numbers in a Turbulent Environment

J.-S. Wu* and G. M. Faeth†

University of Michigan, Ann Arbor, Michigan 48109

The structure of sphere wakes in a turbulent environment was measured over the following test range: sphere Reynolds numbers from 135 to 1560, ambient turbulence intensities of roughly 4%, ratios of streamwise spatial integral scales to sphere diameters of 11–59, and ratios of Kolmogorov length scales to sphere diameters of 0.08–0.80. At these conditions, some phenomena observed for sphere wakes at comparable Reynolds numbers in nonturbulent environments were suppressed, like the fast-decaying and self-preserving turbulent wake regions: instead, while the wakes were turbulent, their mean streamwise velocities scaled like self-preserving laminar wakes but with enhanced viscosities due to turbulence. Effective turbulent viscosities were relatively independent of position and ratios of integral length scales and Kolmogorov microscales to sphere diameters; however, they progressively increased with sphere Reynolds numbers. Low and high Reynolds number regimes were observed, separated by a transition regime involving sphere Reynolds numbers in the range from 300 to 600, which was associated with conditions where effects of vortex shedding were prominent in the temporal power spectra measured in the near-wake region.

Nomenclature

C_d	= drag coefficient
D	= pipe diameter, m
d	= sphere diameter, m
$E_v(f)$	= power spectral density of cross-stream velocity fluctuations, m^2/s
f	= frequency, s^{-1}
f_o	= vortex shedding frequency, s^{-1}
ℓ	= characteristic wake width, Eq. (3), m
ℓ_K	= Kolmogorov length scale, m
Re	= sphere Reynolds number, $d\bar{U}_\infty/\nu$
Re_D	= pipe flow Reynolds number, $D\bar{U}_\infty/\nu$
Re_t	= turbulence Reynolds number, $d\bar{U}_\infty/\nu_t$
Re_w	= local wake Reynolds number, $\ell \bar{u}_c/\nu_t$
r	= radial position. m
St	= Strouhal number, $f_o d/\bar{U}_\infty$
$\bar{U}_t$	= wake-scaling velocity, Eq. (5), m/s
$\bar{U}_\infty$	= mean relative velocity of sphere, m/s
$\bar{u}$	= mean streamwise velocity, m/s
$\bar{u}'$	= rms streamwise velocity fluctuation, m/s
$\bar{v}'$	= rms cross-stream velocity fluctuation, m/s
x	= streamwise distance from center of sphere, m
Λ_u	= streamwise integral length scale, m
ν	= kinematic viscosity, m^2/s
ν_t	= turbulence kinematic viscosity, m^2/s
τ_u	= temporal integral scale of streamwise velocity fluctuations, s

Subscripts

c	= centerline value
o	= virtual origin condition
∞	= ambient condition

Introduction

THE structure and mixing properties of sphere wakes are important fundamental problems having numerous applications,

including the properties of dispersed multiphase flows like sprays, rainstorms. and particle-laden flows. Recent work on turbulence generation by dispersed phases in multiphase flows has highlighted the need for more information about sphere wakes at intermediate sphere Reynolds numbers ($10 < Re < 1000$).[1,2] This prompted earlier measurements of the structure of sphere wakes at intermediate Reynolds numbers in nonturbulent environments.[3] The objective of the present investigation was to extend this work to sphere wakes in turbulent environments that are more representative of conditions within practical dispersed multiphase flows.

Past research on the flow near spheres and in sphere wakes in nonturbulent environments is reviewed by Wu and Faeth[3] and the references cited therein. Studies of the near wake of spheres have established the nature of the recirculation zone and the characteristics of vortex shedding.[3-12] Three wake regions have been identified: a fast-decay wake region, observed only when vortex shedding is present. followed in succession by turbulent and laminar wake regions.[3] Mean streamwise velocity distributions are self-preserving in the turbulent and laminar wake regions and scale according to classical similarity theories.[13-19] The transition between the turbulent and laminar wake regions corresponds to a local wake Reynolds number. $Re_w \approx 10$: as the laminar wake region is approached, turbulence intensities along the axis decay proportional to $Re_w^{7/4}$, which agrees with the scaling predicted for the final turbulence decay period of axisymmetric wakes.[20,21] Clearly, sphere wakes in nonturbulent environments exhibit a rich variety of flow phenomena: however. the relevance of this behavior to wakes in turbulent environments is questionable. There also have been many studies of the effects of ambient turbulence on drag and interphase heat and mass transfer and the structure of boundary layers along surfaces (see Refs. 22–25 and the references cited therein). However. comparable studies of effects of ambient turbulence on wake properties are limited and do not include consideration of the wakes of axisymmetric objects like spheres.

Based on these observations. the present experimental investigation was undertaken to better understand axisymmetric wakes in turbulent environments. The study involved laser velocimetry measurements of mean velocities and turbulence properties in sphere wakes within the stationary turbulence field near the axis of fully developed turbulent pipe flow. This tactic avoids the complications of streamwise variations of ambient turbulence properties due to the relatively rapid decay of grid-generated turbulence.[23] The ranges of test variables were as follows: Re from 135 to 1560. ambient turbulence intensities of roughly 4%, Λ_u/d of 11–59. and

r_K/d of 0.08–0.80. These conditions are representative of dispersed multiphase flows, which typically involve intermediate Reynolds numbers and larger integral scales than the characteristic size of dispersed-phase elements.[1-3,26]

Experimental Methods

Apparatus

The apparatus consisted of a turbulent flow of air within a long horizontal pipe, with the test sphere mounted on a traversing system near the axis at the downstream end of the pipe. Wake properties were measured using a rigidly mounted laser velocimeter, whereas pipe flow properties were measured using a traversible laser velocimeter. The pipe flow was produced by a variable speed blower. The blower was followed by a honeycomb flow straightener and four screens to provide a nonswirling uniform flow at the pipe inlet. A smooth PVC pipe having an inside diameter of 300 mm and a length of 16 m was used to provide the fully developed turbulent pipe flow. Pipe length-to-diameter ratios at the test location were never less than 52, which is sufficient to provide fully developed turbulent pipe flow in the region of the wakes.[18,19]

The test spheres were polished plastic balls (±1% radius tolerance, sphericity within 1%, and surface roughness less than 0.3%) with diameters in the range 1.2–5.6 mm. The spheres were mounted on thin stainless steel wires (51-μm diameter for $d \leq 1.6$ mm and 127-μm diameter for $d \geq 3.0$ mm), which passed through their centers and were sealed with epoxy. The wires were mounted in tension between two struts passing near the top and bottom of the pipe to prevent sphere vibrations. Tests with no spheres present showed that the disturbances of the wire support system were negligible in comparison with effects of the sphere wakes. The optical system for the wake velocity measurements was rigid; therefore, the spheres were traversed using a stepping motor driven linear positioner in the cross-stream direction (positioning accuracy of 5 μm) and a manual linear positioner in the streamwise direction (positioning accuracy of 500 μm). Alignment of the spheres over the full streamwise traverse was facilitated using a small helium-neon laser mounted permanently with its beam directed along the pipe axis, yielding a maximum uncertainty of the cross-stream position of 1 mm at x/d of about 100, with proportionately smaller uncertainties at locations nearer to the sphere.

Instrumentation

Wake structure measurements involved a dual-beam, forward-scatter, frequency-shifted laser velocimeter with the measuring volume centered on the pipe axis, 30 mm downstream from its end. The measurements were based on the 514.5 nm line of an argon-ion laser with an optical power of 500 mW. The sending optics included a 3.75:1 beam expander that yielded a measuring volume having a diameter of 50 μm and a length of 300 μm. The flow was seeded with oil drops (1 μm nominal diameter) at the inlet of the blower to yield data rates in the range 0.5–2 kHz, depending on the mean velocity of the pipe flow. Velocities were found from the low-pass filtered analog output of a burst counter signal processor. Data were collected using a 12-bit analog/digital converter operating at a frequency comparable to the data rate with the break frequency of the filter set at one-half the sampling rate to control alias signals. Mean and fluctuating velocities were obtained using sampling periods of 120 s, whereas temporal power spectra were measured using sampling periods of 300 s. Experimental uncertainties (95% confidence) largely were controlled by sampling limitations to yield the following values for $\bar{u}/\bar{U}_\infty > 0.1$ (and inversely proportional to $\bar{u}$ thereafter): mean velocities, less than 5%, rms velocity fluctuations less than 10%, and temporal power spectra less than 20%. All measurements were repeatable within these ranges over a period of testing of several months.

A traversible dual-beam, forward-scatter, frequency-shifted laser velocimeter was used to measure the structure of the pipe flow, based on the 514.5-nm line of an argon-ion laser and using a fiber-optic cable to transmit the beam to the sending optics. The effective optical power at the measuring volume, accounting for losses in the fiber-optic cable, was 150 mW. The optical arrangement yielded a measuring volume diameter of 100 μm and a length of 1200 μm. Flow seeding, data acquisition, data processing, experimental uncertainties, and repeatability for the pipe flow measurements were the same as the wake structure measurements.

Test Conditions

Test conditions are summarized in Table 1, with the entries appearing in the order of increasing sphere Reynolds numbers. Mean streamwise velocities at the axis of the pipe flow were in the range 1.56–5.35 m/s to avoid problems of natural convection disturbances at very low velocities. Thus, relatively small sphere diameters, 1.2–5.6 mm, were required to consider the intermediate Reynolds number range of interest. This yields blockage ratios less than 0.0035% due to the presence of the sphere, which is negligible. Pipe flow Reynolds numbers were in the range from 3×10^4 to 1.003×10^5, which yielded streamwise pressure gradients of 0.1–1 Pa/m. Tests at similar sphere Reynolds numbers but with varying pipe flow Reynolds numbers indicated negligible effects on the flow properties of streamwise pressure gradients in this range.

The ambient flow properties summarized in Table 1 are averages over the region where wake structure measurements were made, e.g., $2r/D \leq 0.2$. In general, pipe flow properties agreed with

Table 1 Summary of test properties[a]

Re	d, mm[b]	$\bar{U}_\infty$, m/s[c]	Re_D[c]	$\bar{u}'_\infty/\bar{U}_\infty$, %[c]	Λ_u/d	r_K/d[c]	C_d[d]	x_r/d	$\bar{U}_r/\bar{U}_\infty$	v_t/v	Re_t
135	1.2	1.82	34,100	3.9	59	0.80	0.95/1.05	1.9	1.85	2.4	56.4
170	1.6	1.66	31,100	4.0	45	0.63	0.86/0.86	1.8	1.77	2.6	65.6
215	1.2	2.91	54,600	3.8	58	0.60	0.79/0.79	1.5	1.50	3.5	61.0
240	1.6	2.40	45,000	3.8	44	0.49	0.76/0.76	1.7	1.53	3.7	64.8
300	3.0	1.56	30,000	4.2	24	0.27	0.70/0.63	1.5	1.35	4.3	69.0
305	1.6	3.00	56,300	3.9	43	0.40	0.69/0.60	1.1	1.13	5.0	60.5
315	1.2	4.25	79,700	3.8	55	0.40	0.69/0.60	1.1	1.10	5.3	59.0
400	1.2	5.35	100,300	3.8	53	0.35	0.63/0.63	0.8	0.95	8.3	48.0
410	1.6	4.04	75,800	3.9	41	0.32	0.63/0.49	0.9	0.87	7.3	56.3
415	3.0	2.19	41,100	4.0	24	0.21	0.63/0.63	1.0	0.95	8.5	48.6
530	1.6	5.28	99,000	3.7	40	0.27	0.58/0.58	0.8	0.84	11.5	46.1
610	3.0	3.22	60,400	3.9	23	0.20	0.56/0.71	0.8	0.80	16.8	36.3
610	5.6	1.82	34,100	3.9	13	0.17	0.56/0.56	0.6	0.65	17.8	34.3
930	3.0	4.59	86,100	4.0	21	0.15	0.50/0.64	0.7	0.68	27.3	34.1
930	5.6	2.70	50,600	3.9	12	0.12	0.50/0.59	0.5	0.52	27.9	33.3
1560	5.6	4.61	86,000	3.9	11	0.08	0.45/0.45	0.5	0.49	44.3	35.2

[a]Sphere mounted near the axis of fully developed turbulent pipe flow in air ($v = 16$ mm²/s) within a 300-mm inside diameter smooth pipe. Streamwise pressure gradients in the range 0.1–1 Pa/m.
[b]Nylon ball with a 51-μm diam mounting wire for $d = 1.2$ and 1.6 mm; polycarbonate ball with a 127-μm diam mounting wire for $d \geq 3.0$ mm.
[c]Measured average value over the region $2r/d \leq 0.2$.
[d]Value computed from Kürten et al.[27] / value computed from self-preserving laminar-like mean velocity profiles.

existing measurements in the literature within experimental uncertainties.[29,30] Turbulence intensities were not constant due to the present relatively low values of Re_D, yielding values of 3.7–4.2% over the test range. Streamwise integral length scales were found using Taylor's hypothesis, $\Lambda_u = \bar{U}_\infty \tau_u$, with τ_u found from measurements of the temporal correlation of streamwise velocity fluctuations.[18] The resulting measured values of streamwise integral length scales were in the range 64–72 mm, decreasing with increasing Re_D. Thus, integral length scales generally were an order of magnitude larger than the sphere diameters, $\Lambda_u/d = 11$–59, which is typical of dispersed phases in turbulent multiphase flows.[26] Kolmogorov scales were taken to be $\ell_K = \Lambda_u/(\bar{u}_\infty \Lambda_u/\nu)^{3/4}$ from Tennekes and Lumley.[17] The resulting values were in the range 0.42–1.00 mm, generally decreasing with increasing Re_D. Thus, Kolmogorov length scales were generally smaller than the sphere diameters, $\ell_K/d = 0.08$–0.80.

The drag coefficients of the spheres for the various sphere Reynolds numbers were computed in two ways: using the correlation of Kürten et al.[27] for solid spheres in nonturbulent environments and using the measured mean velocity defect within the wake. The two estimates of C_d are in reasonably good agreement in Table 1, with an average error of 6% over all of the measurements. The fact that ambient turbulence intensities of roughly 4% have little effect on the drag coefficient is not surprising for the present relatively low values of Re, based on existing measurements in the literature.[22]

Wake Similarity

Remarkably, the present wakes in turbulent environments exhibited extended regions where they behaved like self-preserving laminar wakes with constant viscosities. Effects of turbulence were manifested by enhanced viscosities, in comparison with molecular viscosities, which varied with the sphere Reynolds number. To illustrate these relationships, the scaling of self-preserving laminar wake properties will be summarized in the following.

Classical similarity analysis of self-preserving round laminar wakes with constant viscosities yields the following expression for streamwise velocities[19]:

$$\bar{u}/\bar{U}_\infty = (C_d Re_t/32)[d/(x-x_o)]\exp(-r^2/2\ell^2) \quad (1)$$

where

$$Re_t = d\bar{U}_\infty/\nu_t \quad (2)$$

The characteristic wake width ℓ in Eq. (2) is given by

$$\ell/d = [2(x-x_o)/d\,Re_t]^{1/2} \quad (3)$$

Here, and in the following, an inertial reference frame has been adopted where the velocities of both the sphere and the wake are relative to the ambient fluid. In addition, the present turbulent flow is considered by replacing the steady velocities of laminar wakes with the mean velocities of the turbulent wakes, $\bar{u}$ and $\bar{U}_\infty$, and the laminar kinematic viscosity ν by the effective turbulent viscosity ν_t. From Eqs. (1) and (3), the effective local wake Reynolds number for the laminar-like turbulent wake region becomes

$$Re_w = \ell\bar{u}_c/\nu_t = (C_d Re_t^{1/2}/16)/[2(x-x_o)/d]^{1/2} \quad (4)$$

Thus, Eqs. (1), (3), and (4) imply $\bar{u}/\bar{U}_\infty$, ℓ/d, and Re_w are proportional to $(x-x_o)^{-1}$, $(x-x_o)^{1/2}$ and $(x-x_o)^{-1/2}$, respectively, in laminar-like turbulent wakes, as long as ν_t is independent of position within the wake.

The formulation of Eqs. (1–4) is somewhat inconvenient because ν_t for laminar-like turbulent wakes is not known a priori, unlike ν for laminar wakes. Thus, it was helpful to define a wake-scaling velocity $\bar{U}_t$ as follows:

$$\bar{U}_t/\bar{U}_\infty = C_d Re_t/32 \quad (5)$$

Then, substituting Eq. (5) into Eq. (1) yields the following expression for streamwise mean velocities within laminar-like turbulent wakes:

$$\bar{u}/\bar{U}_t = [d/(x-x_o)]\exp(-r^2/2\ell^2) \quad (6)$$

where $\bar{U}_t$ is found from the value of $\bar{u}$ where the extrapolation of the velocity variation in the self-preserving region reaches the intercept, $(x-x_o)/d = 1$.

Results and Discussion

Vortex Shedding

Similar to sphere wakes in nonturbulent environments,[3] flow behavior was modified substantially by the presence of vortex shedding from the sphere. Thus, the onset and properties of vortex shedding from the spheres in the present turbulent environment will be considered first.

Conditions for the onset of vortex shedding, and vortex-shedding frequencies thereafter, were found from measurements of temporal power spectra in the near wake, similar to Durão et al.[31] This involved measurements of the temporal power spectra of streamwise and cross-stream velocity fluctuations at the axis and $x/d = 4$, where onset conditions were most easily observed. Although effects of vortex shedding were observed for both velocity components, the following discussion will be limited to the temporal spectra of $\bar{v}_c'$ which exhibited greater effects of vortex shedding.

Some typical temporal power spectra of cross-stream velocity fluctuations at $r/d = 0$ and $x/d = 4$ are illustrated in Fig. 1. Results are illustrated for sphere diameters of 1.6 and 3 mm, although findings for other sphere diameters were similar. At low Reynolds numbers when vortex shedding is absent, e.g., at $Re = 180$, $E_v(f)$ decays monotonically with increasing frequency. The result of vortex shedding, however, clearly is indicated by a spike in $E_v(f)$ for $fd/\bar{U}_\infty$ on the order of 0.1. The magnitude of the spike progressively decreases with increasing Re, because effects of turbulence in the near-wake region tend to increase with increasing Re (this will be discussed in more detail in connection with Fig. 7). Thus, at the highest Reynolds number illustrated in Fig. 1, the effect of vortex shedding is limited to a rather small peak in $E_v(f)$ near $fd/\bar{U}_\infty = 0.1$. The behavior seen in Fig. 1 for $E_v(f)$ is qualitatively similar to $E_u(f)$ and for other positions in the near wake, although the magnitude of the peak and its rate of decay with increasing Re was affected by position.

The onset of vortex shedding, based on the appearance of a peak in $E_v(f)$, occurred at Re in the range from 260 to 290 for sphere diameters on the range 1.2–3.0 mm. Thus, Re for the onset of vortex shedding for spheres in the present turbulent environments are not very different from earlier findings for spheres in nonturbulent environments. For example, the onset of vortex shedding in nonturbulent environments is reported at $Re = 280$ by Wu and Faeth,[3] 300 by Magarvey and MacLatchy,[5] 270 by Goldberg and Florsheim[6] and 300 by Sakamoto and Haniu.[11]

The frequencies of vortex shedding also were similar in nonturbulent and turbulent environments. This is illustrated in Fig. 2, where measurements of vortex-shedding frequencies, represented by the Strouhal number, $St = f_o d/\bar{U}_\infty$, are plotted as a function of Re. Aside from the present results for spheres in turbulent environments, and those of Marshall and Stanton[32] for a circular plate in a nonturbulent environment, all the results are for spheres in nonturbulent environments. Kim and Durbin[12] point out that there are two simultaneous modes of unsteadiness for $Re > 800$, which accounts for the double-valued behavior in this region. The high-frequency mode is associated with instability of the separating shear layer and is only observed for measurements near the sphere. The low-frequency mode extends to frequencies at the onset of vortex shedding and is associated with the large-scale instability of the wake; as a result, it is called the vortex-shedding mode.[12]

Present measurements were made near the axis at some distance from the sphere and only the vortex-shedding mode was observed. The results illustrated in Fig. 2 indicate a tendency for St for vortex
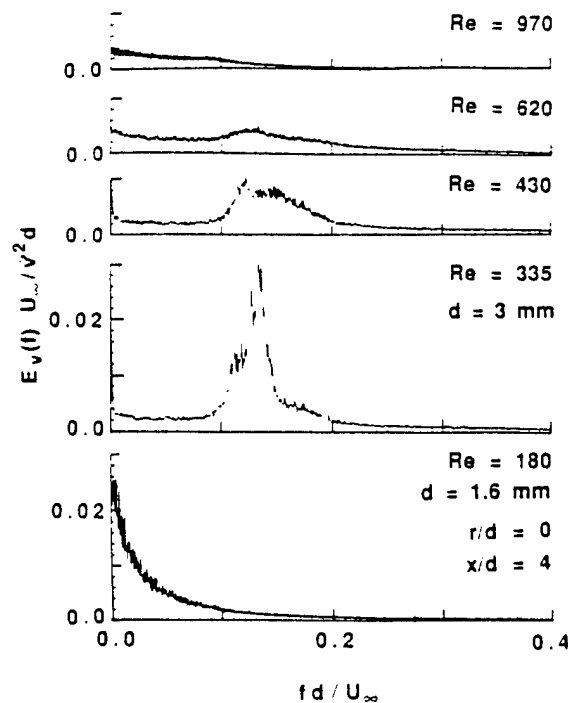
Fig. 1 Temporal power spectra of cross-stream velocity fluctuations in the near-wake region.

shedding to be slightly reduced in turbulent environments in comparison with nonturbulent environments. However, the reduction is not large in comparison to the bandwidth of the spectral peak; see Fig. 1. A somewhat unusual observation was the subharmonic observed near the onset of vortex shedding for the 1.6-mm-diam sphere, although subharmonics have been observed for shear layer instabilities in the past.[11,12]

Mean Velocities

Measurements of mean velocities along the axis suggested that there was an extended region where the wakes were self-preserving and exhibited laminar-like scaling. Thus, plots of $1/\bar{u}_c$ as a function of x/d were extrapolated to find the virtual origin, whereas the value of $\bar{u}_c$ at $(x - x_o)/d = 1$ yielded $\bar{U}_t$, based on Eq. (6). The resulting values of x_o/d and $\bar{U}_t/\bar{U}_\infty$ are summarized in Table 1. In general, the virtual origins were in the near-wake region, relatively close to the sphere, e.g., x_o/d of 0.5–1.9. The value of x_o/d progressively decreased as the Re increased. The ratio, $\bar{U}_t/\bar{U}_\infty$, was in the range 0.49–1.85, and also tended to decrease as Re increased.

The variation of mean streamwise velocities along the axis, $\bar{u}_c/\bar{U}_t$, is illustrated in Fig. 3 for all of the test conditions. The behavior of laminar-like wake scaling according to Eq. (6) is also shown on the plots. The measurements extend from the near-wake region, $(x - x_o)/d$ of 1–2, to $(x - x_o)/d$ of roughly 100. The measurements were terminated at large distances from the sphere where mean velocities became small and the experimental uncertainties stated earlier could not be maintained.

The measurements illustrated in Fig. 3 are grouped into three regimes based on behavior in the near-wake region. Measurements in all three regimes, however, clearly exhibit the scaling expected for laminar-like turbulent wakes at $(x - x_o)/d$ in the range of 8–100. The three regimes involve a low Reynolds number regime, $Re < 300$, a high Reynolds number regime, $Re > 600$, and a transition regime between these two. The low and high Reynolds number regimes involve similarity in terms of $\bar{u}_c/\bar{U}_t$ over the full range of $(x - x_o)/d$; however, values of $\bar{u}_c/\bar{U}_t$ are lower and higher, respectively, than the extrapolation of laminar-like turbulent wake behavior in the near-wake region $(x - x_o)/d < 8$. Behavior in the tran-

sition regime represents an evolution between these two limiting conditions, with similarity in terms of $\bar{u}_c/\bar{U}_t$ much less evident in the near-wake region. The onset of the transition regime at Re of about 300 coincides with conditions where vortex shedding begins. Thus, the changes of near-wake behavior seen in Fig. 3 are caused by effects of vortex shedding, analogous to behavior observed for spheres in nonturbulent environments.[3]

Beyond the near-wake region in Fig. 3, $(x - x_o)/d > 8$, mean velocities scale reasonably well according to the laminar-like turbulent wake correlation. This implies faster mixing rates as Re increases for the present variation of $\bar{U}_t/\bar{U}_\infty$ summarized in Table 1. For example, the values of $(x - x_o)/d$ where $\bar{u}_c/\bar{U}_\infty$ became small, say 1%, were in the range 24–96, progressively increasing with decreasing Re. Values of Re_x at this condition were roughly 1.4 for the low Reynolds number regime, and 0.6 for the high Reynolds number regime, with intermediate behavior in the transition regime. Thus, Re_x on the order of unity is representative of the end of the wake-mixing process for the present turbulent environment.

Given $\bar{U}_t$ and C_d for a particular sphere Reynolds number, Re_t can be computed from Eq. (5) and ν_t from Eq. (2). The resulting values of ν_t/ν and Re_t are summarized in Table 1. It is seen that ν_t/ν progressively increases with increasing Re, reflecting the faster mixing rates at higher Reynolds numbers. The corresponding values of Re_t exhibit a somewhat smaller rate of reduction as Re increases.

Given Re_t, the measured radial profiles of streamwise mean velocities can be plotted according to the scaling of self-preserving laminar-like turbulent wakes from Eqs. (1) and (3). These results are plotted in Fig. 4, along with the predictions of Eqs. (1) and (3). The measurements are grouped into low, transition, and high Reynolds number regimes as before. All the measurements are within the laminar-like turbulent wake region with x/d in the range 8–51. Measurements at larger x/d are not shown in Fig. 4 because experimental accuracy was limited over an appreciable fraction of the wake cross-section due to the small mean velocities in this region. Results already discussed in connection with Fig. 3, however, have shown proper scaling of centerline velocities for $(x - x_o)/d > 50$.

Although the measurements illustrated in Fig. 4 have been grouped into low, transition, and high Reynolds number regimes, results for all three regimes are essentially the same. For $\bar{u}/\bar{U}_\infty >$
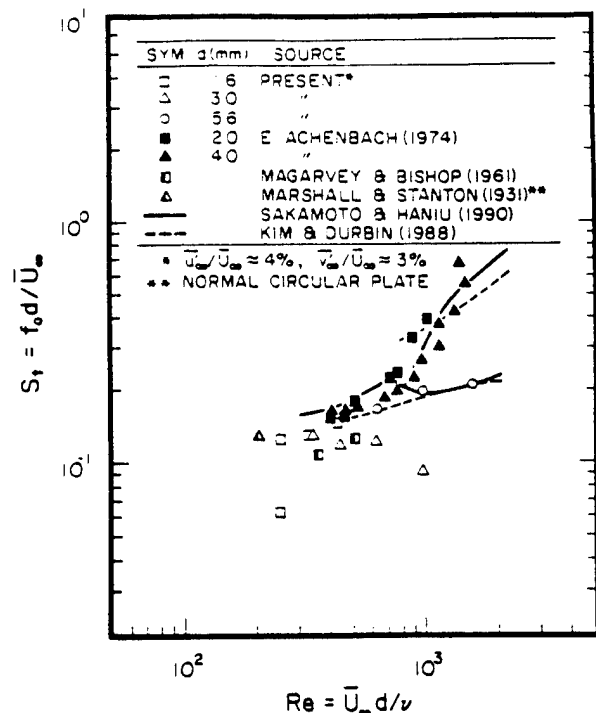

Fig. 2 Strouhal numbers of vortex shedding from the spheres.

0.1, the measurements agree with the predictions for self-preserving laminar-like turbulent wakes, Eqs. (1) and (3), within experimental uncertainties. Results near the edge of the flow exhibit a larger degree of scatter, which is attributed to larger experimental uncertainties of the velocity measurements in this region. Another factor limiting accuracy near the edge of the wakes is the approach of the sphere to the limits of the nearly constant ambient property region near the pipe axis. With laminar-like scaling for these wakes, the faster mixing at larger Reynolds numbers is reflected by increased values of the effective turbulent viscosity (see Table 1).

The value of the effective turbulent viscosity v_t clearly is the critical parameter needed to estimate mean streamwise velocities in the laminar-like turbulent wake region. The results illustrated in Figs. 3 and 4 indicate that v_t was relatively independent of position in the wake. However, v_t varied in a rather systematic fashion with respect to the sphere Reynolds number. Results illustrating this behavior appear in Fig. 5, where v_t/v is plotted as a function of Re for all of the present measurements.

Similar to behavior observed in Fig. 3 for the near-wake region, v_t/v in Fig. 5 exhibits distinct behavior in the low, transition, and high Reynolds number regimes. Over all three regimes, however, results for various sphere diameters overlap so that v_t/v can be correlated as a function of Re alone. This behavior suggests that length scale properties, like Λ_u/d and ℓ_K/d, have a relatively small effect on flow properties over the present test range, which is consistent with the apparently small variation of v_t/v with position in the wake. The variation of v_t/v with Re is nearly linear in the low and high Reynolds number regimes and can be represented by the following empirical fits:

$$v_t/v = 0.017\,Re, \qquad 135 < Re < 310 \qquad (7)$$

$$v_t/v = 0.029\,Re, \qquad 610 < Re < 1560 \qquad (8)$$

These results are only provisional for $\bar{u}'_\infty/\bar{U}_\infty$ of about 4%. In view of the vastly different behavior observed for spheres in nonturbulent environments[3] and the present turbulent environments,
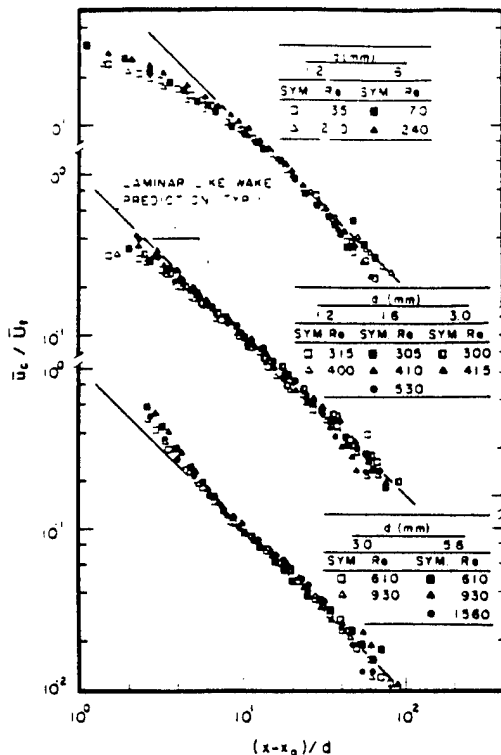
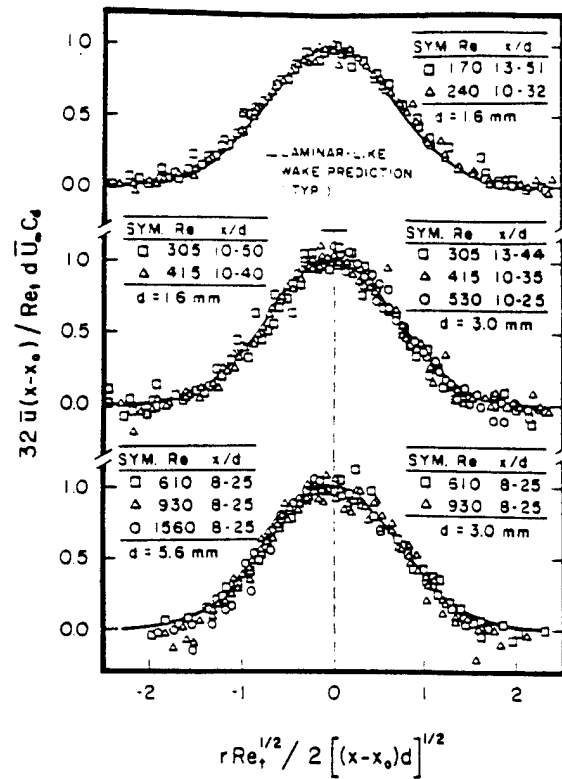Fig. 3 Mean streamwise velocities along the axis of the wakes.

Fig. 4 Correlation of radial profiles of mean streamwise velocities in the laminar-like turbulent wake region.
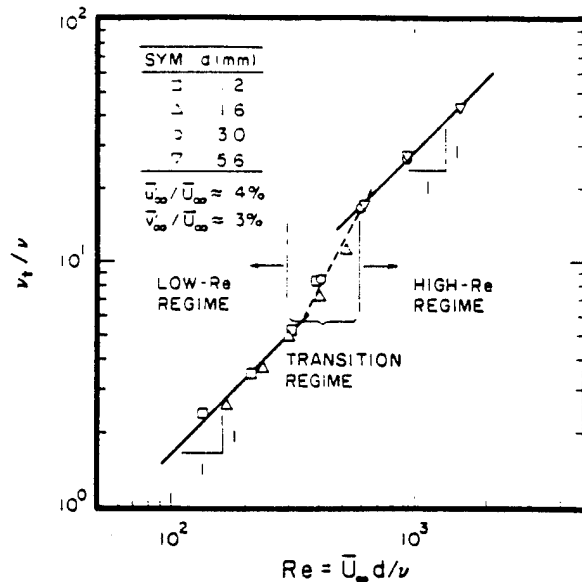
Fig. 5 Variation of turbulent viscosity with sphere Reynolds number.

effects of $\bar{u}'_\infty/\bar{U}_\infty$ on v_t/v certainly can be anticipated. Additionally, v_t/v should approach unity as Re becomes small so that Eq. (7) should not be used at Re below the range of the present measurements. The rate of increase of v_t/v with increasing Re is more rapid in the transition regime than the other two regimes and can be approximated by the following empirical expression:

$$v_t/v = 1.2 + 42\,(Re/1000)^2, \qquad 310 < Re < 610 \qquad (9)$$

The onset of the transition regime at Re of about 300 corresponds to the onset of vortex shedding for present conditions, as noted ear-
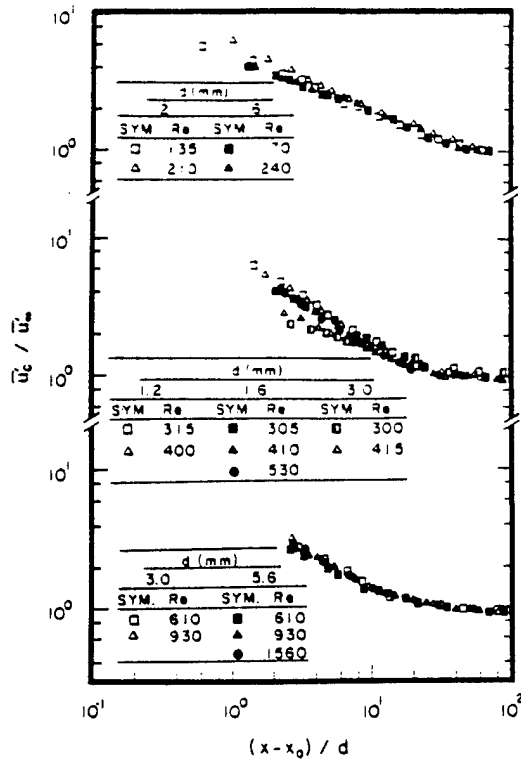
540   WU AND FAETH: WAKES IN A TURBULENT ENVIRONMENT

Fig. 6   Streamwise rms velocity fluctuations along the axis of the wakes.

Fig. 7   Cross-stream rms velocity fluctuations along the axis of the wakes.

lier. This suggests that vortex shedding is responsible for the more rapid growth of v_t/v with Re in the transition regime, with this growth period ending when the near-wake region becomes fully developed in the presence of vortex shedding, much like the near-wake mean velocity profiles illustrated in Fig. 3. Measured velocity fluctuations in the wakes tend to support this behavior and will be considered next.

Velocity Functions

Streamwise and cross-stream velocity fluctuations along the wake axis are plotted as functions of $(x - x_o)/d$ in Figs. 6 and 7. The velocity fluctuations have been normalized by the corresponding ambient rms velocity fluctuations, to indicate the degree of enhancement of turbulence levels within the wake. As before, the measurements have been grouped into low, transition, and high Reynolds number regimes. Aside from a few measurements in the near-wake region, the results are in the laminar-like turbulent wake region with $(x - x_o)/d$ in the range 8–100.

The streamwise velocity fluctuations, Fig. 6, are relatively independent of Re when normalized by $\bar{u}'_\infty$. In addition, results in all three Reynolds number regimes are essentially the same, aside from a somewhat increased degree of scatter in the near-wake region for the transition Reynolds number regime. Streamwise velocity fluctuations exhibit significant enhancement in the near wake, becoming 4–6 times greater than ambient turbulence levels. However, streamwise velocity fluctuations decrease monotonically with increasing streamwise distance and approach ambient turbulence levels at $(x - x_o)/d \approx 60$, which corresponds to the region where mean wake velocities at the axis approach ambient velocity fluctuation levels (cf. Fig. 3).

The behavior of $\bar{v}'_c/\bar{v}'_\infty$ in Fig. 7 differs from $\bar{u}'_c/\bar{u}'_\infty$ in Fig. 6. First of all, $\bar{v}'_c/\bar{v}'_\infty$ tends to vary with Re to a greater degree, even within each of the three Reynolds number regimes. The exception is a tendency to approach behavior independent of Reynolds number for $Re > 9 \times 10^2$, where $\bar{v}'_c = \bar{u}'_c$ and $\bar{v}'_c/\bar{v}'_\infty$ reaches its largest values at each streamwise position. In the low Reynolds number regime, there is a region in the near wake where the presence of the sphere reduces the cross-stream velocity fluctuations slightly from
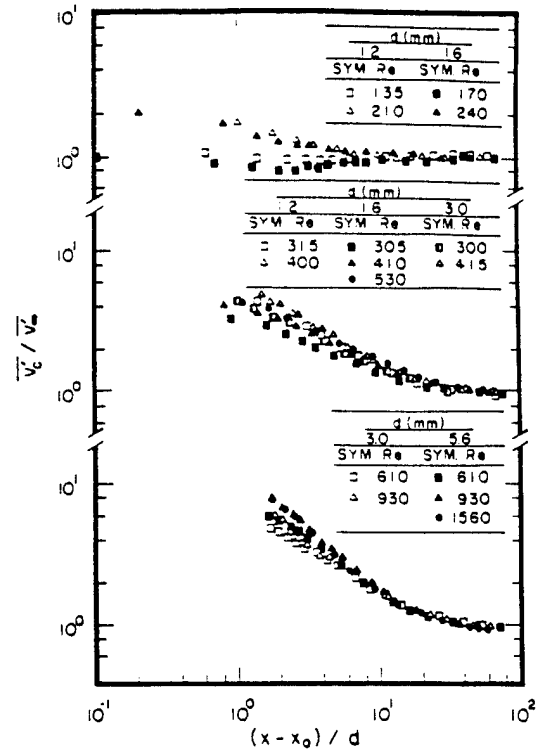
ambient values. This behavior probably involves effects of the recirculation zone behind the spheres,[3-9] however, the mechanism causing velocity fluctuations to be damped was not resolved. The onset of vortex shedding as the transition region is reached causes $\bar{v}'_c/\bar{v}'_\infty$ to increase substantially in the near-wake region. Subsequently, cross-stream velocity fluctuations progressively increase with increasing Re until they stabilize at $Re > 9 \times 10^2$, as discussed earlier.

The results of Figs. 6 and 7 indicate that turbulence levels within laminar-like turbulent wakes are substantially enhanced from ambient turbulence levels; thus, it is not surprising that v_t/v tends to vary with Re even when $\bar{u}'_\infty/\bar{U}_\infty$ is a constant. Furthermore, the relatively small values of $\bar{v}'_c/\bar{v}'_\infty$, approaching unity at the lowest Reynolds numbers, are consistent with relatively small effects of turbulence so that v_t/v approaches unity as well. Additionally, although, $\bar{v}'_c/\bar{v}'_\infty$ tends to increase with Re over the test range, the onset of vortex shedding initiates conditions where $\bar{v}'_c/\bar{v}'_\infty$ increases most rapidly, which also is consistent with the more rapid increase of v_t/v with Re in this region (cf. Fig. 5). Furthermore, it seems plausible that the period of unusually rapid growth of v_t/v should end when values of $\bar{u}'_c/\bar{u}'_\infty$ and $\bar{v}'_c/\bar{v}'_\infty$ become relatively independent of Re at high Reynolds numbers. Finally, values of $\bar{u}'_c/\bar{u}'_\infty$ and $\bar{v}'_c/\bar{v}'_\infty$ for different sphere diameters are essentially the same at given values of Re and $(x - x_o)/d$, supporting the idea that variations of Λ_u/d and ℓ_K/d have a relatively small effect on wake turbulence properties, and thus v_t/v, over the present test range.

Conclusions

The structure of the wakes of spheres in a turbulent environment was observed for $Re = 135$ to 1560. The turbulent environment involved conditions near the axis of fully developed turbulent pipe flow with turbulence intensities of roughly 4%, Λ_u/d in the range 11–59, and ℓ_K/d in the range 0.08–0.80. The major conclusions of the study are as follows:

1) The wakes were turbulent, but mean streamwise velocities scaled like self-preserving laminar wakes with enhanced viscosities due to the effects of turbulence.

2) The effective turbulent viscosities were independent of position in the wake and the length scale but increased with increasing Re, yielding v_t/v in the range 2.4–14.3. The v_t/v exhibited low and high Re regimes, with transition between these regimes for Re in the range 300 to 610 where the rate of increase of v_t/v with increasing Re was more rapid.

3) Streamwise and cross-stream velocity fluctuations along the wake axis reflected the different properties of the three sphere Reynolds number regimes, with behavior relatively independent of Re in the low and high Re regimes, whereas effects of Re were observed in the transition regime. Turbulence intensities in the near-wake region were lowest and highest in the low and high Re regimes, respectively, and exhibited small effects of the length scale ratios, Λ_u/d and ε_K/d, over the present test range.

4) The onset of the transition regime corresponded to the onset of vortex shedding from the spheres (Re of about 300) whereas transition regime ended when effects of vortex shedding no longer could be observed in the temporal power spectra of cross-stream velocity fluctuations in the near-wake region (at the axis for $x/d = 4$). Thus, the enhanced rates of turbulent mixing in the high Re regime appear to be associated with the development of effects of vortex shedding in the near-wake region.

5) The onset of vortex shedding at Re of about 300, the values of St associated with vortex-shedding frequencies, and the drag coefficients of the spheres were similar to observations for spheres in nonturbulent environments. This behavior is plausible due to the relatively large values of Λ_u/d of present tests so that the large-scale motions approached quasisteady behavior.

Effects of varying ambient turbulent intensities must still be resolved in order to address the properties of turbulence generation in dispersed multiphase flows like sprays.[1,2] Additionally, a broader range of Λ_u/d and ε_K/d should be investigated in order to resolve effects of ambient turbulence scales that are likely to affect vortex shedding and the mixing properties of wakes in some turbulent environments.

Acknowledgments

References

[1]Parthasarathy, R. N., and Faeth, G. M., "Turbulence Modulation in Homogeneous Dilute Particle-Laden Flows," *Journal of Fluid Mechanics*, Vol. 220, Pt. 2, 1990, pp. 485–514.

[2]Mizukami, M., Parthasarathy, R. N., and Faeth, G. M., "Particle-Generated Turbulence in Homogeneous Dilute Dispersed Flows," *International Journal of Multiphase Flow*, Vol. 18, No. 3, 1992, pp. 397–412.

[3]Wu, J.-S., and Faeth, G. M., "Sphere Wakes in Still Surroundings at Intermediate Reynolds Numbers," *AIAA Journal*, Vol. 31, No. 8, 1993, pp. 1448–1455.

[4]Margarvey, R. H., and Bishop, R. L., "Wakes in Liquid-Liquid Systems," *Physics of Fluids*, Vol. 4, No. 7, 1961, pp. 800–805.

[5]Magarvey, R. H., and MacLatchy, C. S., "Vortices in Sphere Wakes," *Canadian Journal of Physics*, Vol. 43, Sept. 1965, pp. 1649–1656.

[6]Goldberg, A., and Florsheim, B. H., "Transition and Strouhal Number for the Incompressible Wake of Various Bodies," *Physics of Fluids*, Vol. 9, No. 1, 1966, pp. 45–50.

[7]List, R., and Hand, M. J., "Wakes of Freely Falling Water Drops," *Physics of Fluids*, Vol. 14, No. 8, 1971, pp. 1648–1655.

[8]Achenbach, E., "Vortex Shedding from Spheres," *Journal of Fluid Mechanics*, Vol. 62, Pt. 2, 1974, pp. 209–221.

[9]Nakamura, I., "Steady Wake Behind a Sphere," *Physics of Fluids*, Vol. 19, No. 1, 1976, pp. 5–8.

[10]Pao, H.-P., and Kao, T. K., "Vortex Structure in the Wake of a Sphere," *Physics of Fluids*, Vol. 20, No. 2, 1977, pp. 187–191.

[11]Sakamoto, H., and Haniu, H., "A Study on Vortex Shedding from Spheres in a Uniform Flow," *Journal of Fluids Engineering*, Vol. 112, No. 4, 1990, pp. 386–392.

[12]Kim, K. J., and Durbin, P. A., "Observation of the Frequencies in a Sphere Wake and Drag Increase by Acoustic Excitation," *Physics of Fluids*, Vol. 31, No. 11, 1988, pp. 3260–3265.

[13]Carmody, T., "Establishment of the Wake Behind a Disk," *Journal of Basic Engineering*, Vol. 87, No. 4, 1964, pp. 869–883.

[14]Hwang, N. H. C., and Baldwin, L. V., "Decay of Turbulence in Axisymmetric Wakes," *Journal of Basic Engineering*, Vol. 88, No. 1, 1966, pp. 261–268.

[15]Chevray, R., "The Turbulent Wake of a Body of Revolution," *Journal of Basic Engineering*, Vol. 90, No. 2, 1968, pp. 275–284.

[16]Uberoi, M. S., and Freymuth, P., "Turbulent Energy Balance and Spectra of the Axisymmetric Wake," *Physics of Fluids*, Vol. 13, No. 9, 1970, pp. 2205–2210.

[17]Tennekes, H., and Lumley, J. L., *A First Course in Turbulence*, MIT Press, Cambridge, MA, 1972, pp. 113–124.

[18]Hinze, J. O., *Turbulence*, 2nd ed., McGraw-Hill, New York, 1975, pp. 496–581.

[19]Schlichting, H., *Boundary Layer Theory*, 7th ed., McGraw-Hill, New York, 1977, pp. 234,235, 599.

[20]Phillips, O. M., "The Final Period of Decay of Non-Homogeneous Turbulence," *Proceedings of the Cambridge Philosophical Society*, Vol. 52, Pt. 1, 1956, pp. 135–151.

[21]Lee, D. A., and Tan, H. S., "Study of Inhomogeneous Turbulence," *Physics of Fluids*, Vol. 10, No. 6, 1967, pp. 1224–1230.

[22]Torobin, L. B., and Gauvin, W. H., "Fundamental Aspects of Solids-Gas Flow, Part V: The Effects of Fluid Turbulence on the Particle Drag Coefficient," *Canadian Journal of Chemical Engineering*, Vol. 38, No. 6, 1960, pp. 189–200.

[23]Komoda, H., "On the Effect of Free-Stream Turbulence on the Structure of Turbulent Wake," *Journal of the Japan Society of Aeronautical Engineering*, Vol. 5, Oct. 1957, pp. 274–279.

[24]Pal, S., and Raj, R., "Wake Behavior in the Presence of Free Stream Turbulence," *Journal of Engineering for Power*, Vol. 103, No. 3, 1981, pp. 490–498.

[25]Pal, S., "Freestream Turbulence Effects on Wake Properties of a Flat Plate at an Incidence," *AIAA Journal*, Vol. 23, No. 12, 1985, pp. 1868–1871.

[26]Faeth, G. M., "Mixing, Transport and Combustion in Sprays," *Progress in Energy and Combustion Science*, Vol. 13, No. 4, 1987, pp. 293–345.

[27]Kürten, H., Raasch, J., and Rumpf, H., "Beschleunigung eines Kugelförmen Feststoffteilchens im Strömungsfeld Konstanter Geschwindigkeit," *Chemie-Ingenieur-Technik*, Vol. 38, No. 9, 1966, pp. 941–948.

[28]Laufer, J., "The Structure of Turbulence in Fully Developed Pipe Flow," NACA Rept. 1174, Aug. 1954.

[29]Wu, M.-S., Kwon, S., Driscoll, J. F., and Faeth, G. M., "Preferential Diffusion Effects on the Surface Structure of Turbulent Premixed Hydrogen/Air Flames," *Combustion Science and Technology*, Vol. 78, Sept. 1991, pp. 69–96.

[30]Ruff, G. A., "Structure and Mixing Properties of the Near-Injector Region of Nonevaporating Pressure-Atomized Sprays," Ph.D. Thesis, Dept. of Aerospace Engineering, Univ. of Michigan, Ann Arbor, MI, 1990, pp. 54–58.

[31]Durão, D. F. G., Heitor, M. V., and Pereira, J. C. F., "Measurements of Turbulent and Periodic Flows Around a Square Cross-Section Cylinder," *Experiments in Fluids*, Vol. 6, No. 4, 1988, pp. 298–304.

[32]Marshall, D., and Stanton, T. E., "On the Eddy System in the Wake of Flat Circular Plates in Three-Dimensional Flow," *Proceedings of the Royal Society of London*, Vol. A130, No. A813, 1931, pp. 295–301.

Appendix F: Wu, J.-S. and Faeth, G.M. (1995) Effect of ambient turbulence intensit on sphere wakes at intermediate Reynolds numbers. <u>AIAA J</u>. 33, 171-173.

Effect of Ambient Turbulence Intensity on Sphere Wakes at Intermediate Reynolds Numbers

J.-S. Wu and G. M. Faeth

Effect of Ambient Turbulence Intensity on Sphere Wakes at Intermediate Reynolds Numbers

J.-S. Wu* and G. M. Faeth[†]

University of Michigan, Ann Arbor, Michigan 48109

Nomenclature

C_d = drag coefficient
d = sphere diameter, m
ℓ = characteristic wake width, Eq. (2), m
Re, Re_t = sphere and turbulence Reynolds numbers, $d\bar{U}_\infty/\nu$ and $d\bar{U}_\infty/\nu_t$
r = radial position, m
$\bar{U}_t$ = wake-scaling velocity, Eq. (2), m/s
$\bar{U}_\infty$ = mean relative velocity of sphere, m/s
$\bar{u}, \bar{u}'$ = mean and rms fluctuating streamwise velocities, m/s
$\bar{v}'$ = rms fluctuating cross-stream velocity, m/s
x = streamwise distance from center of sphere, m
ν, ν_t = molecular and turbulence kinematic viscosities, m^2/s

Subscripts

c = centerline value
o = virtual origin condition
∞ = ambient condition

Introduction

RECENT studies of turbulence generation in dispersed multiphase flows have motivated the need for more information about the structure of sphere wakes at intermediate Reynolds numbers[1] ($10 < Re < 1000$), prompting earlier measurements of sphere wakes in nonturbulent environments[2] and in turbulent environments having an ambient turbulence intensity of 4.0% (Refs. 3 and 4). The observations of sphere wakes in turbulent environments indicated that whereas the wakes were turbulent, their mean streamwise velocities scaled like self-preserving laminar wakes with constant but enhanced viscosities due to the presence of the turbulence.[3] Thus, based on classical similarity analysis of self-preserving round laminar wakes with constant viscosities, the mean streamwise velocities in the wakes could be scaled as follows[3,5,6]:

$$\bar{u}/\bar{U}_t = [d/(x - x_o)]\exp(-r^2/2\ell^2) \tag{1}$$

where the wake-scaling velocity and characteristic wake width are

$$\bar{U}_t/\bar{U}_\infty = C_d Re_t/32, \qquad \ell/d = [2(x - x_o)/d Re_t]^{\frac{1}{2}} \tag{2}$$

and the effective turbulence viscosity appears in Re_t. Effective turbulence viscosities were relatively independent of position and the ratios of integral and Kolmogorov length scales to d (for the ranges 11–59 and 0.08–0.80, respectively); nevertheless, they increased with Re and exhibited low and high Re regimes separated by a transition regime where effects of vortex shedding were prominent in

power spectra measured in the near-wake region ($300 \leq Re \leq 600$). Unfortunately, the effect of ambient turbulence intensity on the existence and properties of laminar-like turbulent wakes was not resolved in Ref. 3; therefore, the objective of the present investigation was to resolve effects of ambient turbulence intensity variations on sphere wakes at intermediate Re.

Experimental Methods

The sphere wakes were observed within regions having relatively constant turbulence intensities using low- and high-turbulence wind tunnels having length scales similar to Ref. 3. The test arrangement for the high-turbulence wind tunnel was the same as Ref. 3, except that a perforated disk was centered on the duct axis near its downstream end, yielding a slowly decaying turbulence field so that sphere wakes could be observed at turbulence intensities of 7.0 and 9.5%, with mean and fluctuating ambient velocities varying less than 1% over the region of interest. The turbulence in the low-turbulence wind tunnel was generated by a perforated disk, followed by a nozzle contraction, yielding an ambient turbulence intensity of 2.0% with mean and fluctuating velocities varying less than 1% over the region of interest. Other aspects of the experiments—the properties and mounting of the test spheres, the laser velocimeters (LV) to measure ambient and wake flow properties, and experimental uncertainties—all were identical to Ref. 3, and a complete summary of test conditions and data can be found in Ref. 4.

Results and Discussion

Vortex Shedding

The effect of Re on vortex shedding was similar to the findings of Ref. 3 over the present range of turbulence intensities: effects of vortex shedding could only be observed in the temporal power spectra for Re in the range 300–600 for turbulence intensities $\leq 7.0\%$; and effects of vortex shedding were no longer apparent in the temporal power specta at higher turbulence intensities.

Mean Velocities

Typical measurements of mean streamwise velocities are illustrated in Fig. 1. Similar to findings at all ambient turbulence intensities considered, three wake regions are observed: a near-wake region, a laminar-like turbulent wake region, and a final decay region. The laminar-like turbulent wake region is the most prominent of the three, with mean streamwise velocities scaling according to Eq. (1). The near-wake region [for $(x - x_o)/d < 2$] exhibits effects of vortex shedding for Re in the range 300–600, similar to the observations of Ref. 3. The final decay region [for $(x - x_o)/d > 40$] is characterized by conditions where the mean streamwise velocity
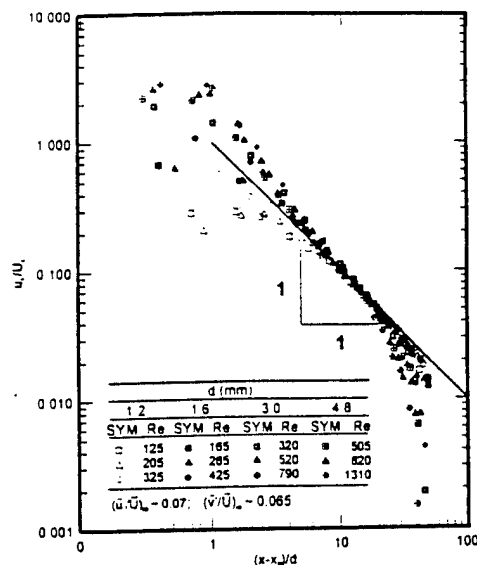

Fig. 1   Mean streamwise velocities along the axis of the wakes for $(\bar{u}'/\bar{U})_\infty = 7.0\%$.
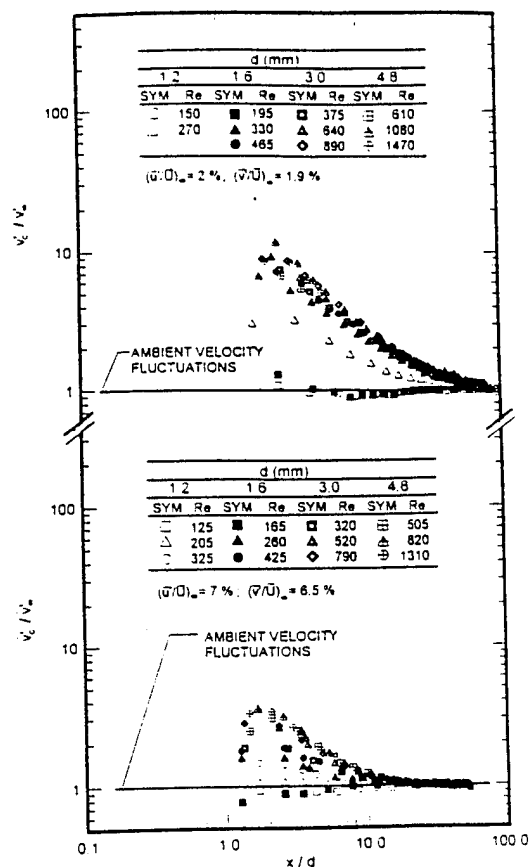

Fig. 2   Cross-stream velocity fluctuations along the axis of the wakes for $(\bar{u}'/\bar{U})_\infty = 2.0$ and 7.0%.

defect of the wake is comparable to the ambient turbulent fluctuations; this region exhibits a faster decay rate of mean streamwise velocities than any other axisymmetric wake region observed thus far.[2-4]

Velocity Fluctuations

Effects of vortex shedding, wake turbulence, and ambient turbulence on effective turbulent viscosities for the laminar-like turbulent wake region are best illustrated by cross-stream velocity fluctuations; therefore, a sample of these results is illustrated in Fig. 2. Similar to the temporal power spectra of cross-stream velocity fluctuations,[4] the results illustrated in Fig. 2 can be separated into three regimes: 1) prior to the onset of vortex shedding ($Re < 300$), the velocity fluctuations in the wake are relatively small, comparable to the ambient velocity fluctuations; 2) when effects of vortex shedding are observed in near-wake temporal spectra ($300 < Re < 600$), the cross-stream velocity fluctuations progressively increase with increasing Re; and 3) at high Re ($Re > 600$), where effects of vortex shedding are no longer observed in the near-wake temporal spectra, $\bar{v}'_c/\bar{v}'_\infty$ become independent of Re. In the high Re regime, values of $\bar{v}'_c$ are substantially enhanced from ambient turbulence levels near the start of the laminar-like turbulent wake region, but they progressively decrease and reach ambient turbulence levels at the start of the final decay region.

Effective Turbulence Viscosity

The value of the effective turbulent viscosity ν_t was found similar to Ref. 3. As noted earlier, ν_t is relatively independent of position within the laminar-like turbulent wake region but it varies as both Re and $(\bar{u}'/\bar{U})_\infty$ are varied, as illustrated in Fig. 3. Similar to the other turbulence properties of laminar-like turbulent wakes, it is evident that ν_t exhibits low, transition, and high Re regimes associated with vortex shedding behavior. The variation of ν_t/ν with Re is nearly
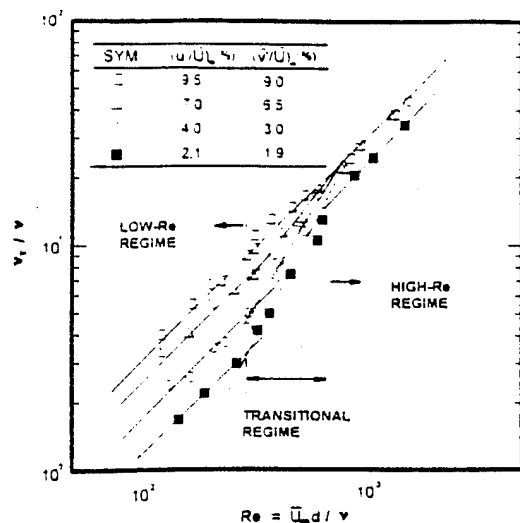
Fig. 3 Variation of turbulence viscosity with sphere Reynolds number and ambient turbulence intensity.

so that high Re behavior persists to the smallest Re considered. Whether this behavior is representative of all higher ambient turbulence levels, as suggested by behavior in the high Re regime, is an interesting issue that should be resolved.

The rate of increase of v_t/v with increasing Re is more rapid in the transition regime than in the other two regimes [except when $(\bar{u}'/U)_\infty = 9.5\%$ which was just discussed]. Properties of v_t/v are most complex in this regime since its limits at low and high Re must accommodate rather different responses to variations of ambient turbulence intensities.

Conclusions

The present study considered sphere wakes for $Re = 125$–1560, $(\bar{u}'/U)_\infty = 2.0$–$9.5\%$, and ratios of the ambient integral and Kolmogorov length scales to d in the ranges 8–59 and 0.05–1.08, respectively. The major conclusions are as follows. 1) The wakes were turbulent but scaled like self-preserving laminar wakes with enhanced viscosities due to the presence of turbulence. 2) The effective turbulent viscosities were relatively independent of position and ratios of ambient integral and Kolmogorov length scales to d, however, they varied with both Re and $(\bar{u}'/U)_\infty$ in a low Reynolds number regime ($Re < 300$) and with Re alone in a high Reynolds number regime ($Re > 600$), with the transition regime between them associated with significant effects of vortex shedding from the sphere. 3) The laminar-like turbulent wake region was followed by a final decay region beginning when $\bar{u}_c \sim \bar{u}'_\infty$, which exhibits faster decay rates than any other axisymmetric wake observed thus far.

Acknowledgments

References

[1]Mizukami, M., Parthasarathy, R. N., and Faeth, G. M., "Particle-Generated Turbulence in Homogeneous Dilute Dispersed Flows," *International Journal of Multiphase Flow*, Vol. 18, No. 3, 1992, pp. 397–412.

[2]Wu, J.-S., and Faeth, G. M., "Sphere Wakes in Still Surroundings at Intermediate Reynolds Numbers," *AIAA Journal*, Vol. 31, No. 8, 1993, pp. 1448–1455.

[3]Wu, J.-S., and Faeth, G. M., "Sphere Wakes at Moderate Reynolds Numbers in a Turbulent Environment," *AIAA Journal*, Vol. 32, No. 3, 1993, pp. 535–541.

[4]Wu, J.-S., "The Structure of Sphere Wakes at Intermediate Reynolds Numbers in Still and Turbulent Environments," Ph.D. Thesis, Department of Aerospace Engineering, Univ. of Michigan, Ann Arbor, MI, 1994.

[5]Tennekes, H., and Lumley, J. L., *A First Course in Turbulence*, Massachusetts Inst. of Technology Press, Cambridge, MA, 1972, pp. 113–124.

[6]Schlichting, H., *Boundary Layer Theory*, 7th ed., McGraw-Hill, New York, 1977, pp. 234–235 and 599.

linear for a particular value of $(\bar{u}'/U)_\infty$ in the low Re range, with values progressively increasing as $(\bar{u}'/U)_\infty$ increases. This behavior can be explained based on crude mixing-length concepts of turbulent transport, e.g., $v_t - v \sim \bar{v}'\ell$. Now $\bar{v}' \sim \bar{v}'_\infty$ before vortex shedding begins whereas $\ell \sim d$ since the sphere size tends to control the width of the flow in the critical region near the start of the laminar-like turbulent wake. Thus, $v_t - v \sim \bar{v}'d \approx (\bar{v}'/U)_\infty U_\infty d$ or $v_t/v - 1 \sim Re(\bar{v}'/U)_\infty$. This implies that v_t/v should increase linearly with both increasing Re and $(\bar{v}'/U)_\infty \sim (\bar{u}'/U)_\infty$, similar to the behavior observed in Fig. 3.

The variation of v_t/v also is nearly linear in Re in the high Re regime but is less dependent on the ambient turbulence intensity. This behavior can be explained by invoking the same mixing-length argument as before although noting that $v_t \gg v$ in the high Re regime. Then, $v_t/v \sim \bar{v}'\ell/v$ and in the laminar-like turbulent wake, $\bar{v}' \sim \bar{U}_\infty \gg \bar{v}'_\infty$. Estimating $\ell \sim d$, as before, then yields $v_t/v \sim \bar{U}_\infty d/v = Re$, generally, as observed in Fig. 3. As a result, v_t/v mainly is independent of $(\bar{v}'/U)_\infty \sim (\bar{u}'/U)_\infty$ in this high Re regime although the presence of ambient turbulence is needed to initiate laminar-like turbulent wake behavior. Finally, for an ambient turbulence intensity of 9.5%, effects of vortex shedding are suppressed due to the high-turbulence levels, as discussed earlier,